EFFECT OF SAMPLE PROCESSING ON PERCOLATED AL_2O_3 –SIC_W COMPOSITES

A Thesis
Presented to
The Academic Faculty

by

Justin Brandt

In Partial Fulfillment
of the Requirements for the Degree
Materials Science and Engineering in the
School of Materials Science and Engineering

Georgia Institute of Technology
December 2014

EFFECT OF SAMPLE PROCESSING ON PERCOLATED AL_2O_3 –SIC_W COMPOSITES

Approved by:

Dr. Rosario Gerhardt, Advisor
School of Materials Science and Engineering
Georgia Institute of Technology

Dr. Robert Speyer
School of Materials Science and Engineering
Georgia Institute of Technology

Dr. Tom Quantrille
Advance Composite Materials LLC

Date Approved: August 20, 2014

[To my loving parents]

ACKNOWLEDGEMENTS

I would like to thank my advisor, Dr. Gerhardt. Without her guidance and direction, none of this would have been possible. The funding was provided via the NSF under DMR# 1207323. I am also grateful for the wonderful surroundings my family and friends provide. The assistance provided by Dr. Tom Quantrille and Advanced Composite Materials (ACM) LLC along with Dr. Erica Corral at the University of Arizona were essential for the creation of the hotpressed and spark plasma sintered samples, respectively. I also acknowledge the contributions of Brian Bertram, Rachel Muhlbauer, Tim Pruyn, Salil Joshi, and Youngho Jin for their various contributions within the lab. Monique Mack was helpful by acquiring some of the data used in this study.

TABLE OF CONTENTS

Page

ACKNOWLEDGEMENTS iv

LIST OF TABLES viii

LIST OF FIGURES ix

SUMMARY xiii

CHAPTERS

1 Introduction 1

1.1 Ceramic Composites 1

1.2 Whisker Composites 2

1.3 Percolation 2

1.4 General Electrical Characterization 4

1.5 Commercial Application 6

1.6 Objective of This Research 7

2 Experimental Details 9

2.1 Detailed Characterization of 20% SiC_w Extruded Rods 9

2.1.1 Samples Measured 9

2.1.2 Extruded Rod Anisotropy 11

2.1.3 Extruded Full Rod Sectioning 13

2.2 Powder Creation for Hot Press and Spark Plasma Sintering 15% SiC_w Pellet Samples 17

2.2.1 Hot Pressing 18

2.2.2 Spark Plasma Sintering 22

2.2.3 Expected Microstructure of HP/SPS Samples 25

2.3 Microstructural Characterization 26

2.3.1 Sample Polishing for Microscopy 26

2.3.2 Scanning Electron Microscopy 27

2.3.3 Atomic Force Microscopy 28

2.3.3.1 Current Atomic Force Microscopy (I-AFM) 28

2.4 Impedance Testing Preparation 32

2.4.1 Sample Electroding 32

2.4.2 Electrical Measurements of Samples 33

2.4.3 Data Manipulation 35

3 Results on Characterization of Extruded Rod Samples 36

3.1 Full Rod Measurements of 20% SiC_w-Al_2O_3 Samples 36

3.2 Breakdown of Full Rods 47

3.3 Anisotropy of Rod Microstructure 58

3.3.1 SEM Confirmation of Anisotropic Microstructure in the Extruded SiC_w-Al_2O_3 Composites 58

3.3.2 Impedance Measurements for Different Sample Orientations With and Without Bias 63

3.4 Measurements on Thin Slices with Sputtered Electrodes 67

4 Results on Hot Pressed and Spark Plasma Sintered 15% SiC_w Samples 73

4.1 Electrode Effect in Hot pressed and Spark Plasma Sintered Samples 73

4.1.1 Hot Press Sample Analysis 73

4.1.2 Spark Plasma Sintered Specimens 78

4.1.3 Comparison of Ag Paint and Sputtered Ag Electrodes 83

4.1.3 Comparison of HP vs SPS with Sputtered Ag 86

4.2 SPS Parameters Effect 90

4.3 EDX Measurements 92

4.4 XRD Data 95

5 Conclusions and Future Work 98

5.1 Conclusions 98

5.2 Future Work 100

REFERENCES 101

LIST OF TABLES

Page

Table 2.1: Compilation of All Tests Done with Eight Extruded Rods 16

Table 2.2: Powder Breakdown in Terms of Constituent Weight and Percentages 17

Table 2.3: Hot Press Sample Geometries and Bulk Densities 21

Table 2.4: Spark Plasma Sintered Sample Compilation 24

Table 2.5: Geometric Properties for Samples Fabricated by SPS 26

Table 3.1: Individual Breakdown for All Three Impedance Peaks Along with the Main Modulus Peak 45

Table 3.2: Circuit Fits Across All Full Rod and Different Sample Lengths for the 20L Extruded Rod Breakdown 52

Table 3.3: Average and Standard Deviation Values Across All Stages in Sample Sectioning for Rod 20L 52

Table 3.4: Circuit fits Across All Sample Lengths for the 20C Extruded Rod Breakdown 54

Table 3.5: Average and Standard Deviation Values Across All Stages in Sample Sectioning for Rod 20C 54

Table 3.6: Maximum and Peak Frequency Values for 20C Eighths Comparison 55

Table 4.1: Bulk and Ag Paint Electrode Response for Hot Pressed Samples 75

Table 4.2: Bulk and Ag Paint Electrode Response for Spark Plasma Sintered Samples 80

LIST OF FIGURES

Page

Figure 1.1: Different composite structure types for secondary phases are listed 3

Figure 1.2: Monte Carlo Simulation depicting a graphical rendering of whisker percolation 3

Figure 1.3: Graph showing the percolation thresholds for multiple sample processing methods 4

Figure 1.4: Combination of a) example of a microwave heating element, b) Individual Silar rods being held together which absorb the radiation, and c) Microwave heating element in action 6

Figure 1.5: a) Cutting tool inserts, b) Cutting tool insert marked with arrow machining hardened tool steel. Images were provided by Greenleaf Corporation in Saegertown, PA 7

Figure 2.1: Basics of extrusion, a ram powered by hydraulics forces the material through a narrow die resulting in a new shape 10

Figure 2.2: a) Industrial extruder. b) Extrudate of different compositions separated by colored dyes before cutting and binder burnout 11

Figure 2.3: Viewing of whiskers along and perpendicular to the extrusion direction 11

Figure 2.4: Schematic of sample cutting procedure from parallel to perpendicular direction 12

Figure 2.5: Full length extruded rods before any cuts are made 13

Figure 2.6: Full length extruded rod breakdown into smaller constituents and labeling system 14

Figure 2.7: Allied Techcut Precision Sectioning Machine used to cut full length extruded rods 15

Figure 2.8: Buehler Isomet 1000 Precision Saw used for precision cuts such as thin slices 15

Figure 2.9: Hot Press at Advanced Composite Materials, LLC 19

Figure 2.10: Temperature ramp up and hold for Hot Press Sintering 20

Figure 2.11: (a) Standard hot pressing configuration (b) Utilizing spacers to press multiple samples in a single cycle 20

Figure 2.12: Spark Plasma Sintering (SPS) pressing apparatus in Arizona Model 10-4 manufactured by Thermal Technology LLC 23

Figure 2.13: Temperature, voltage, and current output during Spark Plasma Sintering 23

Figure 2.14: Schematics depicting whisker orientation common for both HP and SPS samples 25

Figure 2.15: Measurement of sample through thickness 25

Figure 2.16: Zeiss Ultra60 FE-SEM located in the Marcus Cleanroom at Georgia Tech 28

Figure 2.17: Park Systems XE-100 AFM 30

Figure 2.18: Diagram for AFM scanning interactions within apparatus 31

Figure 2.19: AFM cantilever and tip scanning directly over sample microstructure 31

Figure 2.20: Turbo sputter coater used to apply sputtered silver electrodes 33

Figure 2.21: Solartron 1260 Impedance Analyzer and 1296 Dielectric Interface 34

Figure 2.22: Electrical fixtures used to measure cut samples and full length extruded rods 34

Figure 3.1: (a) |Z*| vs. Frequency, (b) Theta vs. Frequency for eight separate extruded ceramic composite rods 37

Figure 3.2: Low frequency resistance value histogram comparison 38

Figure 3.3: a) Real Resistivity vs. Frequency, b) Imaginary Resistivity vs. Frequency for eight full rods 39

Figure 3.4: Imaginary Resistivity vs. Real Resistivity across all full length extruded rods 40

Figure 3.5: a) Real Modulus vs. Frequency, b) Imaginary Modulus vs. Frequency of eight different full length rods 41

Figure 3.6.1: Normalized Z'' and M'' vs. Frequency for full length rods A, C, CB, and D for a) – d) respectively 42

Figure 3.6.2: Normalized Z'' and M'' vs. Frequency for full length rods K, L, O, and Wt for a) – d) respectively 43

Figure 3.7: Peak breakdown of extruded rod D for the impedance data 45

Figure 3.8: Equivalent circuit used in modeling impedance data for extruded samples 47

Figure 3.9: a)-d) Complex impedance graphs for the full, halves, fourths, and eights respectively of the extruded rod 20L consisting of alumina with SiC_w measured using impedance spectroscopy 48

Figure 3.10: a)-d) Complex impedance graphs for the full, halves, fourths, and eights respectively of the extruded rod 20C consisting of alumina with SiC_w measured using impedance spectroscopy 49

Figure 3.11.1: Normalized Z'' and M'' vs. Frequency for first half of rod 20C's eighth sized samples 56

Figure 3.11.2: Normalized Z'' and M'' vs. Frequency for second half of rod 20C's eighth sized samples 57

Figure 3.12: Side by side comparisons of whisker views between the parallel to extrusion direction (left) and perpendicular to extrusion direction (right) at three different magnifications 59

Figure 3.13: Relative density of extruded rods compared to theoretical density against whisker volume concentration for pressureless sintered rods and discs 60

Figure 3.14: Anisotropy comparison of the impedance response normalized by geometric dimensions for measurements parallel and perpendicular to the extruded direction for the 20L samples L111, L112, L121, and L122 eighth samples 62

Figure 3.15: DC bias variations from 0 to 40V for the L112 a) parallel, b) perpendicular, L122 c) parallel, and d) perpendicular of the 20L extruded rod using complex impedance plots 65

Figure 3.16: Complex normalized resistivity response for two 10% SiC_w samples with different thickness and contact areas 66

Figure 3.17: a) Ag paint impedance response, b) Ag sputter impedance response both for the same thin slice from an extruded rod 66

Figure 3.18: Comparison of complex impedance behavior with no bias for the 20C extruded rod thin slices (<2 mm thick) 67

Figure 3.19: Side by side comparison with the addition of 0-40V DC bias for the 20C extruded rod thin slice samples. Please note that part (d) has a different scale. 69

Figure 3.20: Low frequency values at each value of DC bias for all four extruded rod thin slice samples 71

Figure 3.21: I-AFM and topography imaging of an extruded pressureless sintered thin section sample taken with a Pt coated AFM tip at 10V bias shown 72

Figure 4.1: a) Comparison across all five powder compositions using the silver paint electrode, b) Comparison across all five powder compositions using the silver sputter electrode for HP samples 74

Figure 4.2: SEM images of all five compositions for the hotpressed samples 76

Figure 4.3: a) Comparison of the electrical properties across all SPS sintered five powder compositions using the silver paint electrode, b) Comparison across all five powder compositions using the silver sputter electrode for SPS samples 79

Figure 4.4: SEM images of all five compositions for the spark plasma sintered samples 81

Figure 4.5: Side by side comparison of electrode effect for both HP and SPS samples across all powder compositions 84

Figure 4.6: Comparison between 15% SiC_w composites made by Brian Bertram and Justin Brandt 86

Figure 4.7: Direct comparison between hotpressing and spark plasma sintering for each sample 88

Figure 4.8: Whisker junction schematic for a) directly touching whiskers junctions, b) whisker junctions which are not directly in contact, and c) whiskers alone 90

Figure 4.9: a) and b) All four sample sets for the SPS compared for the two extremes of the sintering additives E and D respectively 91

Figure 4.10: SEM base image used for EDX study 92

Figure 4.11: EDX highlighting individual element positions relative to SEM image from Figure 4.10 93

Figure 4.12: Map spectra for EDX showing both the counts relative to the electric field and the map sum spectrum of the elements 94

Figure 4.13: XRD data for SPS samples set 4 overlapped to outline differences in additive content 96

Figure 4.14: Zoomed in version of XRD data to specifically showcase some peaks attributed to Y_2O_3 and MgO 97

SUMMARY

This research focuses on the Al_2O_3 –SiC_w ceramic composite system. The overarching goal of this study was to study the differences in properties that result from various processing methods. The three main processing methods include extruded and pressurelessly sintered rods, hotpressing, and spark plasma sintering. Samples made through extrusion were studied as a function of sample length as well as looking at variations across multiple samples. The two sintering methods, hotpressing and spark plasma sintering, were compared with one another using five separate sets of samples with differing amounts of the sintering additives MgO and Y_2O_3.

Regardless of processing method, the samples were studied through the observation of the surface microstructure using SEM and AFM as well as studying the electrical properties by using Impedance Analysis. By relating the surface microstructure to the impedance data gathered, equivalent circuits which describe individual aspects of the composite microstructure could be formulated. XRD and EDX were utilized as supporting techniques in order to confirm sample compositions both in terms of the matrix and filler materials, as well as the sintering additives incorporated.

Chapter 1

Introduction

This thesis is split into five chapters which include this introduction, the experimental methods section, two main results and analysis chapters, separated into the extruded rod section and hotpressing/spark plasma sintering sections, and finally a conclusions chapter which finishes with recommended future work. This format will suit this thesis best as the processing methods and their tests can be described separately.

1.1 Ceramic Composites

Ceramic composites specifically those containing alumina (Al_2O_3) and silicon carbide (SiC) have been around since the 1980s. Initial applications were heavily focused upon their mechanical and thermal properties. However, with recent emerging commercial applications focused on their use as electromagnetic absorbers, the electrical response of these materials has also become a focal point of scientific interest. Depending on whether the second phase is being considered for electrical or mechanical properties changes the naming convention of the second phase to ‘filler’ or ‘reinforcement’ respectively [1]. In the case of ceramic composites, historically second phases have been added to improve the fracture toughness of a brittle matrix [2]. The driving force behind what makes the electrical properties of a composite interesting is the concept of percolation.

1.2 Whisker Composites

Studies focusing on the electrical properties of whisker composites have a strong literature presence, some which have been published as early as 1991 [3,4]. SiC whisker reinforced mullite composites [5] as well as Boron Nitride - Boron Carbide and Boron Nitride - Silicon Carbide systems [6-8] have been researched as well before moving onto an Alumina – Silicon carbide system studied by Mebane [9-12] and Bertram [1, 13-16]. These resources served as the backbone to the research conducted throughout this thesis.

1.3 Percolation

Percolation refers to the formation of a fully interconnected network between the filler materials. The filler material by definition should be present in much smaller quantities compared to the matrix material. Once the limited amount of filler is able to establish a connected path, it will be able to influence the properties of the composite as a whole. The concept of percolation has been studied on numerous occasions in the past. The shape of the fillers has a strong influence upon percolation. Some common types of composite structures include layered, continuous fibers, platelets, and whiskers and are shown in Figure 1.1[17]. When the phases of the composite structures are arranged as continuous layers or as continuous fibers, the rule of mixtures can be used to describe its properties. In the case of discontinuous additions of the second phase, effective medium theory (EMT) or micromechanics models are used to describe the electrical and mechanical responses, respectively [18-20].

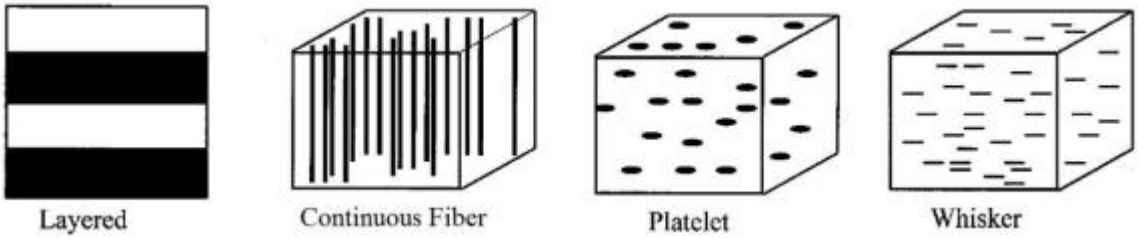

Figure 1.1: Different composite structure types for secondary phases are listed [17].

Especially, for this exact material system, a Monte Carlo simulation has been conducted looking at the whisker percolation [9]. Figure 1.2 shows a possible percolating path formed by the SiC whiskers which have a high aspect ratio.

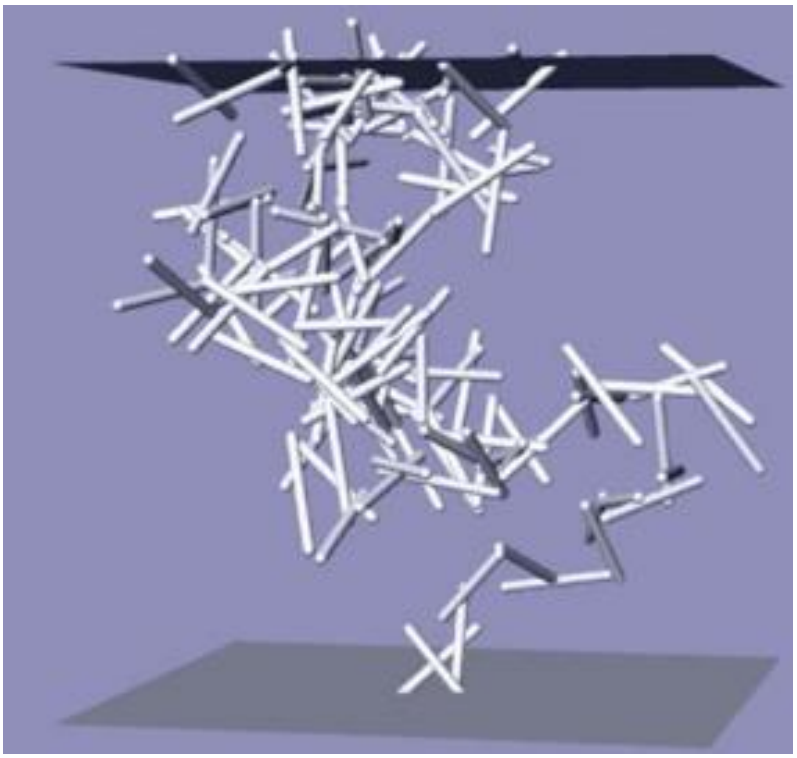

Figure 1.2: Monte Carlo simulation depicting a graphical rendering of whisker percolation[9].

In addition to the simulations done by Mebane, the percolation threshold across multiple sample processing methods including extrusion and pressureless sintering, hotpressing, and drypressed and pressureless sintered discs have been studied in detail [9,10, 13-16]. The exact

percolation thresholds for the different processing methods are shown in Figure 1.3[16]. It was noted within this research how the processing does have a substantial effect upon the percolation results changing both the SiC composition necessary to have it occur at as well as the magnitude of conductivity change resulting from the percolation. The conductivity of the hot-pressed samples shows a higher conductivity post percolation due to the simultaneous application of pressure and temperature during hot pressing. The other two percolation curves shown in the figure were for pressurelessly sintered composites.

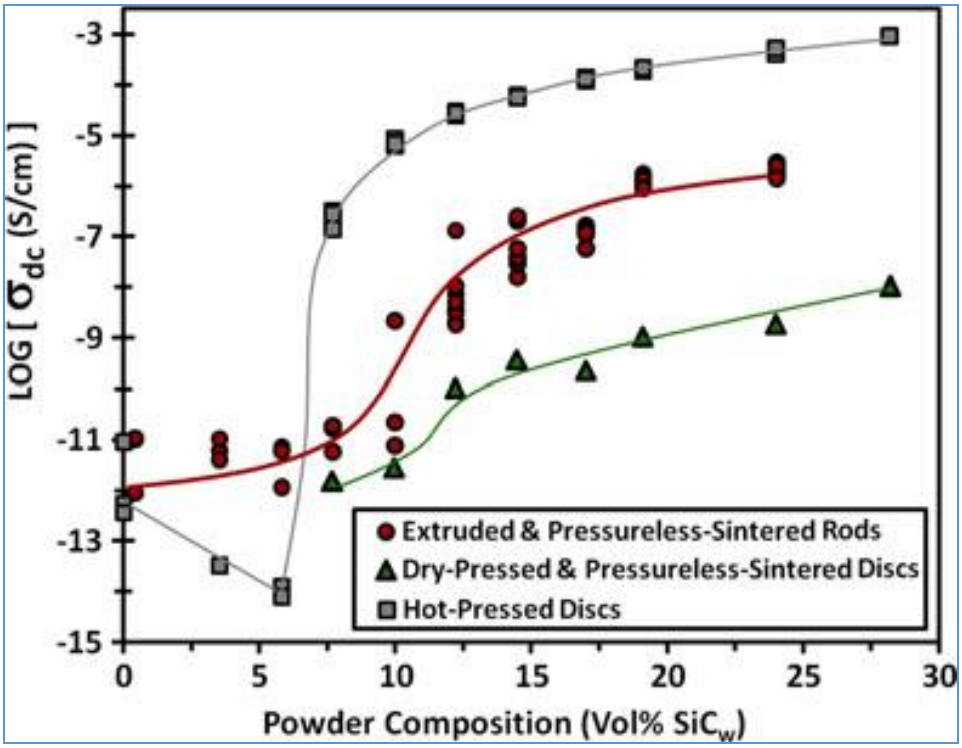

Figure 1.3: Graph showing the percolation thresholds for multiple sample processing methods [16].

1.4 General Electrical Characterization

An integral part of this research was the electrical characterization done through impedance spectroscopy. Impedance spectroscopy is a nondestructive technique which makes

use of alternating current at a wide range of frequencies to garner a response from the sample. Data acquired from impedance spectroscopy is ripe with information[21]. The impedance data can be converted into other dielectric functions which can be used to further analyze the sample[22]. This technique can be used to characterize the microstructure of many samples by attributing individual responses to specific areas within the sample microstructure[23]. The four dielectric functions include complex impedance (Z*), complex admittance (Y*), complex dielectric constant (ε*), and complex modulus (M*). The relationships between them can be summarized in the following equations:

$$\varepsilon^* = \varepsilon' - j\varepsilon'' \quad (1)$$

$$M^* = M' + jM'' = \frac{1}{\varepsilon^*} \quad (2)$$

$$Z^* = Z' - jZ'' = \frac{1}{j\omega C_0 \varepsilon^*} \quad (3)$$

$$Y^* = Y' + jY'' = j\omega C_0 \varepsilon^* \quad (4)$$

The j corresponds to $\sqrt{-1}$, while ω is the angular frequency equal to 2πf. The C_0 is the geometrical capacitance [22]. Using the combination of complex impedance data along with the data available from the other dielectric functions, equivalent circuits can be constructed to help characterize the microstructure. Data fitting can be attempted and once a suitable candidate for the equivalent circuit has been proposed. Many instances of the application of impedance spectroscopy in order to study microstructure exist [23-29] as it continues to offer valuable insight in the electrical characterization of materials.

1.5 Commercial Applications

The applications for this ceramic composite of Al_2O_3 and SiC depend upon how they were fabricated. The extruded samples are able to be used as microwave heating elements. They serve as electromagnetic absorbers which heat up by absorbing microwave radiation inside the microwave. The frequencies of interest include 915 or 2450 MHz, common among microwave ovens. This research is being headed by Advanced Composite Materials LLC in Greer, SC [30]. Several rods which are roughly 1 foot long and ½ inch wide can be made by extrusion and pressureless sintering. Arranging these into a grill, allows for cooking with foods such as pizzas and panini sandwiches. The microwave heating elements can be seen in Figure 1.4. The results yield promising results with both shorter cooking time which saves energy in terms of microwave usage, and better quality food (e.g. grill marks, crispy crust, etc.) [1,31].

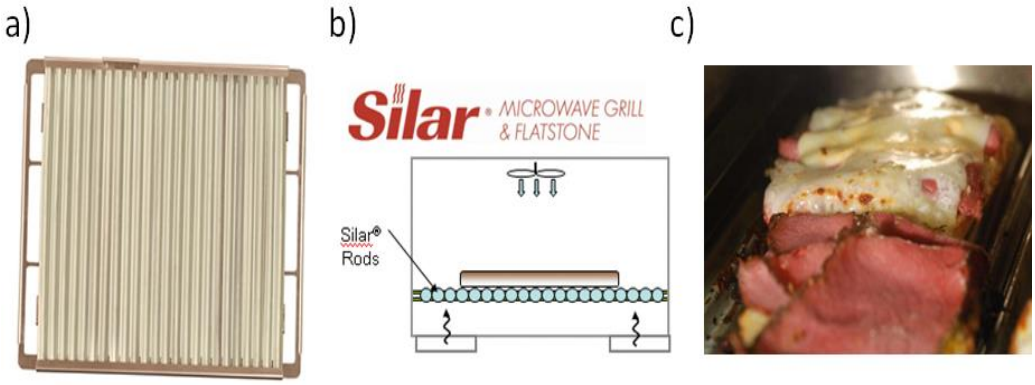

Figure 1.4: Combination of a) example of a microwave heating element, b) individual silar rods being held together which absorb the radiation, and c) microwave heating element in action [31].

When these materials are instead fabricated through hotpressing, the improved density and mechanical properties enables their usage as cutting tool inserts. For cutting tool applications the following properties are extremely important: abrasive wear resistance, thermal conductivity,

fracture toughness, chemical intertness, and thermal shock resistance. This composite system provides improvements over conventional ceramics in all areas except for chemical inertness [1].

The complications regarding ceramic cutting tools has been explored in the past [32,33]. Defect distribution within the tool, tool shape, and sample properties all play a role when considering cutting tools. Sample orientation relative to the processing direction and fracture toughness on the microstructural scale heavily influence the wear performance over the fracture toughness of the bulk sample [34]. Examples of cutting tool inserts can be seen in Figure 1.5.

Figure 1.5: a) cutting tool inserts, b) cutting tool insert marked with arrow machining hardened tool steel. Images were provided by Greenleaf Corporation in Saegertown, PA

1.5 Objective of this research

The goal of this research was to build upon the previous research done by Mebane [9-12] and Bertram [13-16]. Bertram succeeded in determining percolation threshold values for this system containing Al_2O_3 and SiC using various processing methods[16], but percolation for hot pressed samples only has been reported previously in the literature as well [9,10,15]. Additionally, in regards to the extruded rods, a study was conducted upon the full length rods and extremely thin slices around 2mm, but only the extremes were measured[14]. This left the

intermediate lengths to be explored. This was accomplished by sectioning the rods and studying the impedance responses along the way. A preliminary version of such a study was published last year[35].

Additionally, sintering additives used in the previous study on hot pressed samples [14-16] contained 1% Y_2O_3 and 1% MgO across all samples or none at all[9,10,13]. While SiC composition was varied, sintering additives were not. So in this study, while only one composition was studied, it was looked at in scrutiny by adjusting the sintering additives as well. Starting with a completely pure composite with respect to sintering additives and working gradually up to the 1% Y_2O_3 and 1% MgO values, five separate additive compositions have been made while keeping the SiC_w content constant at 15%.

Spark plasma sintering was an additional processing method that was used during this study. This is the first time this fabrication method has been applied to the composite system of Al_2O_3 and SiC_w with these sintering additives. Its purpose was to provide a comparison with the hot pressed samples which will have similar microstructures. A wide variety of ceramic systems have been studied by spark plasma sintering to some extent; however, exact details of the densification methods are still subject to study and modeling [36]. Spark plasma sintering has been noted for its fast and efficient sintering, which happens due to the combined action of spark discharge, Joule heating, electrical diffusion, and plastic deformation effect [37].

Chapter 2

Experimental Details

This thesis contains two results chapters following the presentation of the experimental details. These include the extruded rods analysis in chapter 3 and the combination chapter 4 detailing the fabrication and characterization of hot pressed and spark plasma sintered samples. Experimental details are presented separately below for each chapter initially, excluding the sections they share in common which will be presented at the end. This includes microstructural and electrical characterization.

2. 1 Detailed Characterization of 20% SiC_w Extruded Rods

2.1.1 Samples measured

The extruded and pressure-less sintered 20% SiC_w samples used in the first part of this study were taken from the samples made by Brian Bertram [1]. For completeness sake, some details related to their processing are included here.

In order to effectively perform extrusion, the dry ceramic powders must be uniformly mixed with binders which enhance the strength in order to handle the otherwise fragile green bodies. The components of a binder system include water, a flocculant, a coagulant, and a lubricant. The concept for extrusion is shown in Figure 2.1, where a ram forces the mixture through an enclosure with a die at the other end.

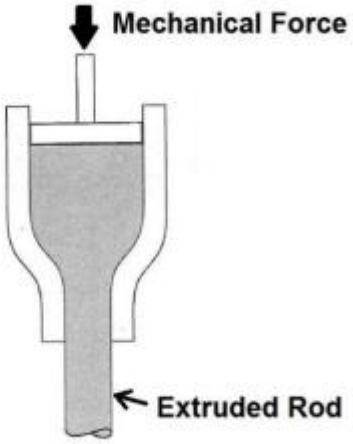

Figure 2.1: Basics of extrusion, a ram powered by hydraulics forces the material through a narrow die resulting in a new shape [38]

Before sintering can occur for the extruded samples, the binders must be removed. Water and mineral oil are evaporated from the extruded sample in a low temperature environment over a long period of time. The more stable organics of the binder in turn must be removed through a burnout process at 550 °C in an oxidizing environment. The peak temperature used during the pressureless sintering was 1725 °C in a flowing N_2 ambient using an ACM-proprietary ramp/hold schedule. The peak temperature used was constant regardless of composition in order to reduce the number of variables. The final dimensions of the extruded rods were 23-26.5 cm and 14-15mm for the lengths and diameters respectively. Figure 2.2 shows both the extruder machine as well as initial extrudate before any cutting and binder burnout. For further details of the extruded samples refer to Bertram's PhD thesis [1].

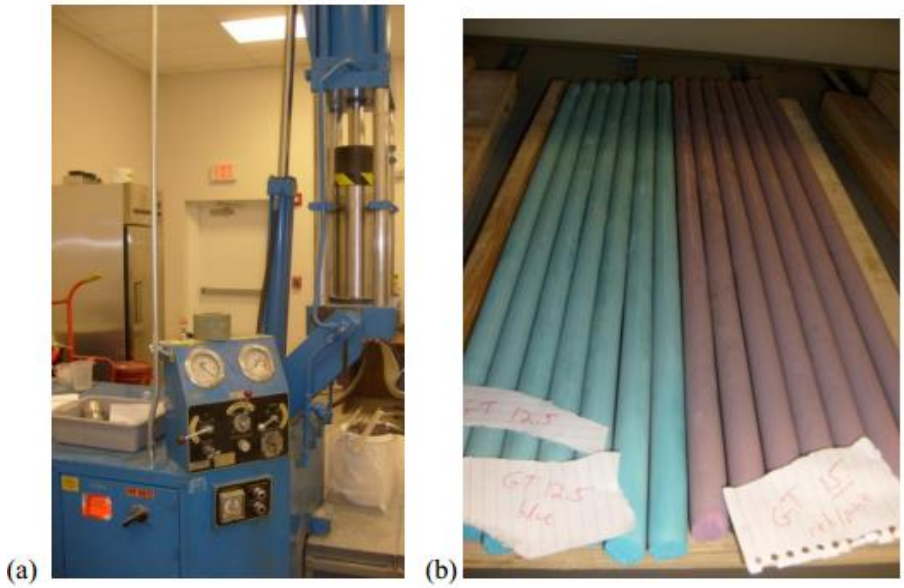

Figure 2.2: a) Industrial extruder. b) Extrudate of different compositions separated by colored dyes before cutting and binder burnout [1]

2.1.2 Extruded Rod Anisotropy

The extrusion process results in a sample anisotropy reflected by the whisker orientation. This is due to the force exerted to funnel the material through the much thinner die at the end of the enclosure. Schematics that show the difference in how the whiskers align along the extrusion direction and its perpendicular cross-section are shown in Figure 2.3 [16].

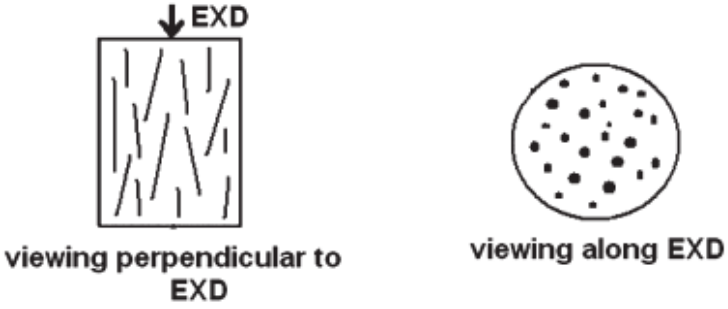

Figure 2.3: Viewing of whiskers along and perpendicular to the extrusion direction [16]

Furthermore, in order to effectively take impedance measurements on the two distinct directions of the extruded samples, it became necessary to machine the sample so that electrodes

could be applied easily and ultimately the samples to be measured. Figure 2.4 illustrates the cuts necessary to take the perpendicular measurements. The remaining darker square from the original cylindrical rod becomes the new shape to accommodate the electrodes.

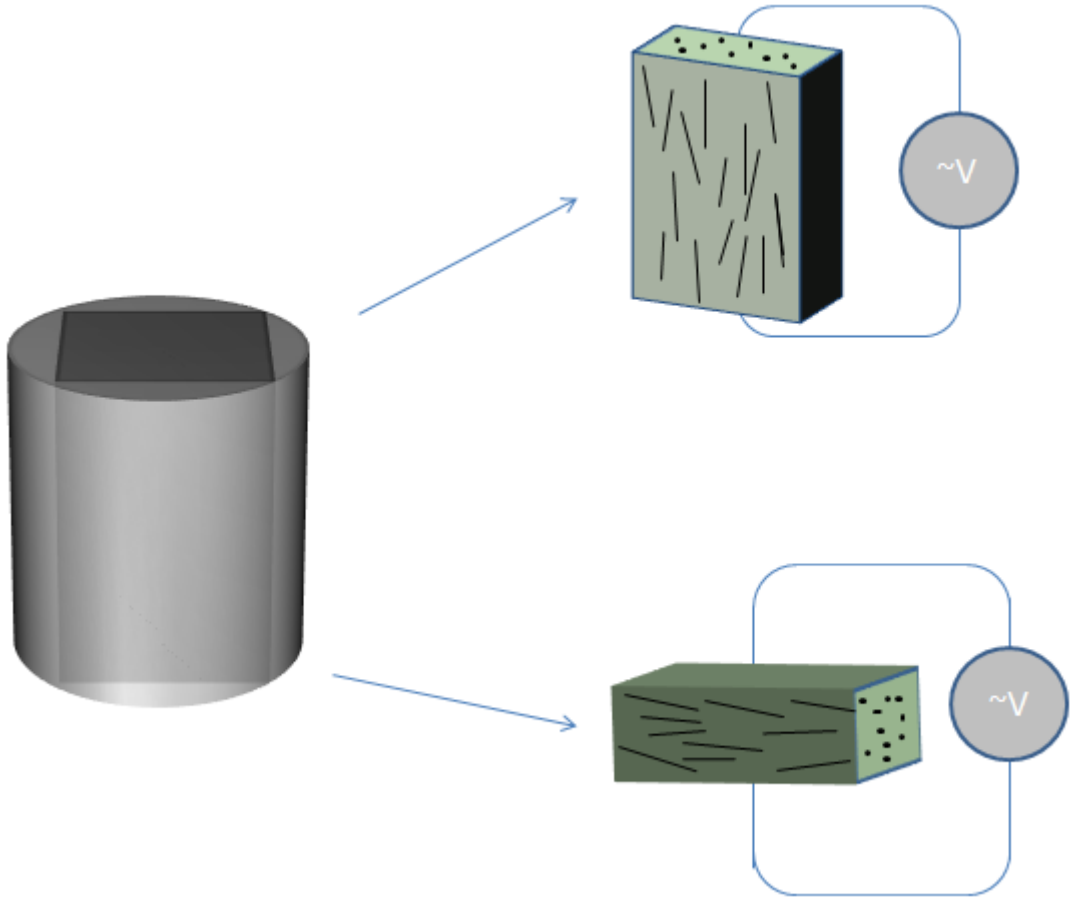

Figure 2.4: Schematic of sample cutting procedure from parallel to perpendicular direction

2.1.3 Extruded Full Rod Sectioning

Further testing on the extruded rods was conducted by cutting the full length rods that average 25.60 cm in length into smaller constituents (see Figure 2.5 below). After initial impedance tests were completed, the full rods were first cut into two halves. The halves were coated with electrodes and measured once again. This process continued by cutting the halves into fourths and finally into eighths continuing the impedance measurements along each step of the way. One of the bars, rod 20C, was further sliced into 2mm sections. Figure 2.6 shows the breakdown of a full length rod using this process.

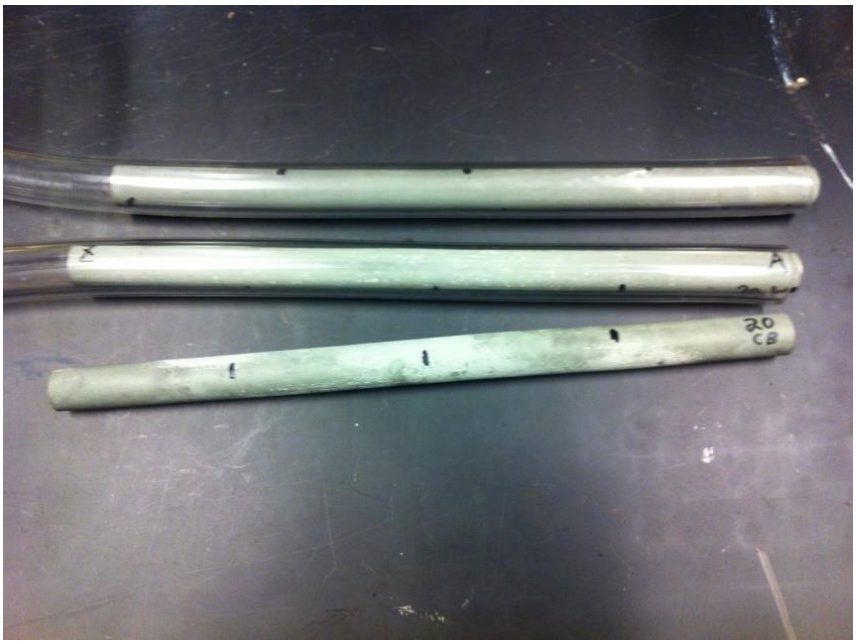

Figure 2.5: Full length extruded rods before any cuts are made

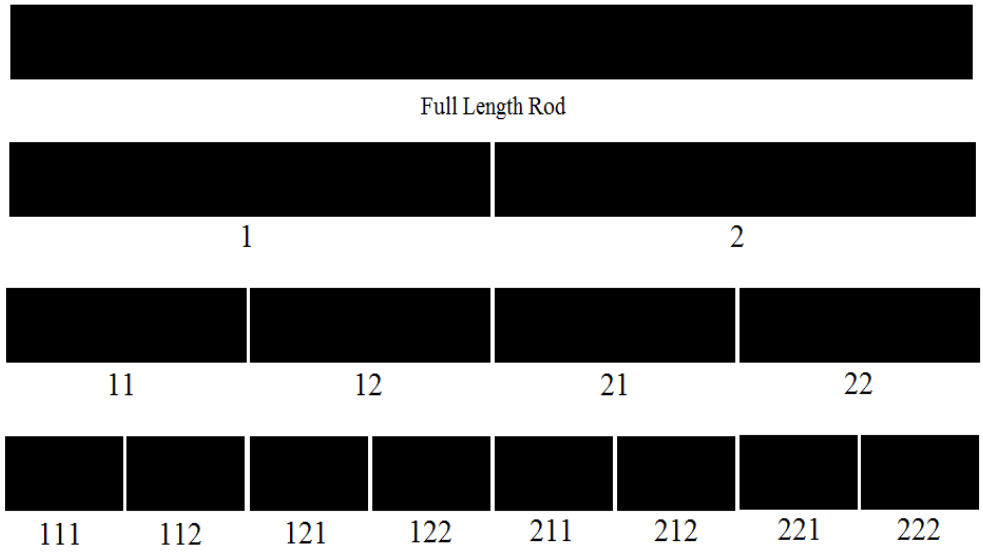

Figure 2.6: Full length extruded rod breakdown into smaller constituents and labeling system

A combination of the Techcut 5 Precision Sectioning Machine manufactured by Allied and the Isomet 1000 Precision Saw manufactured by Buehler, shown in Figure 2.7 and Figure 2.8 respectively, were used for cutting the rods. The former was mainly used for the initial cuts for the full length rods that would not be able to fit in the smaller Isomet 1000. The Isomet 1000 was especially useful in making thin slices because the precision with which cuts could be made was superior. Table 2.1 lists all of the full length rods measured and how many sections were cut from them as well as the characterization techniques utilized.

Figure 2.7: Allied Techcut Precision Sectioning Machine used to cut full length extruded rods

Figure 2.8: Buehler Isomet 1000 Precision Saw used for precision cuts such as thin slices

Table 2.1: Compilation of All Tests Done with Eight Extruded Rods

20% Samples	SEM	Measurement	I-AFM	Parallel Slices	Perpendicular Slices
A		10 MHz – 10 mHz		1	
C		10 MHz – 10 mHz,	Yes	1 2, 1/2 4, 1/4 8, 1/8 4, 2mm slices	
CB		10 MHz – 10 mHz		1	
D		10 MHz – 10 mHz		1	
K		10 MHz – 10 mHz		1	
L	Yes	10 MHz – 10 mHz, 0-40V DC Bias		1 2, 1/2 4, 1/4 8, 1/8	4 of 1/8 slice samples converted
O		10 MHz – 10 mHz		1	
Wt		10 MHz – 10 mHz		1	

2.2 Powder Creation for Hot Press and Spark Plasma Sintering 15% SiC_w Pellet Samples

A total of five powder blends were created to pursue sample creation for comparing the microstructure and properties of Hot-Press and Spark Plasma Sintered specimens. These powders were mixed at Advanced Composite Materials, LLC in Greer, South Carolina. Sintering additives at different weight concentrations were added to help densify the samples as well as seeing their effect on the electrical properties. Initially, four blends were made using the two additives MgO and Y_2O_3. The Y_2O_3 was held constant at 1% while the MgO was varied from 0, 0.25, 0.5, and 1% with the sample notation A-D. Finally, a completely pure sample was added and named sample E.

Table 2.2: Powder Breakdown in Terms of Constituent Weight and Percentages

	Mass					Fraction				
	A (g)	B (g)	C (g)	D (g)	E (g)	A (%)	B (%)	C (%)	D (%)	E (%)
SiC	300	300	300	300	300	0.15	0.15	0.15	0.15	0.15
MgO	0	4.25	8.5	17	0	0	0.0021	0.0043	0.0085	0
Y_2O_3	17	17	17	17	0	0.0085	0.0085	0.0085	0.0085	0
Al_2O_3	1683	1678.75	1674.5	1666	1700	0.842	0.839	0.837	0.833	0.85

The powder breakdown was as shown in Table 2.2. Sample batches amounted to 2000g for each composition. The SiC weight percent was set first and foremost to ensure the whisker

concentration was exactly at the intended amount of 15% weight. The weight of the additives was then taken from the remaining weight allotted to the alumina.

Once the powder compositions were set, the next step concerned mixing and fine tuning the powder size. This was achieved by ball milling. The media proceeded to mix and crush the powder into finer sizes. This process continued for 12 hours with periodic checking to make sure the powder did not clog the neck of the container. Once removed from the container the powder was then sieved and was ready to be pressed.

The powder was weighed out as reflected by the mass columns in Table 2.2 and inserted into a die where the inner surfaces were lined with a graphite sheet to prevent adverse reactions with the die especially at the high temperature that is used for sintering these samples. Inserts are used to keep the powder in place during the hot pressing. Graphite dies are well suited for usage in sintering due to their characteristics such as low coefficient of thermal expansion.

2.2.1 Hot Pressing

Hot-pressing was conducted at Advanced Composite Materials, LLC using the Thermal Technology Astro 50 Ton Vacuum Hot Press rated to 50 tons and 2000 °C shown in Figure 2.9. The maximum temperature hold used was 1650 °C and the temperature profile used is displayed in Figure 2.10.

There were ramp up/holds at 1000°C and 1400°C each at 10 minutes for both the ramp up time and the holds. This was followed up with a 20 minute ramp and hold at the maximum temperature of 1650°C. The entire process took 90 minutes and the cooling process took a similar amount of time. The pressure for the first ramp was 1540 psi and the subsequent two holds were at 4400 psi. Figure 2.11a depicts the configuration of a hot press, where the pressure needs to be

applied. The heating mechanisms which surround the hot zone including the refractory lining are also shown. Two samples could simultaneously be pressed with this set up with the introduction of spacers as shown in Figure 2.11b. Consequently, only 5 hot-press runs were needed to make the 10 samples being used in this study.

Figure 2.9: Hot Press at Advanced Composite Materials, LLC

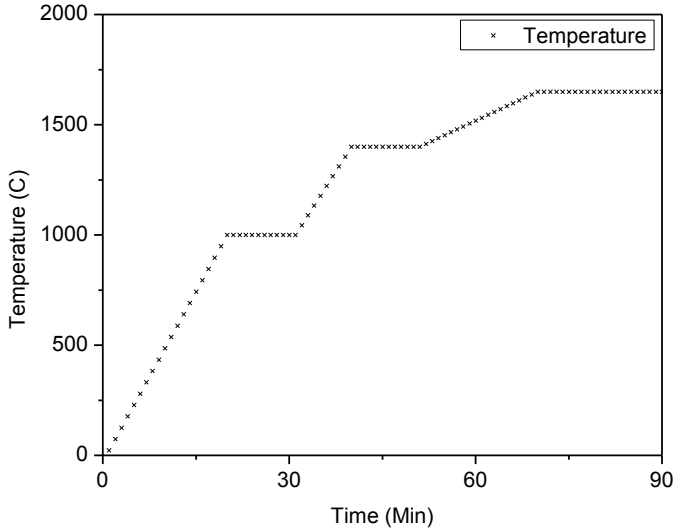

Figure 2.10: Temperature ramp up and hold for Hot Press Sintering

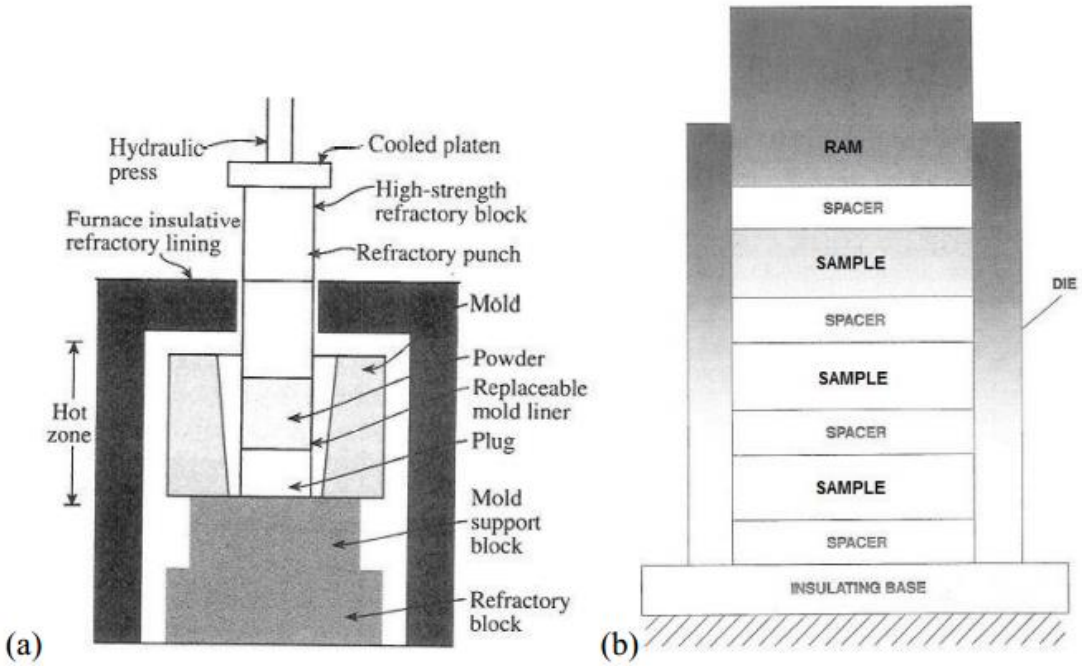

Figure 2.11: (a) Standard hot pressing configuration [38] (b) Utilizing spacers to press multiple samples in a single cycle [39]

Table 2.3 outlines the sample dimensions of all the hot pressed samples fabricated for this study. The samples were made on two separate trips and are color coded by when they were pressed. Two sets of samples were made; however, both of the pure samples were not pressed until the second trip. Diameter, thickness, volume, density, and mass are among the parameters listed in this table.

Table 2.3: Hot Press Sample Geometries and Bulk Densities

Hot Press Set 1					
	A1	B1	C1	D1	E1
Diameter (cm)	2.920	2.920	2.921	2.920	2.911
Thickness (cm)	0.623	0.613	0.608	0.628	0.728
volume (cm^3)	4.172	4.105	4.074	4.205	4.845
Density (g/cm^3)	3.848	3.847	3.846	3.845	3.839
Mass (g)	16.054	15.793	15.672	16.169	18.600
Hot Press Set 2					
	A2	B2	C2	D2	E2
Diameter (cm)	2.919	2.917	2.914	2.916	2.917
Thickness (cm)	0.768	0.780	0.835	0.830	0.772
volume (cm^3)	5.139	5.213	5.569	5.543	5.159
Density (g/cm^3)	3.848	3.847	3.846	3.845	3.839
Mass (g)	19.777	20.054	21.420	21.312	19.806

2.2.2 Spark Plasma Sintering

The spark plasma sintering experiments were conducted at the Arizona Materials Laboratory headed by Dr. Erica Corral. As seen in Figure 2.12, the set up in Arizona consisted of the Model 10-4 by Thermal Technology LLC. The Model 10-4 is capable of 10 tons of force and is accompanied by a 4000 amp power supply. The same set of powders already made back at ACM was weighed out and set into the dies. Similarly to the hot pressing, the insides of the dies were lined with graphite sheet and the powders were quickly packed before setting them inside the SPS machine. Through a trial run (set 1) of constant maximum temperature of 1600°C, the lowest temperature needed before the powder stopped compacting was taken by monitoring both the positional and temperature data feed. These were observed to be at 1550°C, 1500°C, 1450°C, 1450°C, 1450°C for the E, A, B, C, D blends respectively. The temperature ramp up was done at 100°C/min with a 5 minute hold at the max temperature. With the cooling process included, the entire procedure for making samples by SPS took roughly 30 minutes. The first two sets of sample production used a cooling rate of 100°C/min. Since cracking of the samples occurred, this was later adjusted to 50°C/min to see if cracks in the samples could be prevented. The pressure for the SPS set was set to 50 MPa for all the samples. Additionally, for the final set of SPS samples made, the powder was sieved further to 75 μm in hopes the finer powder would sinter more efficiently.

Figure 2.13 lists an example of all the data monitored during an SPS run. The data for position, temperature, volts, and amps were all simultaneously being gathered as a function of time. Values for the position variable can be seen slowly decreasing as the powder compacts due to the combined influence of temperature, pressure, volts, and amps. The pressure was not listed

here since it was constantly held at 50 MPa. The steps taken and parameters that were varied for all sample sets made can be seen in Table 2.4.

Figure 2.12: Spark Plasma Sintering (SPS) pressing apparatus in Arizona Model 10-4 manufactured by Thermal Technology LLC

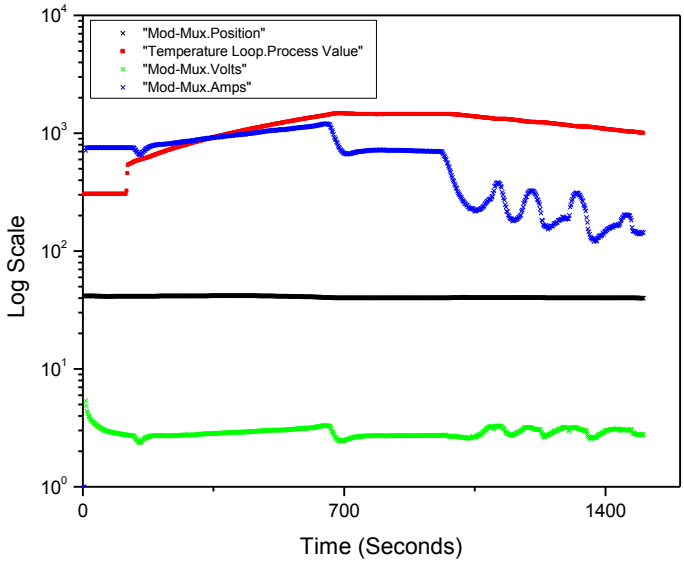

Figure 2.13: Temperature, voltage, and current output during Spark Plasma Sintering

Table 2.4: Spark Plasma Sintered Sample Compilation

SPS Samples	Max Temperature (°C)	Pressure (MPa)	Cool down rate (°C/min)	Extra Sieving
E1	1600	50	100	
A1	1600	50	100	
B1	1600	50	100	
C1	1600	50	100	
D1	1600	50	100	
E2	1550	50	100	
A2	1500	50	100	
B2	1450	50	100	
C2	1450	50	100	
D2	1450	50	100	
E3	1550	50	50	
A3	1500	50	50	
B3	1450	50	50	
C3	1450	50	50	
D3	1450	50	50	
E4	1550	50	50	Yes
A4	1500	50	50	Yes
B4	1450	50	50	Yes
C4	1450	50	50	Yes
D4	1450	50	50	Yes

2.2.3 Expected Microstructure of HP/SPS Samples

Contrary to the samples fabricated through extrusion, where the whiskers are oriented through being forced through a narrow die, in the case of HP/SPS, the whiskers are influenced by the pressure condensing the powder from the top and bottom directions. This leaves a random set of orientation in the xy-plane, but a stronger alignment perpendicular to the pressing direction [5,10,15]. Figure 2.14 depicts the expected microstructure for the HP and SPS samples and can be compared easily to the microstructure of the extruded samples listed earlier in Figure 2.3. The majority of the impedance measurements were done across the specimen thickness. The measurement arrangement is shown in the schematic of Figure 2.15.

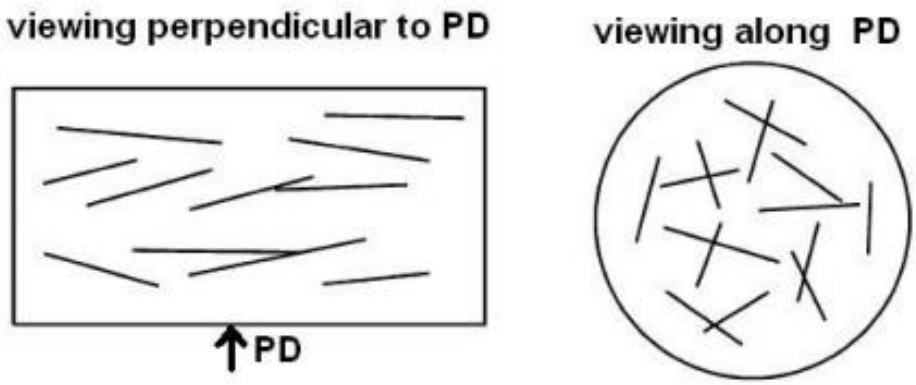

Figure 2.14: Schematics depicting whisker orientation common for both HP and SPS samples [1]

Figure 2.15: Measurement of sample through thickness

The SPS fourth set was studied in detail as it was the product of all the adjustments made throughout the previous SPS runs as described in Table 2.4. The sample dimensions of the fourth set are shown below in Table 2.5. Similarly to Table 2.3 which lists the HP sets made, the diameter, thickness, volume, density, and mass are shown.

Table 2.5: Geometric Properties for Samples Fabricated by SPS

	A4	B4	C4	D4	E4
Diameter (cm)	2.009	2.007	2.007	2.008	2.008
Thickness (cm)	0.340	0.344	0.332	0.333	0.329
volume (cm^3)	1.078	1.088	1.050	1.055	1.042
Density (g/cm^3)	3.848	3.847	3.846	3.845	3.839
Mass (g)	4.147	4.1867	4.04	4.055	3.999

2.3 Microstructural Characterization

2.3.1 Sample Polishing for Microscopy

Microscopy preparation included a grinding and polishing regimen, starting with 250 µm diamond discs which allowed fast removal of surface contaminants and surface roughness. This was followed up by 125, 70, 45, 15, and 6 µm discs respectively. During the diamond disc polishing, it is necessary to use a dressing stick at 5-10 minute intervals to help maintain the quality of the discs. Samples were always ground using a figure-eight motion applying some force from the fingers to maintain a good contact between the sample and the disc. At each stage of the polishing, the sample would be continuously ground for 1 to 2 minutes before changing the orientation of the sample by 90 degrees. Periodic changes in the orientation were necessary to

get the most uniform polishing possible. Once the scratches of the previous disc were overwritten completely by the new disc, it was safe to move on to the next size disc. After going through all the steps of diamond disc polishing, the final preparation was completed using diamond paste ranging from 3, 1, and 0.25 μm using MicroCloth made by Buehler. Instead of using water for the diamond paste, MetaDi suspensions were used because they help lubricate the surface and dissipate heat. This sample polishing process emphasizes the interfaces between the matrix and the whiskers and allows them to be detected in the SEM more easily.

2.3.2 Scanning Electron Microscopy (SEM)

SEM was one of the two main methods used to study the microstructure of this composite system. The majority of images were taken with the Zeiss Ultra60 FE-SEM shown in Figure 2.16. Once the fully polished samples were prepared, they could be put into the vacuum chamber and inserted into the chamber of the SEM once fully pumped. The high efficiency In-lens SE detector was used for high contrast surface imaging. The equipment apparatus can be seen in the image below. An accelerating voltage of 5kV was used for the majority of the images reported in this thesis. Magnifications vary across images taken but most were in the range of 1k to 20k. It was important to use a close working distance between the sample and the emission source in order to obtain the highest quality images. However, risking the safety of the equipment was not an option, so the minimum working distance of 4mm was never crossed and 5mm working distance was usually good enough to maintain high quality images.

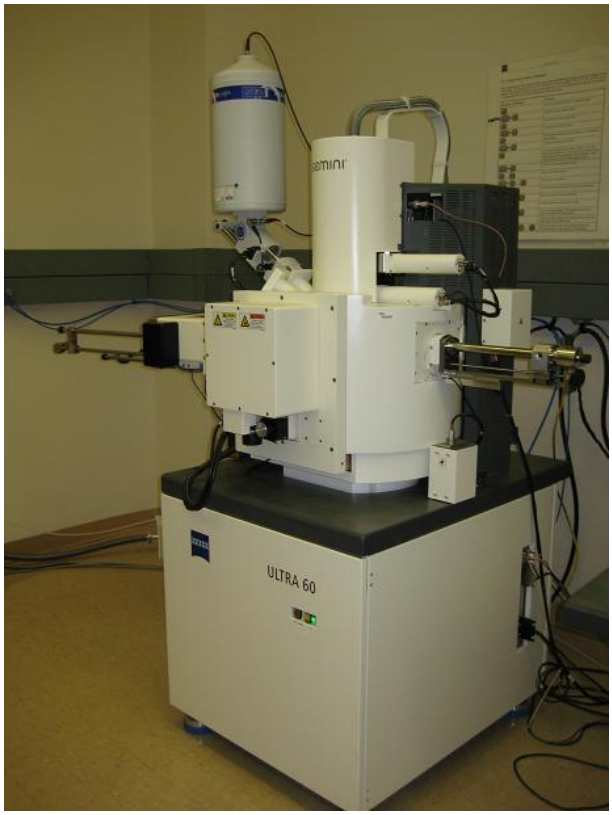

Figure 2.16: Zeiss Ultra60 FE-SEM located in the Marcus Cleanroom at Georgia Tech [40]

2.3.3 Atomic Force Microscopy (AFM)

The AFM was a secondary microscopy technique used to supplement the images gathered by using the SEM. The AFM is a piece of equipment with a lot of potential capable of measuring conductors, non-conductors, and even some liquids. Sample preparation for AFM is not highly demanding, meaning the previous SEM sample preparation was adequate for imaging. The specific piece of equipment used is the Park Systems XE-100E AFM shown in Figure 2.17. The optical microscope included in this machine helps approach the tip to the sample safely without crashing and breaking the tip. As the diagram in Figure 2.18 shows, it is necessary to center the laser off the tip and mirrors in order to get proper feedback [41]. Once the tip is properly approached, the topography, amplitude, and phase are among the responses looked at while trying to perfect the image. Figure 2.19 shows the probe scanning the sample surface after

the tip has fully been approached. Scan sizes for the AFM are much more limited than for the SEM with the maximum scan size being 40 μm by 40 μm. However, most scans were done on a smaller scale focusing solely on imaging whiskers which dimensions are on the order of 5-50 μm and 0.2-1.0 μm for the lengths and diameters respectively. Scans were done using noncontact AFM which measures tip oscillation while the tip is a few nanometers away from the surface, still in the net attractive regime of interatomic force.

2.3.3.1 Current Atomic Force Microscopy (I-AFM)

Current AFM which expands on the capabilities of an AFM by running a current through the sample is able to detect conducting paths through the sample [13,42,43]. The approaching method for the tip is the same, but a specialized tip for current AFM is necessary. Scan size was again very narrow only spanning 2 μm by 2 μm focusing on whisker behavior alone. A tip bias of 10V in combination with the external current amplifier set at 10^8-10^{11} was necessary to garner a response [13].

Figure 2.17: Park Systems XE-100 AFM [44]

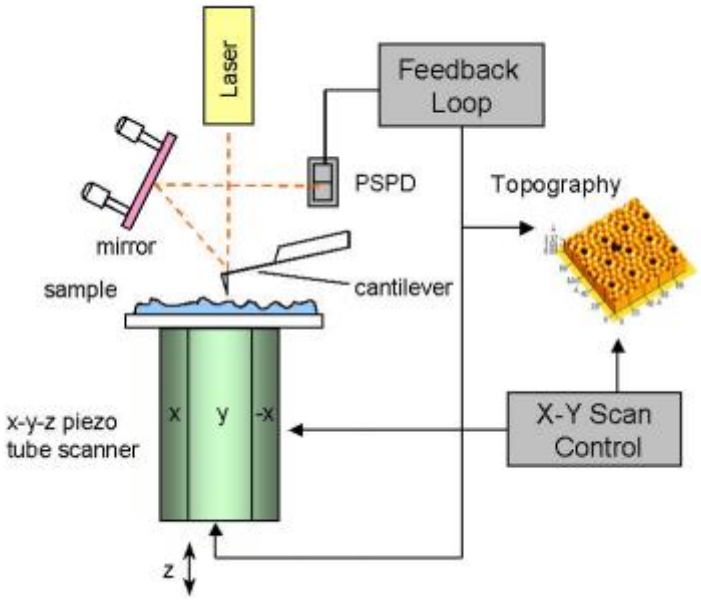

Figure 2.18: Diagram for AFM scanning interactions within apparatus [41]

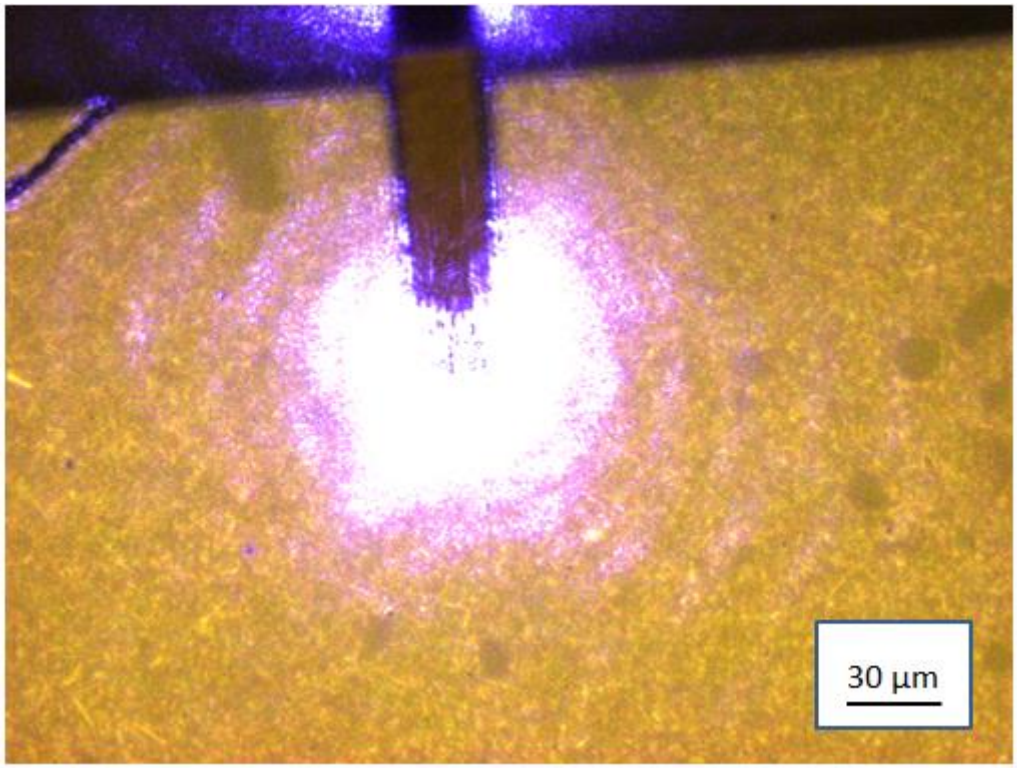

Figure 2.19: AFM cantilever and tip scanning directly over sample microstructure

2.4 Impedance Testing Preparation

2.4.1 Sample Electroding

Depending on the form of impedance measurement, the sample preparation differed slightly. A combination of the Solartron 1260/1296 was used for data gathering. In the case of the in-plane measurements of the pressed surface, nothing more than initial polishing was needed. However, in order to measure the electrical response through the thickness of thicker samples silver paint electrodes became necessary. Silver paint and sputtered silver were used as electrodes [13]. This is to evaluate the impedance data in an effective manner.

The silver paint was simply applied to the sample surface using a brush, making the smoothest surface possible and later checking the quality of the coating using a multimeter. The sputter coating on the other hand was a slightly more complex process that requires a sputtering machine. The sputter coater model used is the Denton Vacuum Desk II TSC turbo sputter coater shown in Figure 2.20. Once the samples are placed within the sputter coater, the sputtering process begins with the usage of argon gas to serve as the environment within the coater. It is important to adjust the gas so that a stable 50 millitorr is maintained during the process. The coating period lasts for just over 15 minutes which is set using the manual timer at 999 seconds. Once completed, the machine powers down and after turning off the gas the samples can be removed. Covering the sides of the sample with tape helped avoid the entire sample being sputtered and ensured the measuring of the properties across the thickness of the sample. Similarly, the coating was checked using a multimeter for the sputter coatings as well.

Figure 2.20: Turbo sputter coater used to apply sputtered silver electrodes

2.4.2 Electrical Measurements of Samples

The Solartron 1260 Impedance Analyzer and 1296 Dielectric Interface as seen in Figure 2.21 were used together to conduct these measurements. The frequency range used for the samples spanned several orders of magnitude from 10MHz to 10 mHz. The AC voltage was set to 0.5V in the parallel to hot pressing direction for all scans. The samples with the newly applied electrodes were held in place using electrical fixtures that are able to adjust to the geometry of the samples [1]. The fixture on the left in Figure 2.22 was a homemade fixture using a gripping device, two epoxy pucks with protruding SEM-like stubs for electrodes, and connections made with alligator clips. The long extruded rods were measured using a separate, similar custom-built fixture using a larger gripping device shown on the right in Figure 2.22. Measurements were also

made using a superimposed DC bias to help isolate responses due to the electrode from the bulk samples [13].

Figure 2.21: Solartron 1260 Impedance Analyzer and 1296 Dielectric Interface

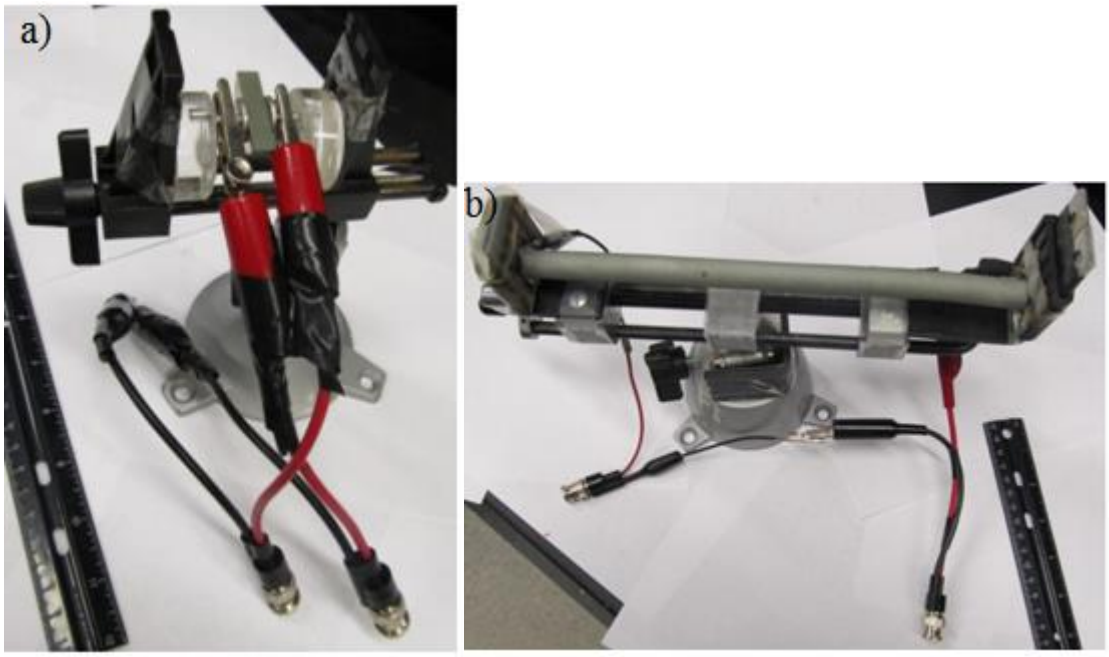

Figure 2.22: Electrical fixtures used to measure cut samples and full length extruded rods [1]

2.4.3 Data manipulation

In order to analyze the data taken from the Solartron, a combination of programs such as Zview and Origin were used. Zview is able to look at frequency explicit and implicit plots among all the dielectric functions (these include impedance, admittance, modulus, and permittivity). The program can be used to construct equivalent circuits in order to fit the measured spectra [21]. Origin was used to construct figures in a clear and concise manner with better quality labels.

Chapter 3

Results on Characterization of Extruded Rod Samples

This chapter is the first of the two highlighting the results gathered through the experiments conducted for this study. The extruded samples were studied in four separate sections including full rod measurements, rod sectioning into smaller components, evaluation of the anisotropic microstructure, and characterization of thin sections.

3.1 Full Rod Measurements of 20% SiC_w-Al_2O_3 Samples

A total of eight full length extruded rods averaging 25.60 cm in length were measured to investigate the variance across multiple extruded samples. These are the full length rods of extruded samples containing 20% SiC_w mentioned in Table 2.1. By looking at a number of parameters with respect to frequency, as seen through a number of figures seen in this chapter, the differences among the samples become more apparent. Figure 3.1a presents the relationship between impedance magnitude measured in ohms-cm, due to the normalization of slightly varied rod lengths, and frequency. While variations are visible across different bars, the amount of information capable of being derived from Figure 3.1a along with Figure 3.1b, where the theta values are being compared against the frequency, is limited.

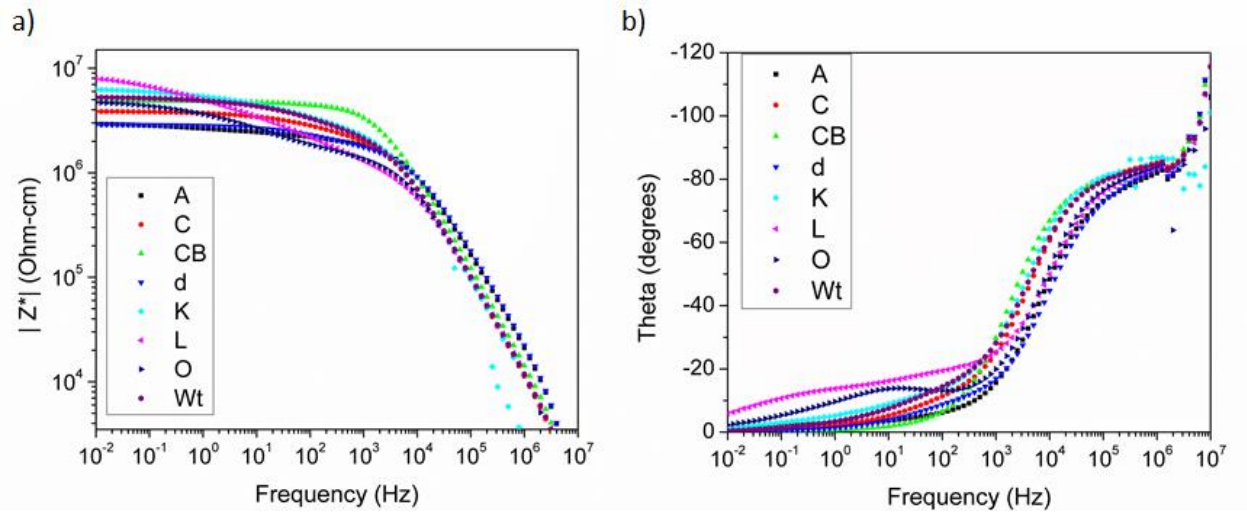

Figure 3.1: (a) |Z*| vs. Frequency, (b) Theta vs. Frequency for eight separate extruded ceramic composite rods

Figure 3.2 describes the low frequency resistance values across all full length extruded rods. The majority of the rods are near the average value with the largest response coming from the 20L rod, which has roughly twice the average value. The lowest resistance value from rod 20A came out to be just under a quarter of the average value. However, all things considered, the total range in responses is less than an order of magnitude. The variability across different rods is present, but is relatively confined. On the other hand, the differences indicate that the rods must have slightly different arrangements of SiC whiskers.

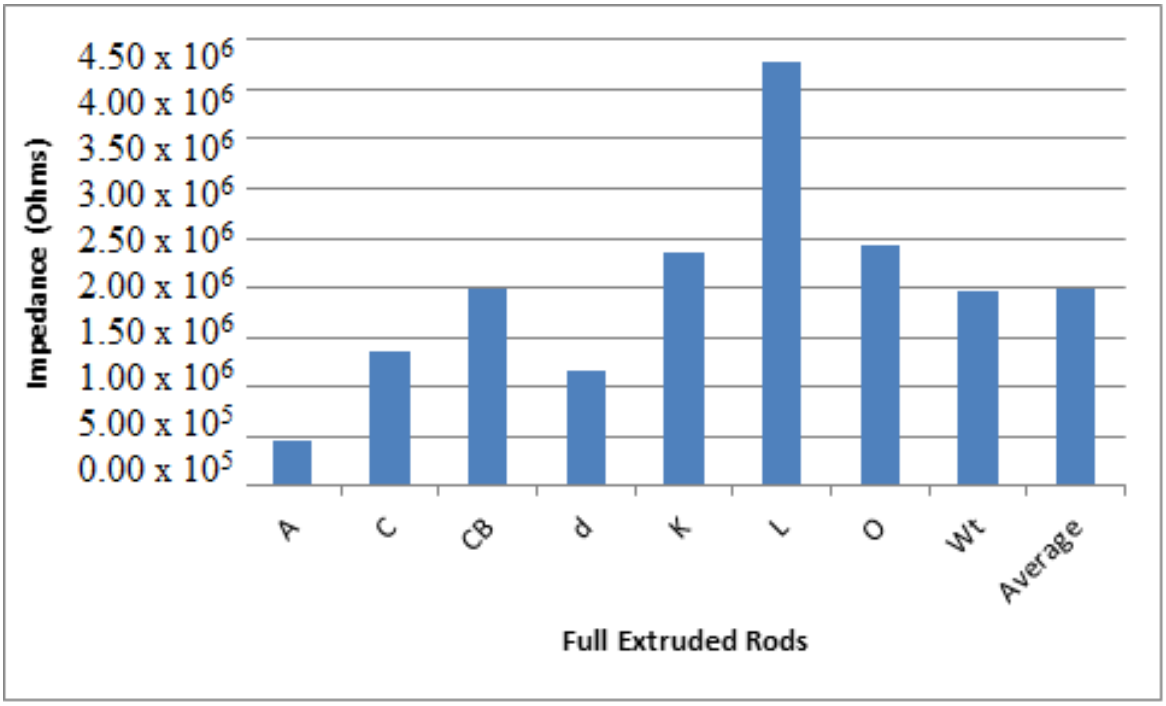

Figure 3.2: Low frequency resistance value histogram comparison

Figure 3.3a and Figure 3.3b display the real resistivity and imaginary resistivity versus frequency respectively. The variations in response across full length rods are more apparent in this figure compared to Figure 3.1a. Furthermore, the imaginary resistivity serves to showcase these changes in the most visible manner. All rods exhibit a major peak in the 10^3-10^4 Hz frequency range. Rods also exhibit another peak in a wider frequency region 10^{-2} to 10^2. Not only is the frequency range for this peak behavior wider, the size in which it manifests itself is highly dependent on the rod. Rod 20L especially showcases this behavior as the low frequency peak is higher in magnitude than the 10^3-10^4 Hz frequency range peak and this abnormal behavior carries on into the rod sectioning which will be discussed in section 3.2.

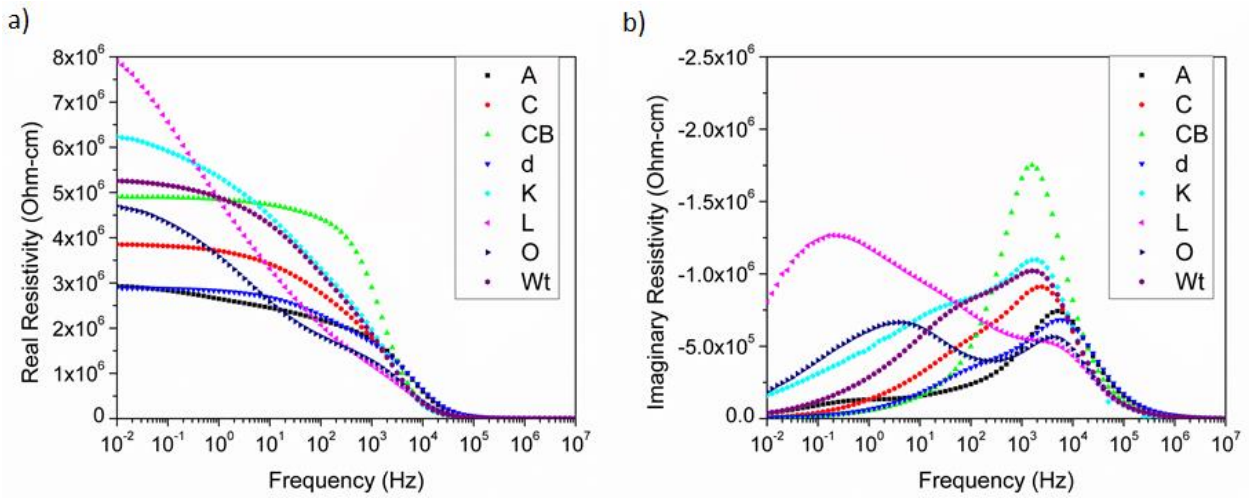

Figure 3.3: a) Real Resistivity vs. Frequency, b) Imaginary Resistivity vs. Frequency for eight full rods

Figure 3.4 presents a complex Z* plot, where Z'' is plotted vs Z'. Although the frequency is not available directly on one of the axis, its change can be seen as the points are followed leaving the origin. The high frequency starts at the origin and the frequency gradually decreases as the data points dip towards the x-axis. Rod 20L again emerges out of the pack as the sample with differing behavior, but rod 20CB stands out as well due to its large imaginary component relative to the other full length rods.

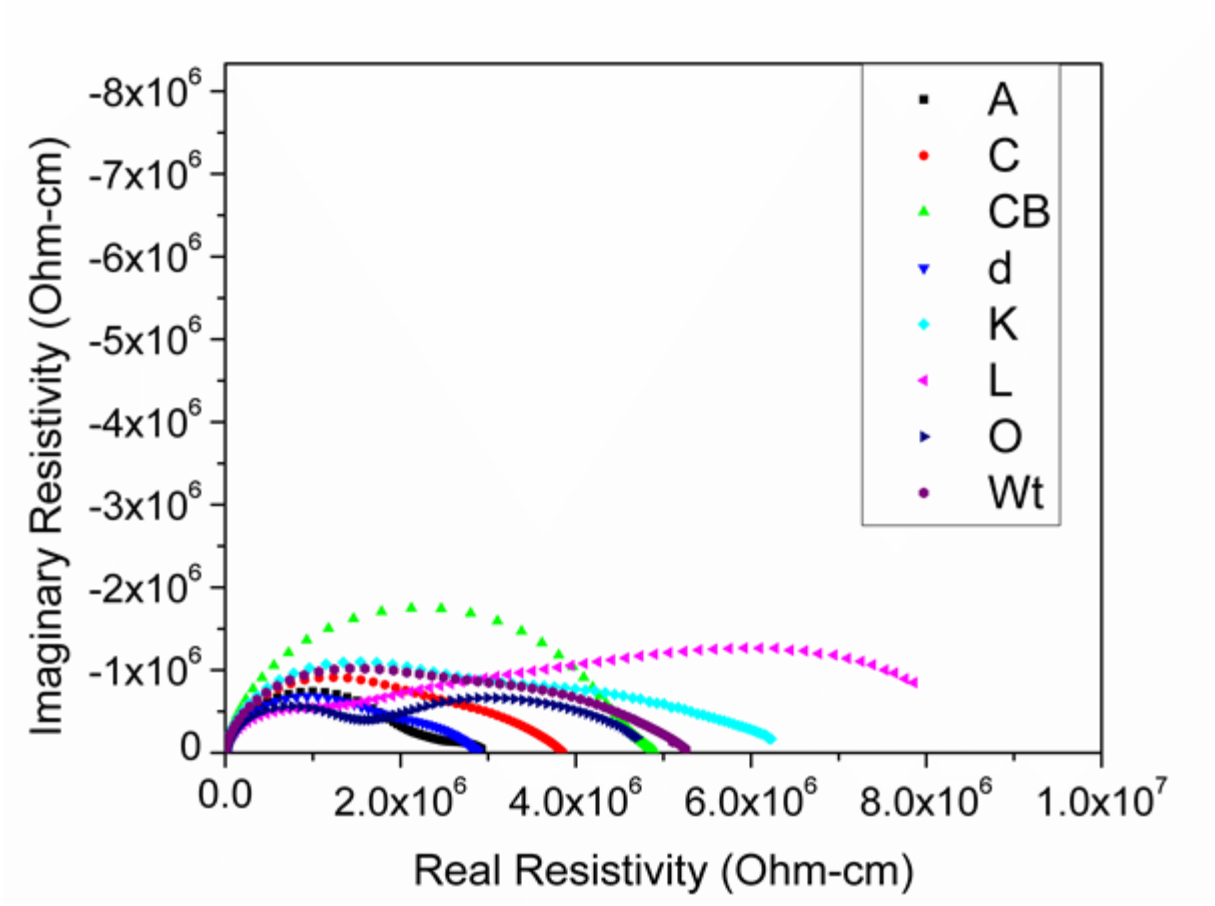

Figure 3.4: Imaginary Resistivity vs. Real Resistivity across all full length extruded rods

Figure 3.5 displays the same data plotted in Figure 3.4 after its transformation into the electric modulus following Equation (2) and Equation (3). What Figure 3.5 illustrates, which is not as apparent in the previous figures, is the unique behavior of rod A and rod D in the modulus function. Their response in both the real and imaginary modulus is roughly twice the values of the rest of the rods. When looking solely at the shapes of the curves, they are extremely similar. This similarity will be shown once again in Figure 3.6 where the imaginary impedance and imaginary modulus are compared after normalization. The major peak in the imaginary modulus shown in both Figure 3.5a and throughout all of Figure 3.6 occurs at around 10^4 Hz. As consistent as the imaginary modulus peak response is, the imaginary impedance response does

not follow the same trend for all of the samples and shows a couple different types of behavior instead of it. Rods A, C, CB, D, K, and Wt share a similar behavior with the largest peak and a slightly smaller buried peak working in conjunction around the 10^2 to 10^4 Hz frequency ranges. Another set of behaviors can be observed for rods 20L and 20O, where the largest clear peak can be seen at a much lower frequency (10^{-1}- 10^1 Hz) than for the other set of rods. In order to show the different contributions to the total response, it is necessary to break up the overall peak into several components. More detail on how these peaks come together will be described in Figure 3.7. The imaginary impedance peak is made up of at least three different peaks in all cases, whereas the modulus peak can be fitted by one or possibly two separate peaks.

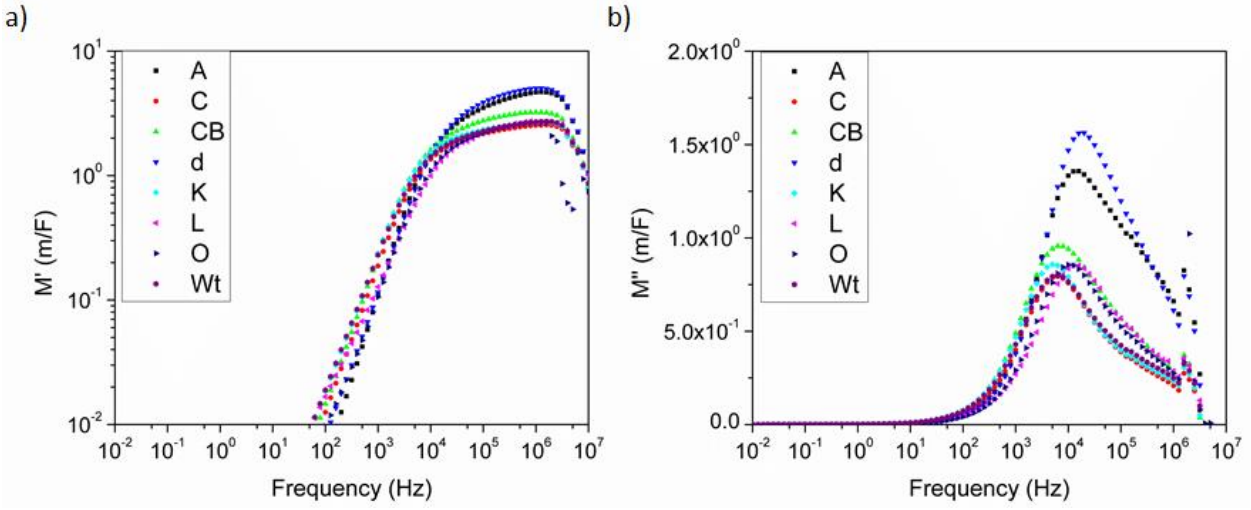

Figure 3.5: a) Real Modulus vs. Frequency, b) Imaginary Modulus vs. Frequency of eight different full length rods

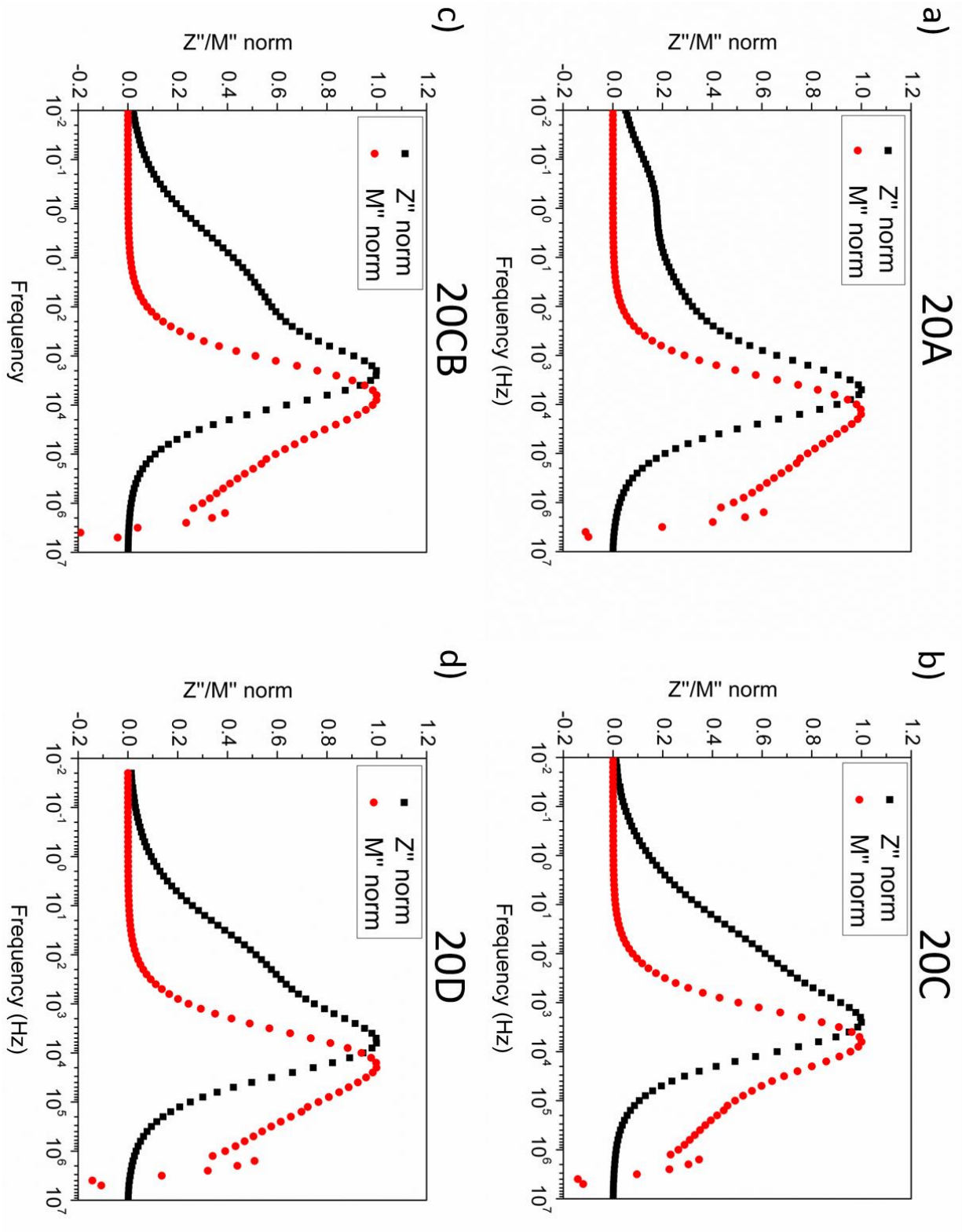

Figure 3.6.1: Normalized Z'' and M'' vs. Frequency for full length rods A, C, CB, and D for a) – d) respectively

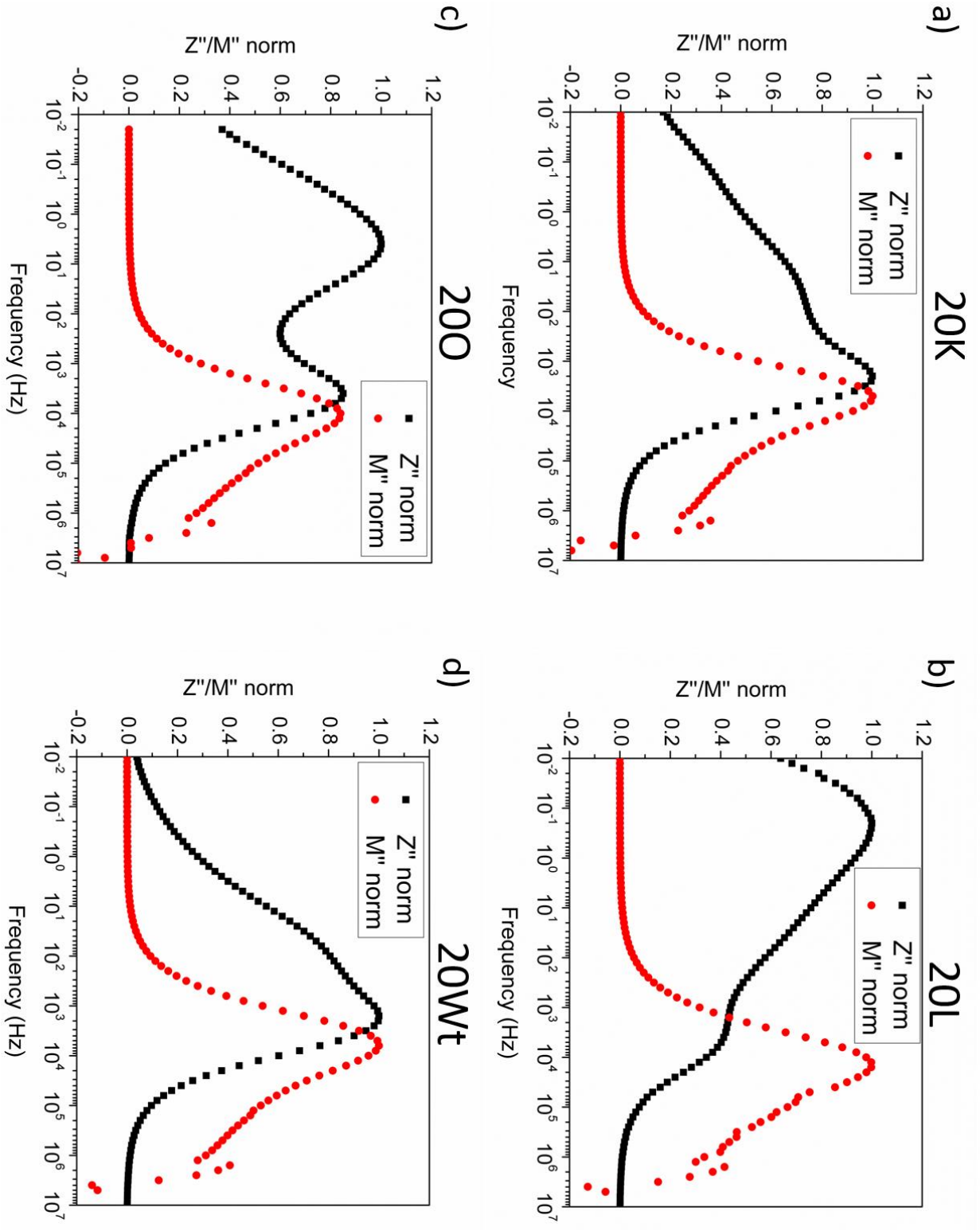

Figure 3.6.2: Normalized Z'' and M'' vs. Frequency for full length rods K, L, O, and Wt for a) – d) respectively

Figure 3.7 shows an example of what the behavior of multiple peaks can look like under the entire imaginary impedance response obtained from a full length extruded rod. Initial assessments of number of peak estimates may not be always correct as smaller peaks working in conjunction may be the cause of the behavior as a whole. Once these peaks are all superimposed together, they should reflect the imaginary impedance data as a whole.

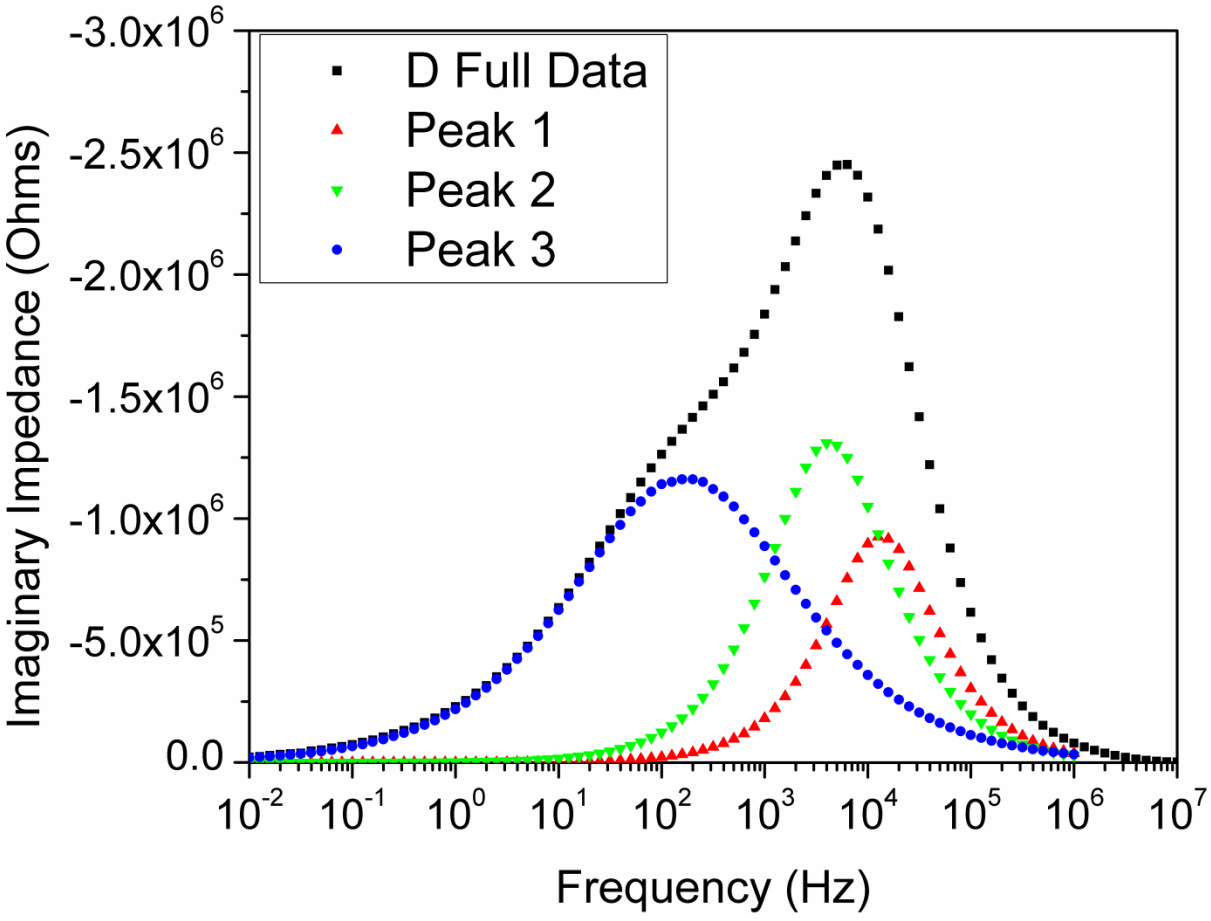

Figure 3.7: Peak breakdown of extruded rod D for the impedance data

Table 3.1: Individual Breakdown for All Three Impedance Peaks Along with the Main Modulus Peak

	Z''_{P1} (Ω)	$F_{Z''P1}$ (Hz)	Z''_{P2} (Ω)	$F_{Z''P2}$ (Hz)	Z''_{P3} (Ω)	$F_{Z''P3}$(Hz)	M''_{P}(m/F)	$F_{M''P}$ (Hz)
20A	2.39×10^{6}	6.31×10^{3}	5.85×10^{5}	3.68×10^{2}	4.51×10^{5}	1.36×10^{0}	1.47×10^{4}	1.36×10^{0}
20C	2.05×10^{6}	4.30×10^{3}	1.47×10^{6}	7.94×10^{2}	1.36×10^{6}	3.98×10^{1}	6.31×10^{3}	7.94×10^{-1}
20CB	n/a	n/a	n/a	n/a	n/a	n/a	5.41×10^{3}	7.75×10^{-1}
20D	9.27×10^{5}	1.36×10^{4}	1.31×10^{6}	4.30×10^{3}	1.16×10^{6}	1.71×10^{2}	1.85×10^{4}	1.57×10^{0}
20K	2.95×10^{6}	3.41×10^{3}	2.41×10^{6}	2.92×10^{2}	2.36×10^{6}	3.98×10^{0}	4.64×10^{3}	7.70×10^{-1}
20L	1.31×10^{6}	5.84×10^{3}	1.76×10^{6}	1.08×10^{2}	4.27×10^{6}	2.93×10^{-1}	1.47×10^{4}	8.55×10^{-1}
20O	1.01×10^{0}	8.58×10^{3}	1.04×10^{6}	2.00×10^{3}	2.42×10^{6}	3.41×10^{0}	1.08×10^{4}	8.57×10^{-1}
20Wt	2.45×10^{6}	3.69×10^{3}	1.96×10^{6}	3.98×10^{2}	1.97×10^{6}	1.59×10^{1}	6.31×10^{3}	7.99×10^{-1}

Table 3.1 summarizes both the frequency and impedance values for each peak so they can easily be compared across different full length extruded rods. Additionally, the modulus peak and frequency for all rods are listed here as well. Out of the three impedance peaks present, two occur in a narrow regime between 10^2 and 10^3 Hz. The final peak is a couple of orders of magnitude away somewhere in between 10^0 and 10^1 Hz on average. The impedance peak values on the other hand remain within the 10^6 Ohm regime with few exceptions regardless of the peak. So in summary, the peaks may manifest themselves at different frequencies, but their magnitudes

are very similar. This is as would be expected since these peaks probably represent similar responses in the percolated network.

Data fitting of the experimental peaks can be accomplished by using physically meaningful equivalent circuits. The equivalent circuit that fits the experimental data has six main components and is shown in Figure 3.8. These include a leading resistor, 3 RC elements in parallel, followed by one RL parallel element, and finally another RC element in parallel set below the main path of circuits. The 3 RC elements seem like they could be a single entity but in reality they do exist as 3 separate parallel RC elements in series (as already described by the presence of three peaks in the imaginary impedance). This is showcased by the peak breakdown that when put together forms the majority of the impedance response as a whole. By super imposing peaks 1 through 3 of Figure 3.7, the data that would be seen as those seen in Figure 3.3b emerge. Note the different frequency ranges in which each RC element in parallel dominates. These are indicators of the different electrical pathways taking part within the extruded rods and can possibly be attributed to varying whisker densities across the rods. A leading resistor represented by R_L exists to account for the distance from the origin the high frequency data occupies when leaving the x-axis. This value was often times negative as illustrated in Tables 3.2 through Table 3.5. The RL parallel element was instrumental in better fitting the high frequency modulus data. The amount of activity within the higher frequency regimes has been observed in both Figure 3.6 and to be shown in Figure 3.11. The final RC parallel elements labeled as 4 represent the alternate pathway for the electrical current to flow within the alumina matrix. While the option exists within the circuit, it is not a preferred path due to the vast difference in electrical conductivity between the Al_2O_3 and SiC_w.

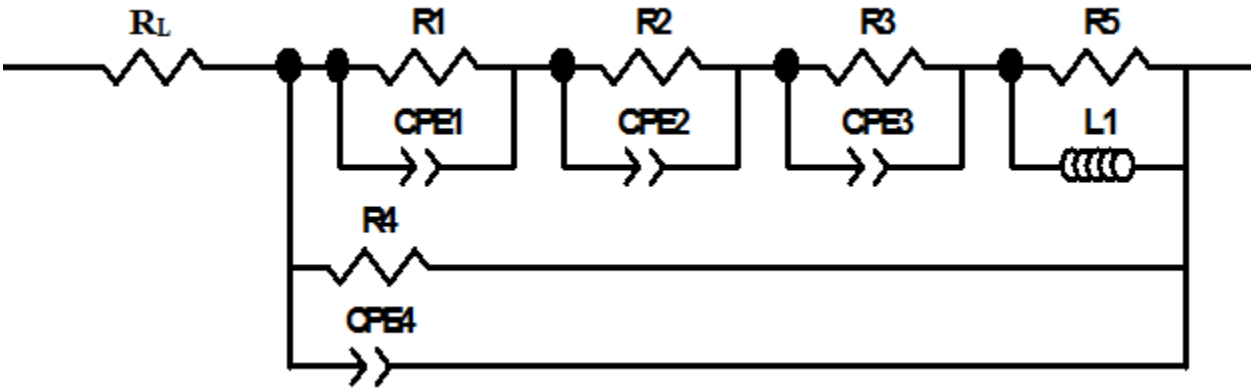

Figure 3.8: Equivalent circuit used in modeling impedance data for extruded rod samples

3.2 Breakdown of Full Rods

Two rods, 20C and 20L, were selected from the samples analyzed in section 3.1 to undergo the rod sectioning into smaller constituents. This process was aimed at observing differences in variability across the full length extruded rods. The electrical reponse of all the cut sections for rods 20L and 20C are presented in Figures 3.9 and 3.10 respectively. Parts (a) and (b) give the response of the full rod and the half cut rods respectively, while parts (c) and (d) display the measured response of the quarter and eighth rod measurements.

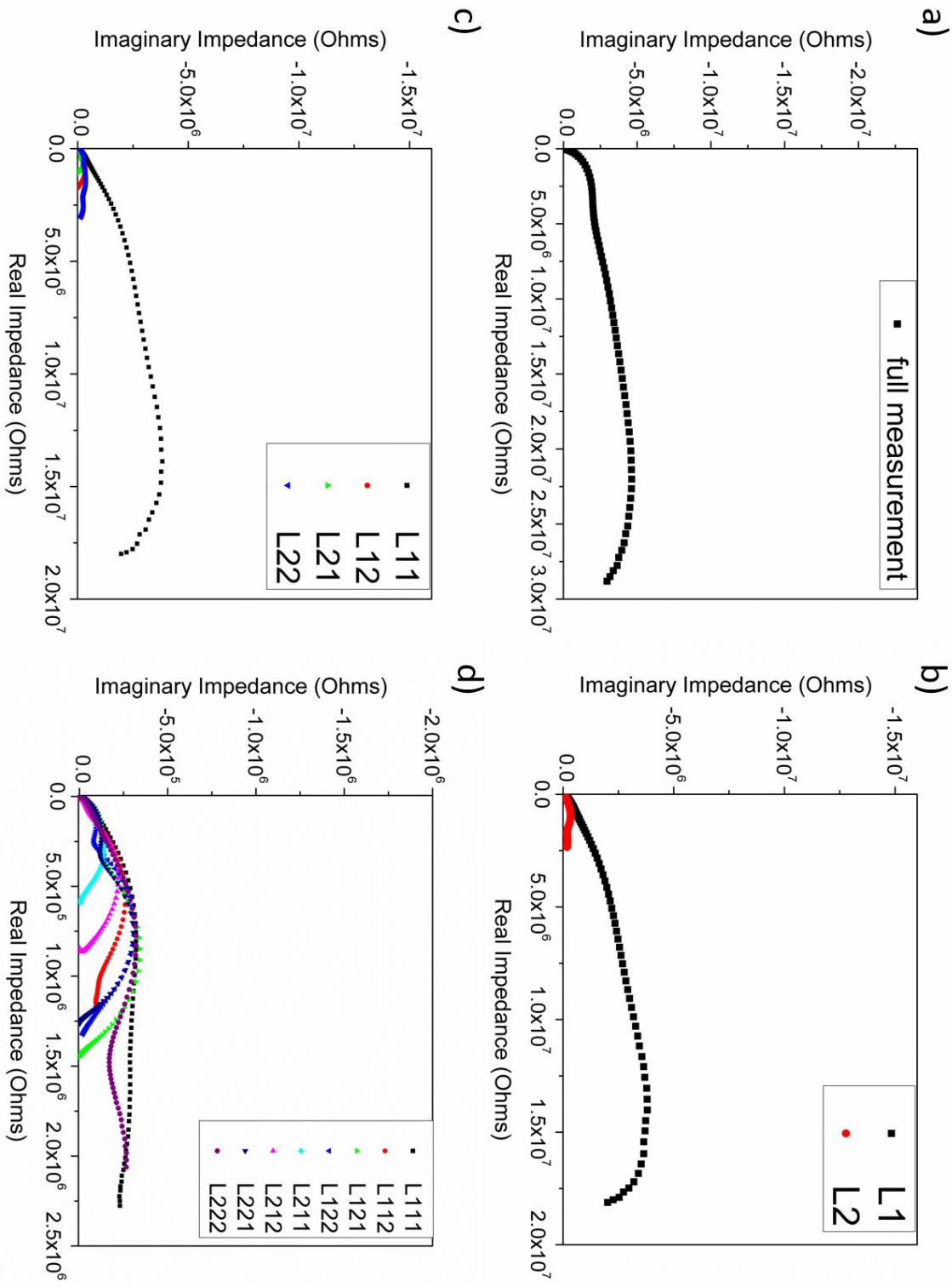

Figure 3.9: a)-d) Complex impedance graphs for the full, halves, fourths, and eights respectively of the extruded rod 20L consisting of alumina with SiC_w measured using impedance spectroscopy [35]

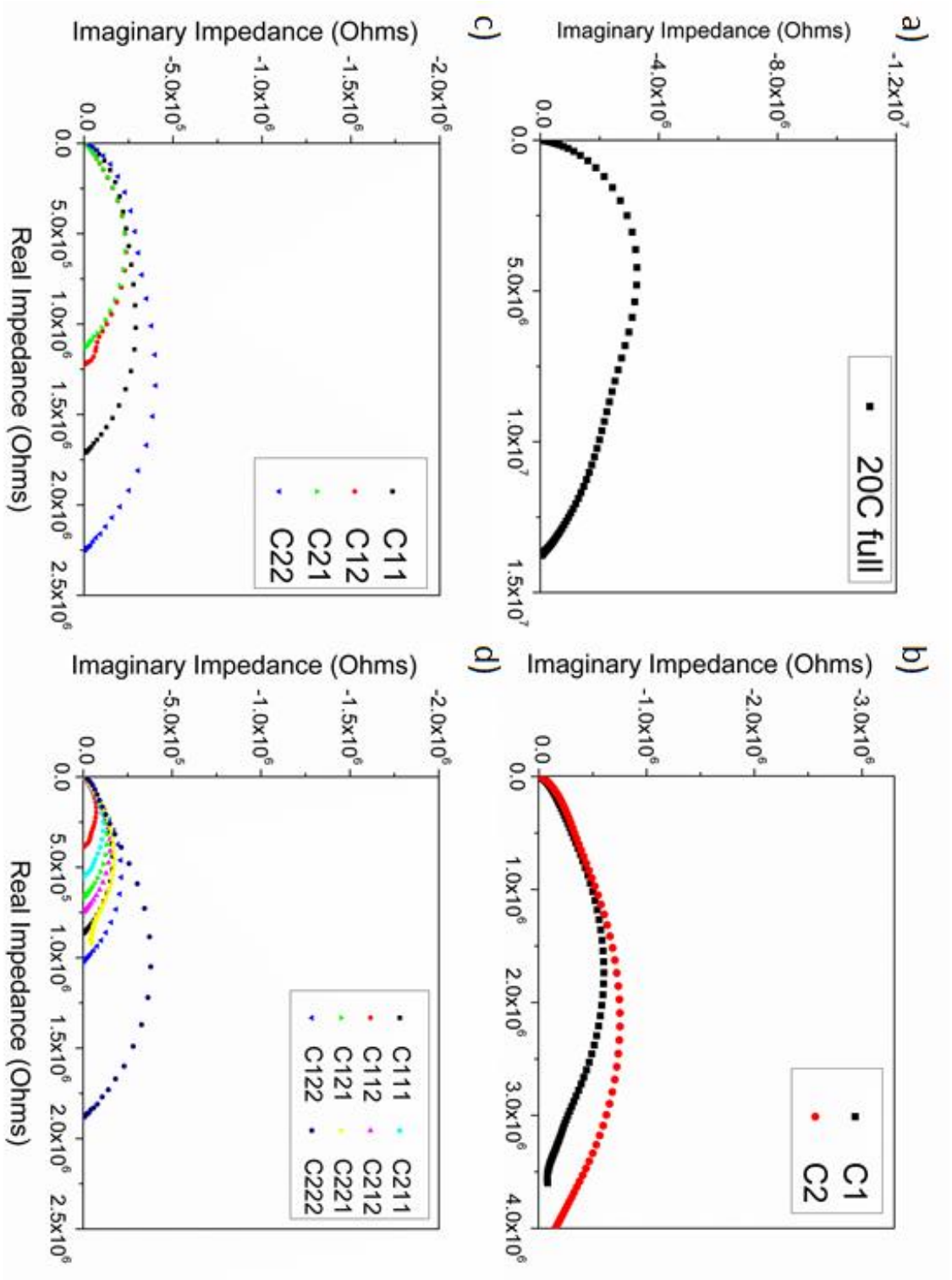

Figure 3.10: a)-d) Complex impedance graphs for the full, halves, fourths, and eights respectively of the extruded rod 20C consisting of alumina with SiC_w measured using impedance spectroscopy

The rod breakdowns depicted in Figures 3.9 and 3.10 tell compelling yet different stories between the two separate rods. When the 20L rod was first sectioned into halves (see Figure 3.9b), a stark difference emerged between the two halves. The first half was almost a full order of magnitude more resistive than its counterpart. This behavior of one slice being much more resistive compared to the others continued into the fourths again with a difference of roughly an order of magnitude. However, by the time the samples were reduced into eighths pieces, the difference is minimized although it is still detectable. It is important to note that with each cut made to the rod, there is a finite amount of material being lost to the saw. This effect becomes more and more significant as the rod is cut down into smaller and smaller pieces as the number of cuts necessary doubles with each step. Within these areas consumed by the saw, the possibility of particularly insulating whisker formations or lack thereof may be present. Once removed, the results of the measurements may become more conducting and show more similar responses.

On the other hand, the 20C rod showed much less variability across the rod than the 20L rod. The two halves exhibit similar behavior with the difference well within a couple percent (see Figure 3.10b). Maximum differential in the fourth measurements is roughly two times difference and similarly the eighths do not exceed a 4 times difference across all eight samples. So while variability does exist throughout the rod, this example is much more homogeneous than the 20L rod, since the differences for the halves, fourths, and eighths are quite small with a few exceptions (see Figure 3.10c and Figure 3.10d).

It is imperative to mention the extreme repeatability of these impedance measurements. If multiple scans are taken from the same sample under the same conditions, the results will be nearly identical without fail. Some factors and conditions capable of influencing the results

include humidity [45] and electrode aging [13]. Humidity is more likely to affect the properties when the material is porous and a dielectric [46] in the composites, whereas electrode aging can affect the interface properties with the electrode [13].

The fitted equivalent circuit value breakdown for the 20L full bar, the halves, the fourths, and the eighths sized samples can be seen in Table 3.2. This table helps elucidate the variability among the different cuts but also the overall consistency observed across all samples by taking an average and standard deviation for the different sized portions as depicted in Table 3.3. The average and standard deviation across all circuit elements are within an order of magnitude or less. This showcases that the property distribution across the different sections of the rod are relatively narrow, yet not exactly the same.

Table 3.2: Circuit Fits Across All Full Rod and Different Sample Lengths for the 20L Extruded Rod Breakdown

20L	R_L	R1	CPE1-T	R2	CPE2-T	R3	CPE3-T
full	-1.31×10^{4}	3.36×10^{6}	1.90×10^{-11}	2.03×10^{7}	2.89×10^{-8}	6.64×10^{6}	1.41×10^{-9}
L1	-1.92×10^{4}	6.61×10^{6}	9.89×10^{-9}	1.35×10^{7}	6.60×10^{-8}	5.65×10^{5}	1.32×10^{-9}
L2	-7.76×10^{3}	1.40×10^{6}	1.21×10^{-8}	1.10×10^{6}	1.34×10^{-6}	2.02×10^{5}	3.09×10^{-9}
L11	-1.32×10^{4}	6.16×10^{6}	8.08×10^{-9}	1.36×10^{7}	6.16×10^{-8}	4.74×10^{5}	5.70×10^{-10}
L12	-5.03×10^{3}	1.32×10^{6}	2.12×10^{-8}	2.91×10^{5}	8.78×10^{-10}	1.56×10^{5}	8.03×10^{-6}
L21	-4.29×10^{3}	7.51×10^{5}	1.27×10^{-8}	3.26×10^{5}	6.39×10^{-10}	2.08×10^{4}	3.61×10^{-5}
L22	-7.62×10^{3}	1.40×10^{6}	1.06×10^{-8}	5.88×10^{5}	1.59×10^{-10}	1.25×10^{6}	5.89×10^{-7}
L111	-2.30×10^{3}	1.12×10^{5}	2.98×10^{-8}	9.53×10^{5}	2.29×10^{-8}	1.48×10^{6}	5.30×10^{-7}
L112	-4.70×10^{3}	7.77×10^{4}	1.22×10^{-8}	9.17×10^{5}	2.58×10^{-8}	1.00×10^{20}	7.78×10^{-6}
L121	-9.45×10^{2}	1.34×10^{5}	3.38×10^{-10}	1.11×10^{6}	1.11×10^{-8}	1.83×10^{5}	8.37×10^{-10}
L122	-6.33×10^{2}	7.24×10^{4}	1.55×10^{-10}	1.06×10^{6}	2.01×10^{-8}	1.60×10^{5}	3.10×10^{-10}
L211	-1.31×10^{3}	3.80×10^{4}	1.25×10^{-8}	1.13×10^{5}	8.77×10^{-9}	4.33×10^{5}	1.02×10^{-7}
L212	-1.79×10^{3}	8.36×10^{4}	1.24×10^{-8}	1.40×10^{5}	2.07×10^{-8}	6.48×10^{5}	4.99×10^{-8}
L221	-2.31×10^{3}	3.15×10^{5}	4.41×10^{-10}	3.80×10^{5}	8.07×10^{-9}	5.60×10^{5}	4.59×10^{-8}
L222	-4.99×10^{3}	9.51×10^{4}	2.79×10^{-9}	1.38×10^{6}	2.85×10^{-8}	1.26×10^{6}	3.19×10^{-6}

Table 3.3: Average and Standard Deviation Values Across All Stages in Sample Sectioning for Rod 20L

20L	R_L	R1	C1	R2	C2	R3	C3
Full	-1.31×10^{4}	3.36×10^{6}	1.90×10^{-11}	2.03×10^{7}	2.89×10^{-8}	6.64×10^{6}	1.41×10^{-9}
Average	-1.35×10^{4}	4.00×10^{6}	1.10×10^{-8}	7.31×10^{6}	7.02×10^{-7}	3.83×10^{5}	2.20×10^{-9}
Halves	$\pm8.10\times10^{3}$	$\pm3.68\times10^{6}$	$\pm1.60\times10^{-9}$	$\pm8.79\times10^{6}$	$\pm9.00\times10^{-7}$	$\pm2.57\times10^{5}$	$\pm1.25\times10^{-9}$
Average	-7.55×10^{3}	2.41×10^{6}	1.31×10^{-8}	3.71×10^{6}	1.58×10^{-8}	4.76×10^{5}	1.12×10^{-5}
Fourths	$\pm4.06\times10^{3}$	$\pm2.52\times10^{6}$	$\pm5.68\times10^{-9}$	$\pm6.62\times10^{6}$	$\pm3.05\times10^{-8}$	$\pm5.51\times10^{5}$	$\pm1.70\times10^{-5}$
Average	-2.37×10^{3}	1.16×10^{5}	8.83×10^{-9}	7.56×10^{5}	1.83×10^{-8}	6.75×10^{5}	5.60×10^{-7}
Eighths	$\pm1.64\times10^{3}$	$\pm8.52\times10^{4}$	$\pm1.02\times10^{-8}$	$\pm4.78\times10^{5}$	$\pm7.91\times10^{-9}$	$\pm5.13\times10^{5}$	$\pm1.17\times10^{-6}$

A similar set of tables have been made for the measurements of the different parts for extruded rod 20C during its sectioning. Table 3.4 lists the circuit fits directly, while Table 3.5 lists the tabulated values for the average and standard deviation of each step. Once again, the standard deviation values are often smaller than the average value and never more than an order of magnitude away from each other. This reinforces the notion of variability always being present, but the core identity of the material system itself will limit the bounds in which this variability can occur.

Each component of this equivalent circuit must represent something present in the microstructure. While, the lowest frequency response may be attributed to the electrode effect [13], the remainder of the circuit elements must describe the bulk response of the sample. The two sets of RC elements in parallel may be able to be attributed to the whiskers themselves and the junctions between whiskers. It is clear that the behavior of the whiskers alone does not have a constant value. However, this may be a result of the whiskers shapes also contain variability in them as well, as previously described in chapter 2. Another possibility is that a different distribution of whisker densities is present through the thickness of the various samples measured [16]. Whisker interconnectivity is highly influenced by sample processing and the impedance values reflect this as the results in Chapter 4 concerning HP and SPS samples will show.

Table 3.4: Circuit fits Across All Sample Lengths for the 20C Extruded Rod Breakdown

20C	R_L	R1	CPE1-T	R2	CPE2-T	R3	CPE3-T
full	$-4.31x10^{3}$	$4.54x10^{6}$	$1.46x10^{-11}$	$4.16x10^{6}$	$1.14x10^{-10}$	$4.90x10^{6}$	$5.60x10^{-9}$
C1	$-3.72x10^{4}$	$2.82x10^{5}$	$3.66x10^{-9}$	$2.94x10^{6}$	$1.09x10^{-8}$	$6.40x10^{5}$	$2.27x10^{-6}$
C2	$-3.42x10^{4}$	$3.04x10^{5}$	$6.75x10^{-10}$	$3.75x10^{6}$	$9.31x10^{-9}$	$3.16x10^{5}$	$4.50x10^{-6}$
C11	$-9.10x10^{3}$	$3.72x10^{5}$	$8.89x10^{-10}$	$9.63x10^{5}$	$1.65x10^{-8}$	$6.78x10^{5}$	$3.73x10^{-7}$
C12	$-5.50x10^{3}$	$3.28x10^{4}$	$2.42x10^{-9}$	$1.09x10^{6}$	$1.84x10^{-8}$	$5.71x10^{5}$	$9.45x10^{-6}$
C21	$-5.44x10^{3}$	$2.79x10^{4}$	$2.31x10^{-9}$	$1.04x10^{6}$	$1.71x10^{-8}$	$2.56x10^{6}$	$7.53x10^{-6}$
C22	$-9.97x10^{3}$	$4.56x10^{5}$	$4.13x10^{-10}$	$1.37x10^{6}$	$1.05x10^{-8}$	$7.12x10^{5}$	$3.17x10^{-7}$
C111	$-5.03x10^{3}$	$8.81x10^{3}$	$3.27x10^{-10}$	$8.31x10^{5}$	$4.52x10^{-8}$	$3.07x10^{4}$	$8.85x10^{-9}$
C112	$-2.96x10^{3}$	$3.34x10^{3}$	$7.10x10^{-9}$	$3.57x10^{5}$	$4.87x10^{-8}$	$3.01x10^{4}$	$1.18x10^{-6}$
C121	$-5.68x10^{3}$	$8.94x10^{3}$	$1.53x10^{-9}$	$6.61x10^{5}$	$4.19x10^{-8}$	$4.48x10^{3}$	$7.23x10^{-9}$
C122	$-3.44x10^{3}$	$1.67x10^{4}$	$2.35x10^{-9}$	$9.39x10^{5}$	$3.47x10^{-8}$	$6.52x10^{4}$	$2.83x10^{-8}$
C211	$-5.08x10^{3}$	$1.27x10^{4}$	$1.42x10^{-8}$	$5.32x10^{5}$	$3.45x10^{-8}$	$1.34x10^{4}$	$9.01x10^{-7}$
C212	$-2.88x10^{3}$	$6.26x10^{3}$	$4.62x10^{-10}$	$7.33x10^{5}$	$3.69x10^{-8}$	$1.16x10^{4}$	$5.85x10^{-9}$
C221	$-4.17x10^{3}$	$1.70x10^{5}$	$5.33x10^{-8}$	$6.61x10^{5}$	$4.28x10^{-8}$	$2.06x10^{4}$	$2.41x10^{-9}$
C222	$-9.32x10^{3}$	$6.13x10^{4}$	$2.86x10^{-10}$	$1.72x10^{6}$	$2.73x10^{-8}$	$1.13x10^{5}$	$4.98x10^{-9}$

Table 3.5: Average and Standard Deviation Values Across All Stages in Sample Sectioning for Rod 20C

20C	R_L	R1	C1	R2	C2	R3	C3
full	$-4.31x10^{3}$	$4.54x10^{6}$	$1.46x10^{-11}$	$4.16x10^{6}$	$1.14x10^{-10}$	$4.90x10^{6}$	$5.60x10^{-9}$
Average Halves	$-3.57x10^{4}$ $\pm 1.52x10^{3}$	$2.93x10^{5}$ $\pm 1.09x10^{4}$	$2.16x10^{-9}$ $\pm 1.49x10^{-9}$	$3.34x10^{6}$ $\pm 4.07x10^{5}$	$1.01\ x10^{-8}$ $\pm 7.99\ x10^{-10}$	$4.78x10^{5}$ $\pm 1.62x10^{5}$	$3.38x10^{-6}$ $\pm 1.11x10^{-6}$
Average Fourths	$-7.50x10^{3}$ $\pm 2.05x10^{3}$	$2.22x10^{5}$ $\pm 1.94x10^{5}$	$1.51x10^{-9}$ $\pm 8.73x10^{-10}$	$1.12x10^{6}$ $\pm 1.55x10^{5}$	$1.56\ x10^{-8}$ $\pm 3.02\ x10^{-9}$	$1.13x10^{6}$ $\pm 8.28x10^{5}$	$4.42x10^{-6}$ $\pm 4.13x10^{-6}$
Average Eighths	$-4.82x10^{3}$ $\pm 1.96\ x10^{3}$	$3.60x10^{4}$ $\pm 5.72x10^{4}$	$9.94x10^{-9}$ $\pm 1.82x10^{-8}$	$8.04x10^{5}$ $\pm 4.09x10^{5}$	$3.9x10^{-8}$ $\pm 6.91x10^{-9}$	$3.62x10^{4}$ $\pm 3.63x10^{4}$	$2.67x10^{-7}$ $\pm 4.82x10^{-7}$

Similarly to Figure 3.6, Figure 3.11 shows the normalized data for both the imaginary impedance and the imaginary modulus, but instead of comparing different full length rod behavior, the figures presented here are for the eighth sized slices of the 20C rod exclusively.

Once again, the imaginary modulus behavior follows near identical behavior in both shape and frequency ranges throughout all of the slices. On the other hand, the imaginary impedance shows some variance in the behavioral types, including examples like C111 and C121, which exhibit a second minor peak around 10^{-1} Hz with C112 also acting similarly although having a slightly larger peak. The rest of the samples including C122, C211, C212, C221, and C222 have their minor peak at a lower frequency that is cut off by the 10^{-2} Hz limit of the measured scan. One major difference between the response of the eighth rods and the full length rods is that in the eighth rods, the location of the modulus peaks have shifted to higher frequency (~$5x10^{6}$ Hz) and there is essentially no overlap between the imaginary modulus and imaginary impedance in this case. The values of the maximum and the peak frequency and components are shown in Table 3.6. These results prove that the impedance measurements are sensitive to different amounts of whiskers being distributed along the measurement direction.

Table 3.6: Maximum and Peak Frequency Values for 20C Eighths Comparison

20C Eighths	Max Z'' (Ohms)	Z''_p Freq (Hz)	Max M'' (m/F)	M''_p Freq (Hz)
C111	$-1.64x10^{5}$	$1.71x10^{2}$	$5.10x10^{-1}$	$1.85x10^{6}$
C112	$-7.30x10^{4}$	$5.84x10^{2}$	$4.23x10^{-1}$	$2.71x10^{6}$
C121	$-1.35x10^{5}$	$2.51x10^{2}$	$4.79x10^{-1}$	$2.15x10^{6}$
C122	$-2.15x10^{5}$	$1.08x10^{2}$	$4.87x10^{-1}$	$2.15x10^{6}$
C211	$-1.13x10^{5}$	$3.16x10^{2}$	$4.63x10^{-1}$	$2.51x10^{6}$
C212	$-1.52x10^{5}$	$2.33x10^{2}$	$4.90x10^{-1}$	$2.15x10^{6}$
C221	$-1.73x10^{5}$	$1.85x10^{2}$	$4.88x10^{-1}$	$2.00x10^{6}$
C222	$-3.83x10^{5}$	$5.84x10^{1}$	$5.53x10^{-1}$	$1.47x10^{6}$

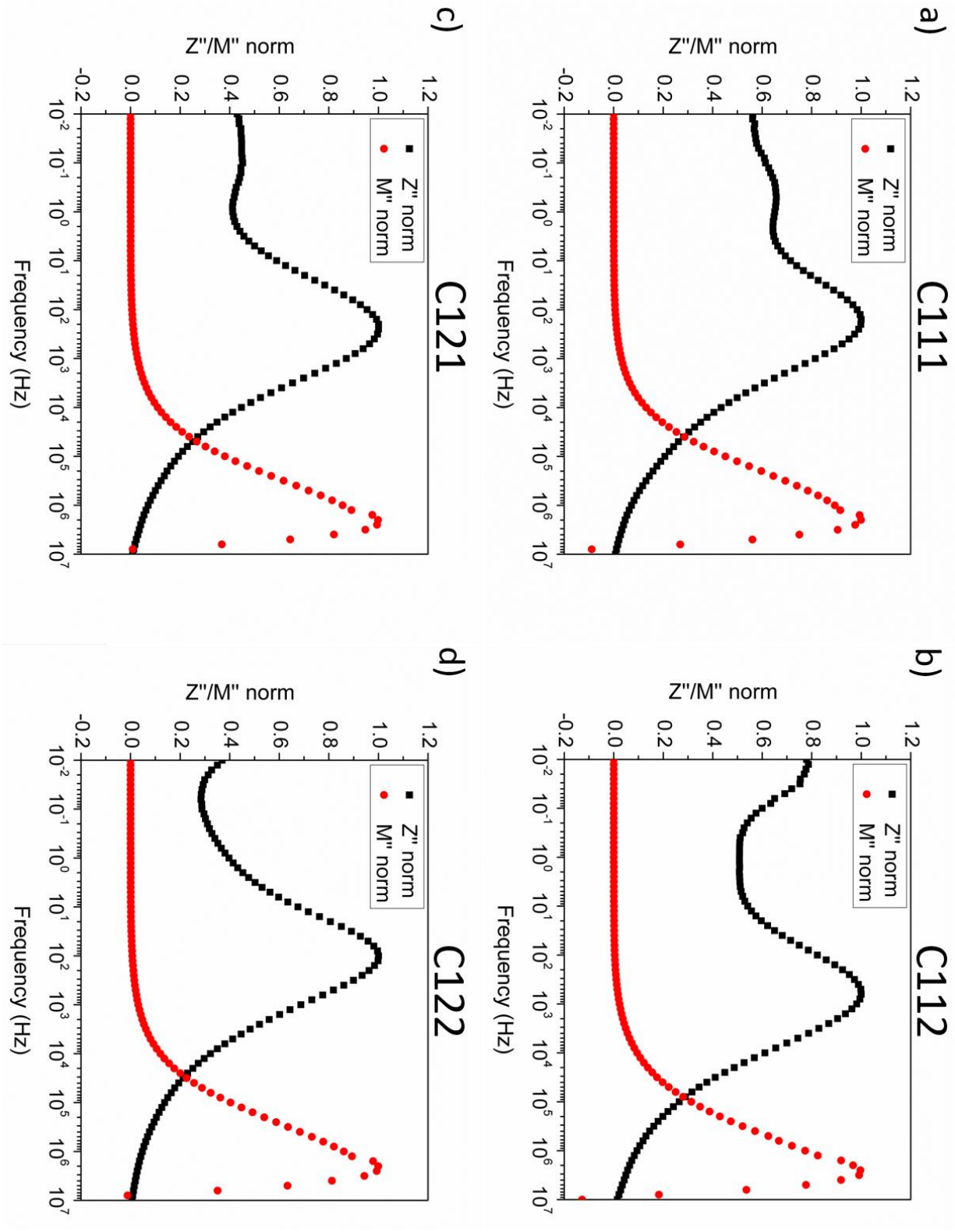

Figure 3.11.1: Normalized Z'' and M'' vs. Frequency for first half of rod 20C's eighth sized samples

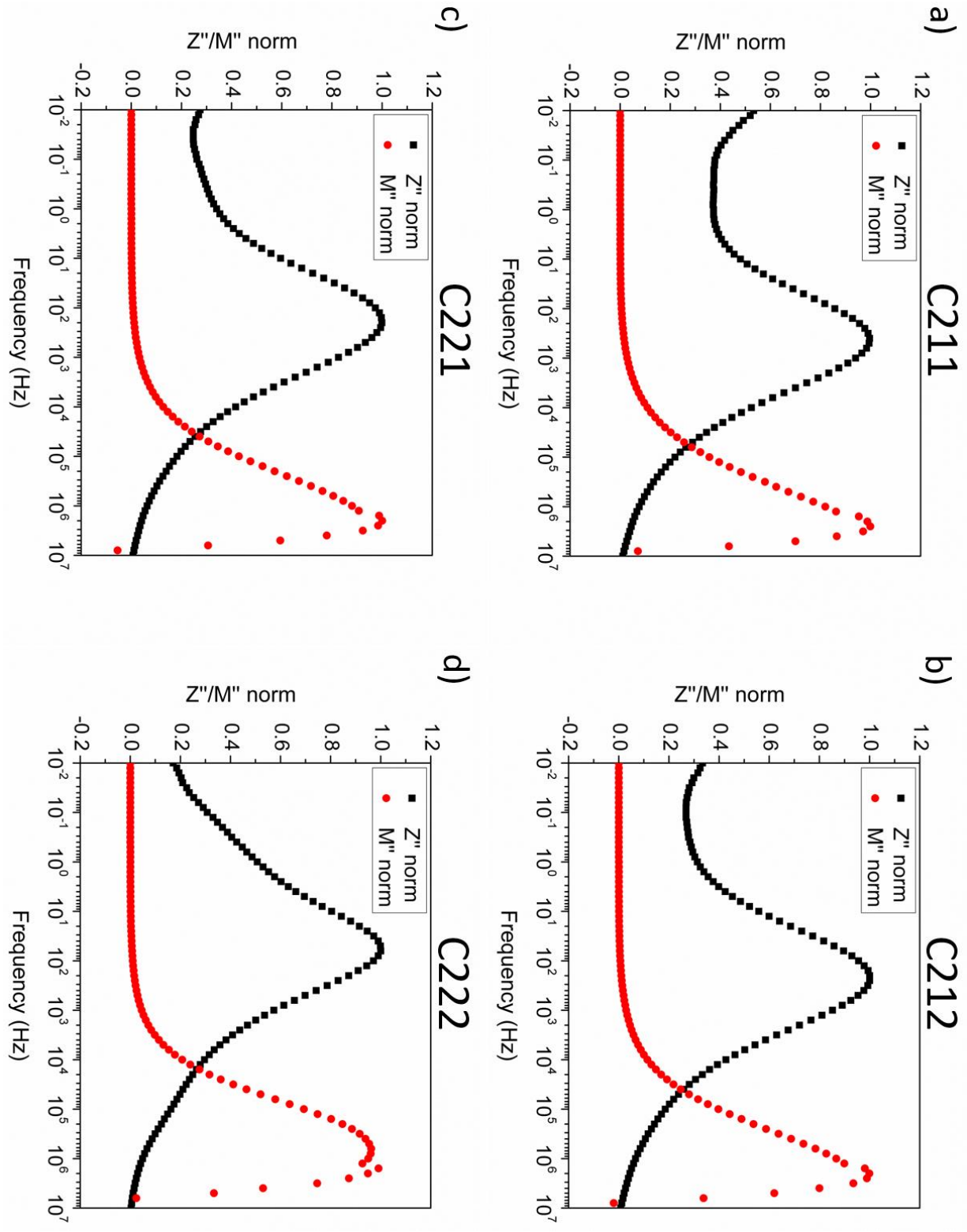

Figure 3.11.2: Normalized Z'' and M'' vs. Frequency for second half of rod 20C's eighth sized samples

3.3 Anisotropy of Rod Microstructure

3.3.1 SEM Confirmation of Anisotropic Microstructure in the Extruded SiC_w-Al_2O_3 Composites

Scanning electron microscope imaging confirms the anisotropy within the extruded rods thought to be present, as explained in the experimental details section. Figures 3.12 offers a gradually increasing magnification of the surface microstructure in order to obtain a broad view of the surface before focusing more on the individual whisker orientations.

The difference in whisker orientation is clear between the two sample orientations. In the parallel direction shown on the left side images in Figure 3.12, the whiskers are seen as circles or hexagons because they are oriented in the z-direction relative to the screen. While some exceptions do exist, the overwhelming majority of whiskers show this clean cut orientation during picture taking. The same overall message can be derived from the perpendicular samples, where the whiskers are overwhelmingly situated in the xy plane. Often the cross-section of the entire length of the whisker can be seen. This can be easily surmised from the images shown on the right in Figure 3.12.

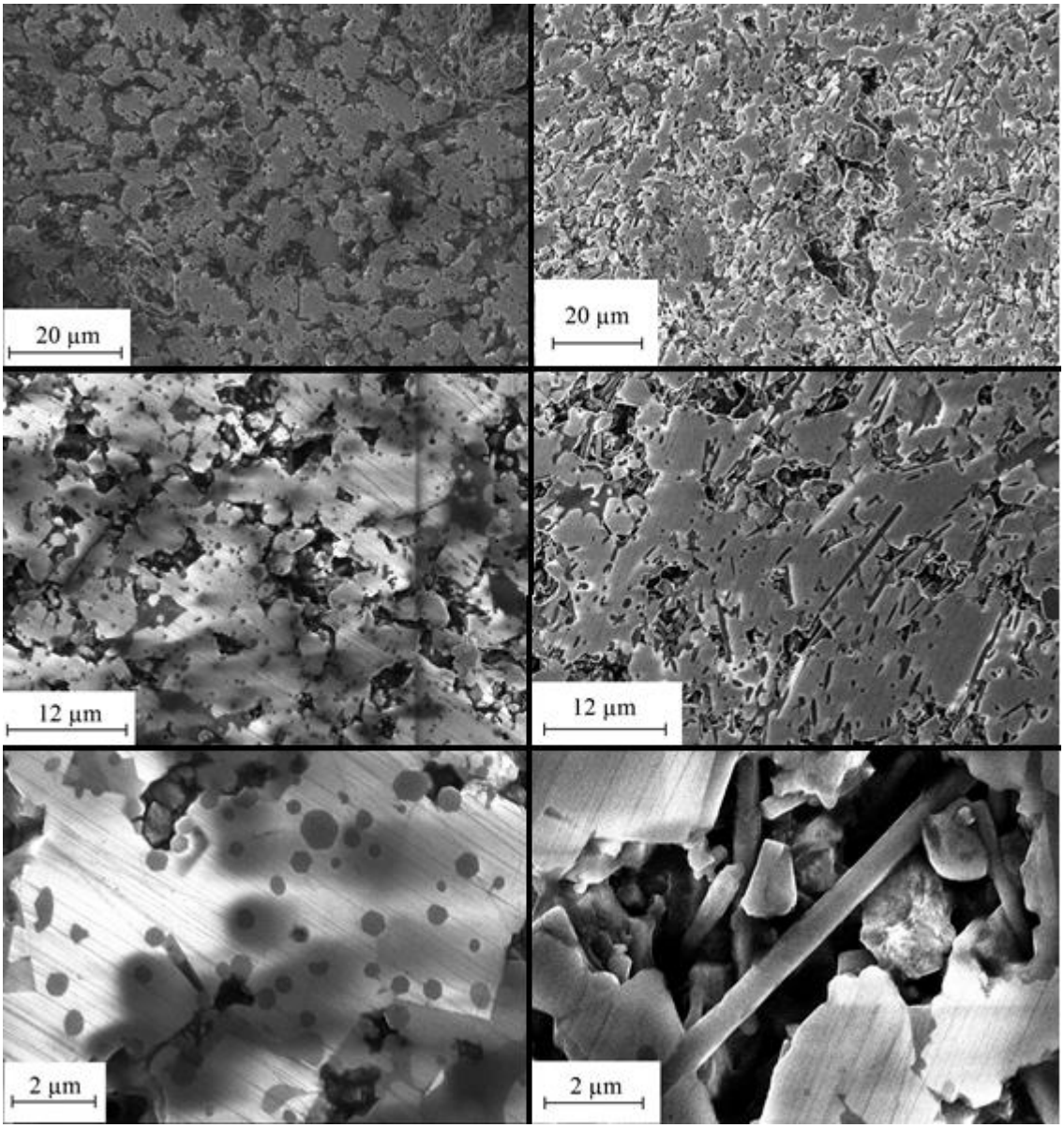

Figure 3.12: Side by side comparisons of whisker views between the parallel to extrusion direction (left) and perpendicular to extrusion direction (right) at three different magnifications

Whisker pullouts are visible in images taken from both sample orientations as this occurs as a result of the grinding/polishing process. Due to the nature of the samples created through extrusion, the porosity is significantly higher in these pressureless sintered samples [16] than when the same compositions are hot pressed or spark plasma sintered as will be described in Chapter 4. The addition of mechanical pressure during sintering promotes plastic flow enhanced

sintering. Furthermore, whisker content and porosity seem to be directly proportional as porosity steadily rises as more whiskers are added to the extruded rods as seen in Figure 3.13 [16]. It seems as though the increased whisker content enables clustering of the whiskers which in turn inhibit densification during sintering [47]. It can be observed that this inhibition caused by whisker clustering happens both before and after the percolation threshold, but the increased whisker content post percolation does cause an increase in the porosity as shown in Figure 3.13 [16].

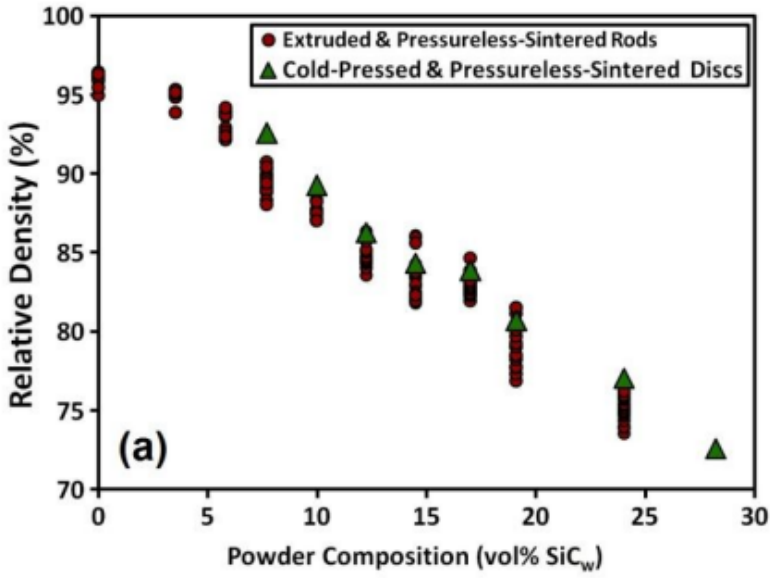

Figure 3.13: Relative density of extruded rods compared to theoretical density against whisker volume concentration for pressureless sintered extruded rods and discs [16]

Additionally, normalized impedance data allows further analysis on the differences sample orientation within the extruded whisker paradigm brings about. Four eighth sized samples were measured in both parallel and perpendicular directions as described in Figure 2.4 in Chapter 2, and normalized to resistivity, as shown in Figure 3.14. The perpendicular measurements are consistently more conducting compared to the parallel counterparts. This is

partly brought about by the sample geometry, where the through thickness of parallel direction is much thicker than for the perpendicular cut samples as mentioned in chapter 2. Thus the current has a much more difficult time traversing an increased amount of material.

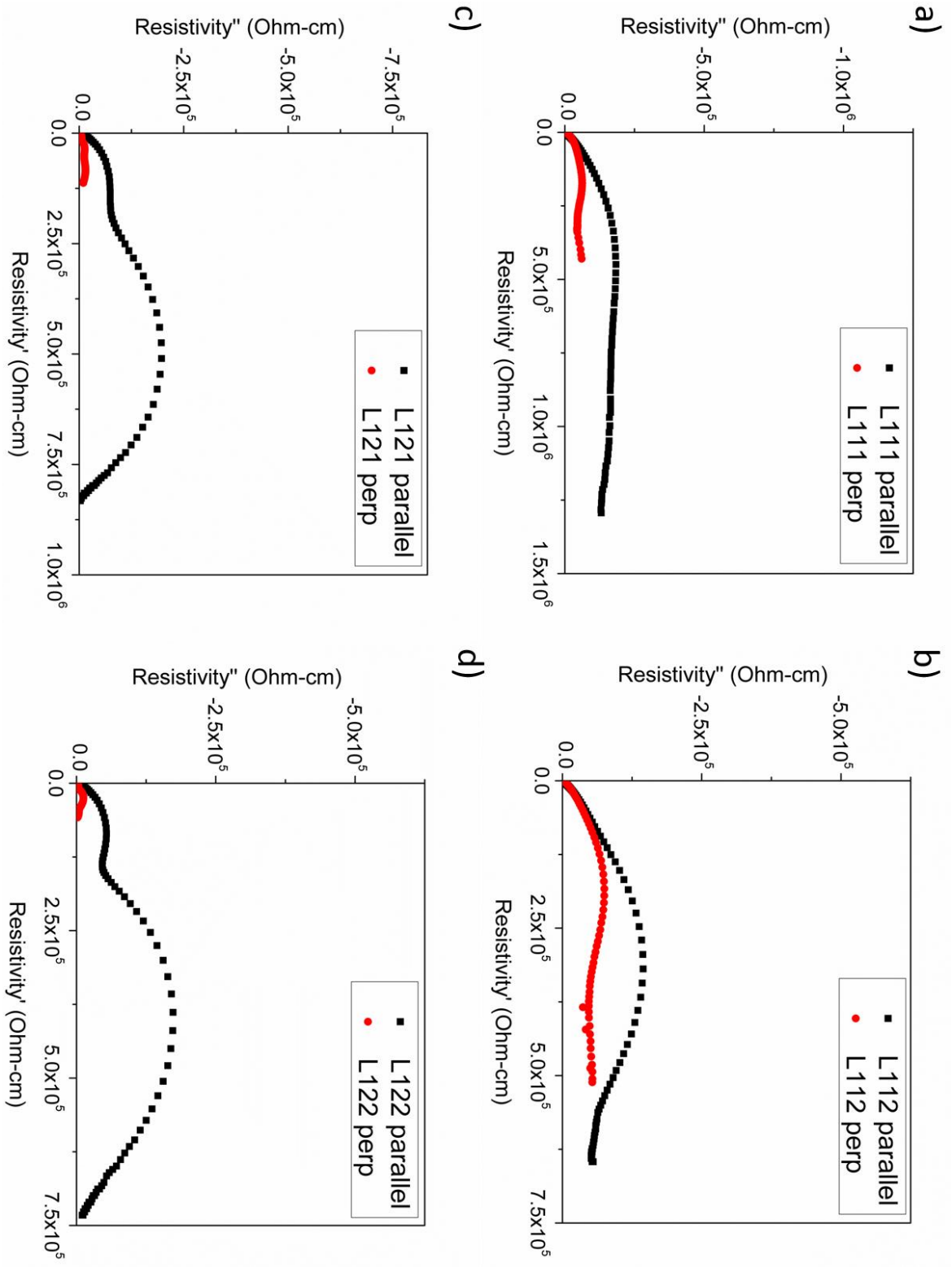

Figure 3.14: Anisotropy comparison of the impedance response normalized by geometric dimensions for measurements parallel and perpendicular to the extruded direction for the 20L samples L111, L112, L121, and L122 eighth samples

3.3.2 Impedance Measurements for Different Sample Orientations With and Without Bias

In addition to looking at the microstructure across different sample orientations and the initial impedance comparison for the parallel and perpendicular measurements, additional impedance measurements were conducted in order to evaluate the effect of the electrodes which could not be easily obtained with longer rods. Figure 3.15 shows the schematics of the orientation of the samples as they were measured as well as the impedance data itself. The samples were cut as explained in the experimental details section to allow scans in both orientations from the same exact specimen for the sake of this comparison noting that the data presented in Figure 3.14 was obtained from circular area eighth cut rods in the parallel direction. When observing the size of the electrodes in the schematics, the size discrepancy becomes apparent and its effect can be seen in the impedance data as well. Considering the rough average sample dimensions of 3.1cm x 0.5 cm x 1.2 cm for these rectangular prisms, the difference in electrode sizes for the parallel and perpendicular measurements become 0.63 cm^2 and 3.93 cm^2 respectively. The ratio between the two electrode sizes is over 6:1. Effects brought about by varying contact sizes and thicknesses has been studied before and was noted how one of the semicircles in the impedance response would coincide once normalized while the other would not [9]. This leads to the association of the second semicircle with the Ag paint electrode [9]. The differing responses as a function of electrode size are also noted in Figure 3.16.

The DC bias serves to minimize the response garnered by the electrode effect in Figure 3.15. Once applied, the bias slowly diminished the impedance response of the low frequency semicircle attributed to the electrode as observed with hot pressed samples before [13]. This behavior is much easier to spot in the perpendicular measurements with the larger electrode and past 10V while the trend continues. There are diminishing effects past this point. In the parallel

specimens, even 40V DC bias is unable to overcome the large Ag paint electrode effect as reported previously [13]. In order to show the effect of changing the Ag paint electrode with a sputter electrode, a thin section was measured with both electrode types. Figure 3.17 shows the much smaller electrode effect on the same extruded rod thin section sample as has been reported before with other SiC_w filled hot pressed samples [13]. However with enough bias both Ag paint and Ag sputter display the same bulk behavior as it should since it is the same specimen.

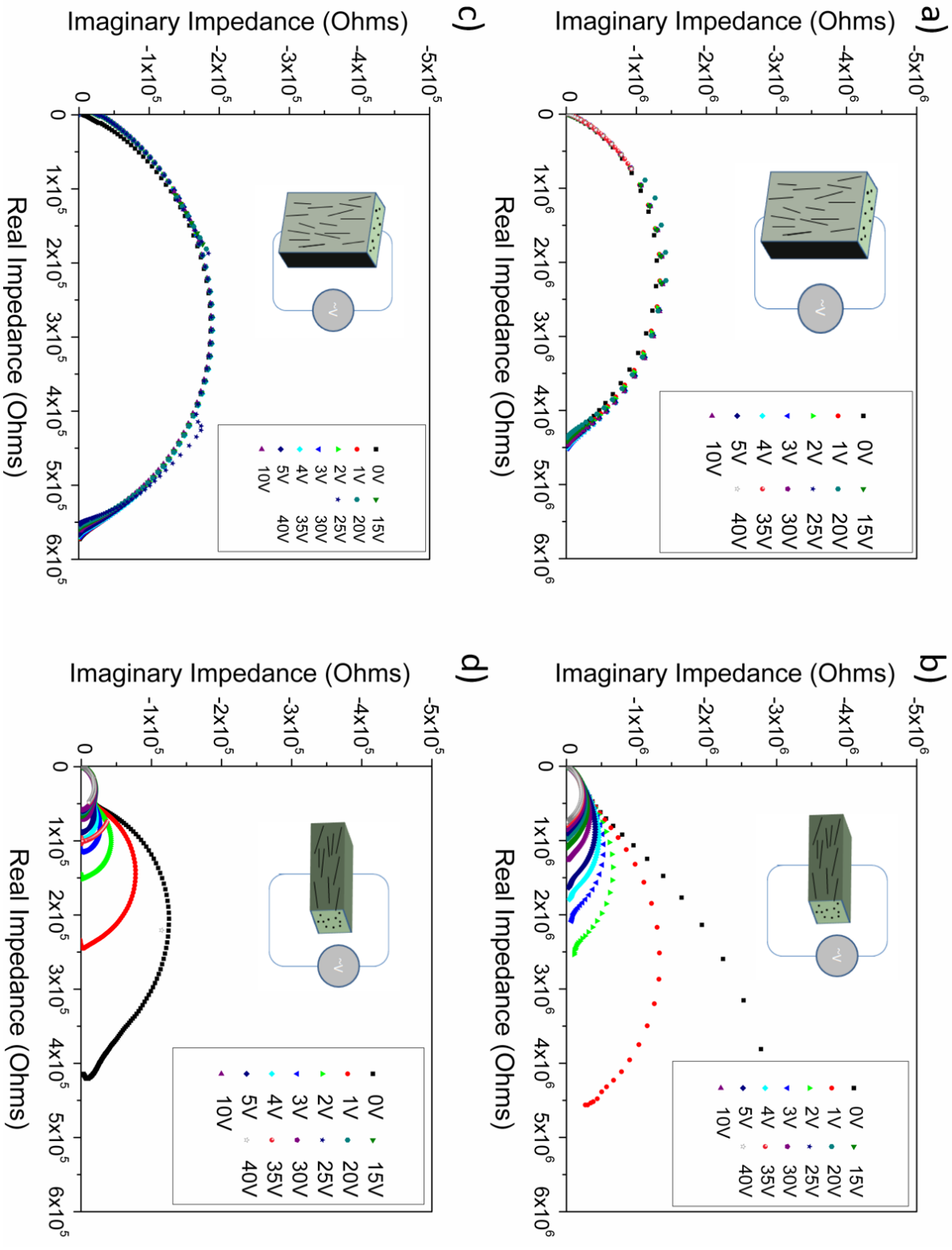

Figure 3.15: DC bias variations from 0 to 40V for the L112 a) parallel, b) perpendicular, L122 c) parallel, and d) perpendicular of the 20L extruded rod using complex impedance plots

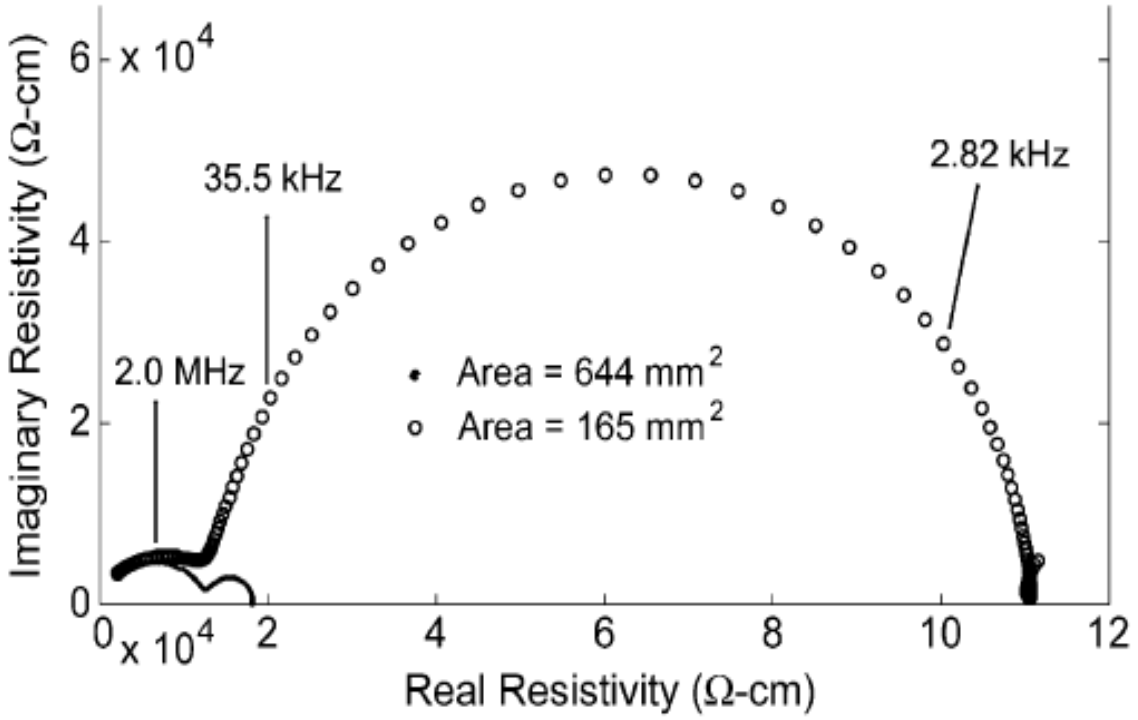

Figure 3.16: Complex normalized resistivity response for two 10% SiC_w samples with different thickness and contact areas [9]

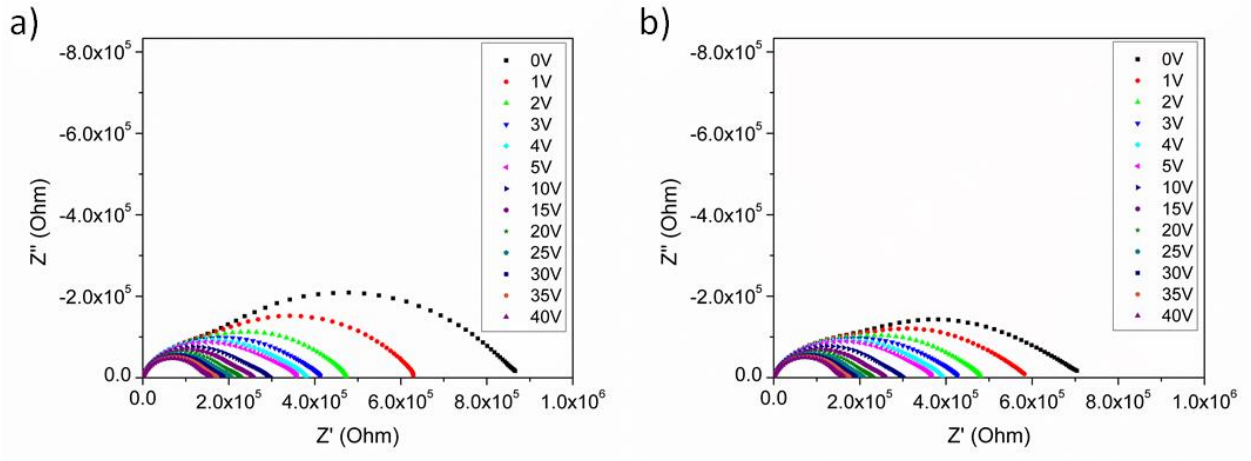

Figure 3.17: a) Ag paint impedance response, b) Ag sputter impedance response both for the same thin slice from an extruded rod

3.4 Measurements on Thin Slices with Sputtered Electrodes

Figure 3.18 lists the complex impedance behavior of a series of thin extruded rod slices post normalization. Although the contact area for the electrodes is completely identical due to the fact that they are sliced from the exact same extruded rod, the thickness of the slices was slightly different due to human error. However, the number of SiC whisker contacts in each of the specimens, even if they were to be cut to the same thickness, may not be the same. Therefore, once normalized, the resistivity of these values could be compared effectively. The thin slices are very consistent in nature, with two of the slices even displaying near identical behaviors. The third slice shows very similar shape, but the last one has much larger semicircle in the low frequency range which can be attributed to less ideal whisker distribution within the slice since we no longer have an electrode effect by using sputtered silver.

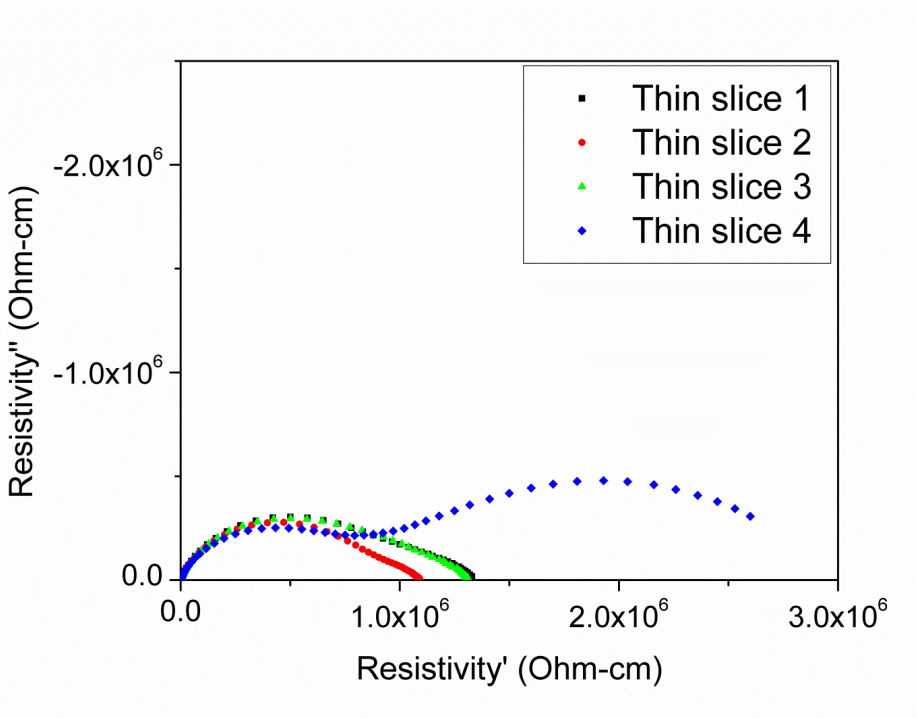

Figure 3.18: Comparison of complex impedance behavior with no bias for the 20C extruded rod thin slices (<2 mm thick)

Figure 3.19 compares the response of the same samples displayed in Figure 3.18, but shows the effect of adding a DC bias in each case. The bias is slowly increased from 0-40V and its effect can be seen in the gradual decrease in resistivity shown. 0-5V measurements were taken in 1V increments to see any fine changes in behavior; however, the change occurs incrementally as expected and nothing out of the ordinary occurs here. Starting at 10V and higher, the bias can be seen affecting the high frequency semicircle as well. This shows that with a strong enough bias, both the matrix and the whiskers and the whisker contact will be affected as was originally proposed by Bertram [14]. This effect is consistent throughout all four slices proving its reproducibility.

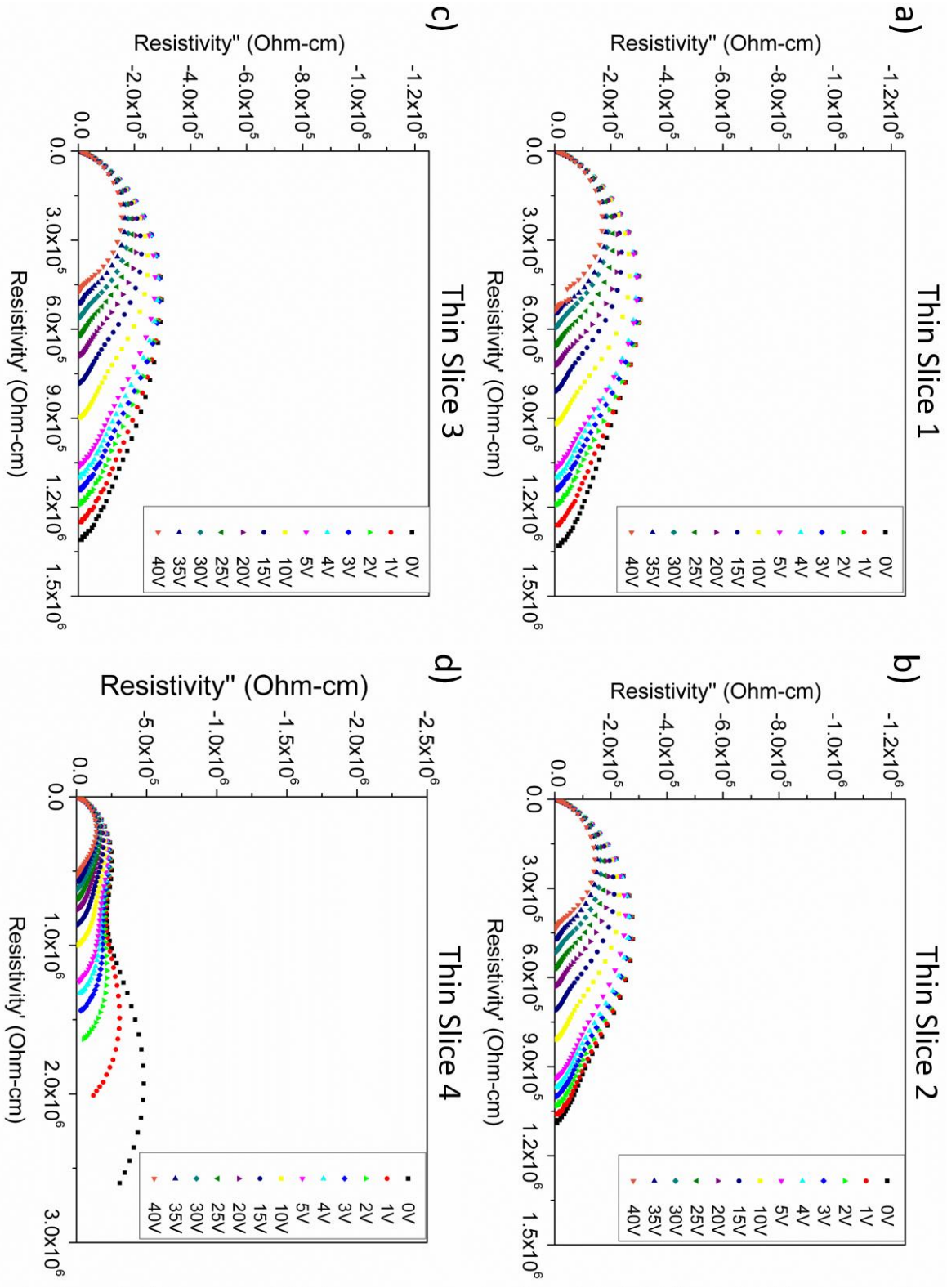

Figure 3.19: Side by side comparison with the addition of 0-40V DC bias for the 20C extruded rod thin slice samples. Please note that part (d) has a different scale.

Figure 3.20 follows the low frequency resistivity versus the increasing DC bias. As previously mentioned, the increasing DC bias serves to eliminate the low frequency semicircles. The gradual decrease in resistivity as the DC bias goes up reaffirms this fact. Another interesting thing to note is the convergence of behaviors across all thin slices. Even the fourth thin slice which displayed higher levels of resistivity at low DC bias converge with the other slices relatively quickly around 10V of bias which is where the electrode Schottky bias effect has been demonstrated with I-AFM images [13]. Figure 3.21 shows the whiskers responding to the bias applied from the tip of the AFM. By preparing an extremely thin parallel slice of the extruded rod, the response gathered with the I-AFM can be compared to SEM images listed previously in Figure 3.12. The size of the current signals accurately represents the dimensions of whiskers provided in Chapter 2.

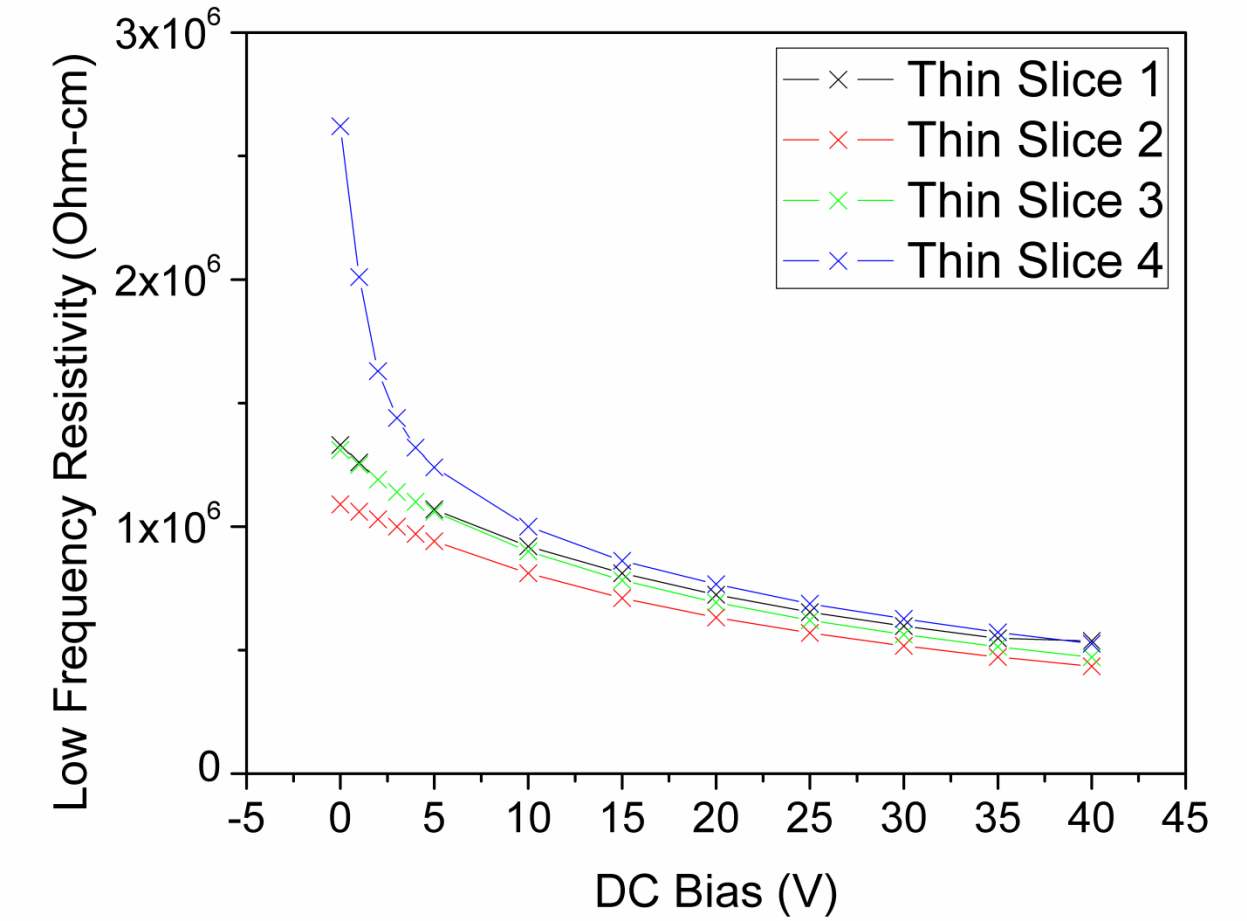

Figure 3.20: Low frequency values at each value of DC bias for all four extruded rod thin slice samples

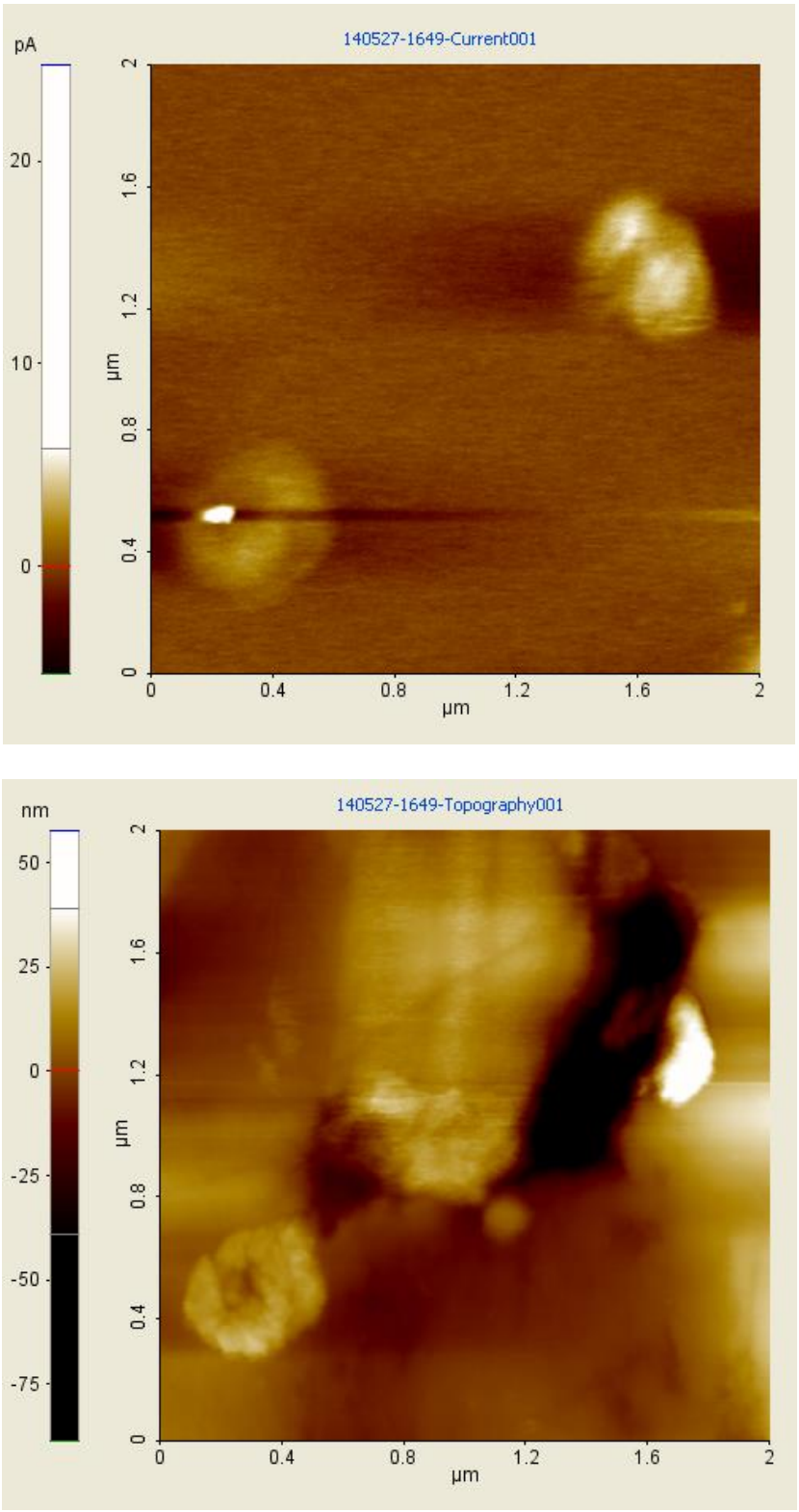

Figure 3.21: I-AFM and topography imaging of an extruded pressureless sintered thin section sample taken with a Pt coated AFM tip at 10V bias shown

Chapter 4

Results on Hot Pressed and Spark Plasma Sintered 15% SiC_w Samples

This chapter will conclude the results section of this thesis. The difference in processing methods between the two sintering techniques employed will be analyzed comparing sample microstructure through microscopy as well as impedance spectroscopy measurements. As outlined in chapter 2, the same 15% SiC_w-Al_2O_3 containing varying amounts of sintering additives will be compared in this chapter.

4.1 Electrode Effect in Hot Pressed and Spark Plasma Sintered Samples

4.1.1 Hot Press Sample Analysis

As described in Chapter 3 and in earlier publications [13,14], when comparing any relatively thin samples such as those fabricated through hotpressing or spark plasma sintering, the electrode always plays a significant role in the impedance measurements [13]. Across all samples, whether it is between different sample processing techniques or different sets within the same method, each has been normalized according to the sample geometry in order to easily compare the impedance responses between them. The initial set of hotpressed samples were fabricated with the powders of compositions A through D. During the second trip, the pure composition E was made and two samples along with a full second set of A through D samples were fabricated. The powder compositions are as listed in Table 2.2.

Figure 4.1a and Figure 4.1b show the discrepancies caused by using the silver paint and silver sputter electrodes on all 5 specimen types. The low frequency electrode semicircle displayed is substantial compared to the bulk behavior in the case of Ag paint. While the most insulating HP D sample exhibits a response around 40,000 Ohm-cm, the electrode effect extends

the response all the way past 100,000 Ohm-cm. This larger response is consistent throughout all five sample blends. Looking at the sputtered electrode response exclusively, it is clear to see that increasing the amount of sintering additives results in a more insulative behavior. In contrast, for the samples measured with Ag sputter shown in Figure 4.1(b), the resistivities are about an order of magnitude lower.

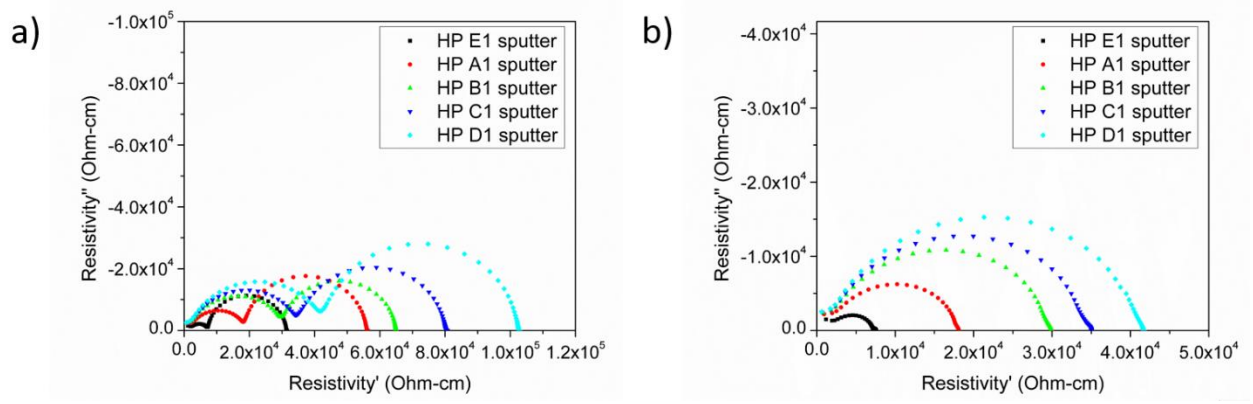

Figure 4.1: a) Comparison across all five powder compositions using the silver paint electrode, b) Comparison across all five powder compositions using the silver sputter electrode for HP samples

Table 4.1 provides a quick overview of the data seen in Figure 4.1 by rearranging it into table form. As visually seen in the figure, the low frequency electrode response is much larger than the bulk response and the two gradually increase in resistivity as the sintering additives increase.

Table 4.1: Bulk and Ag Paint Electrode Response for Hot Pressed Samples

HP	Bulk (Ohm*cm)	Electrode(Ohm*cm)	Additives
E	7,500	24,500	Pure
A	18,000	38,000	0% MgO, 1% Y_2O_3
B	30,000	35,000	0.25% MgO,
C	35,000	45,000	0.5% MgO,
D	42,000	61,000	1% MgO,

Figure 4.2 shows the 100µm cross section of the surface microstructure of all the hotpressed samples. The difference in microstructures across sample compositions with varying sintering additives is not significant at first glance. Whisker orientation within the xy-plane is random with a good distribution in whisker size as well.

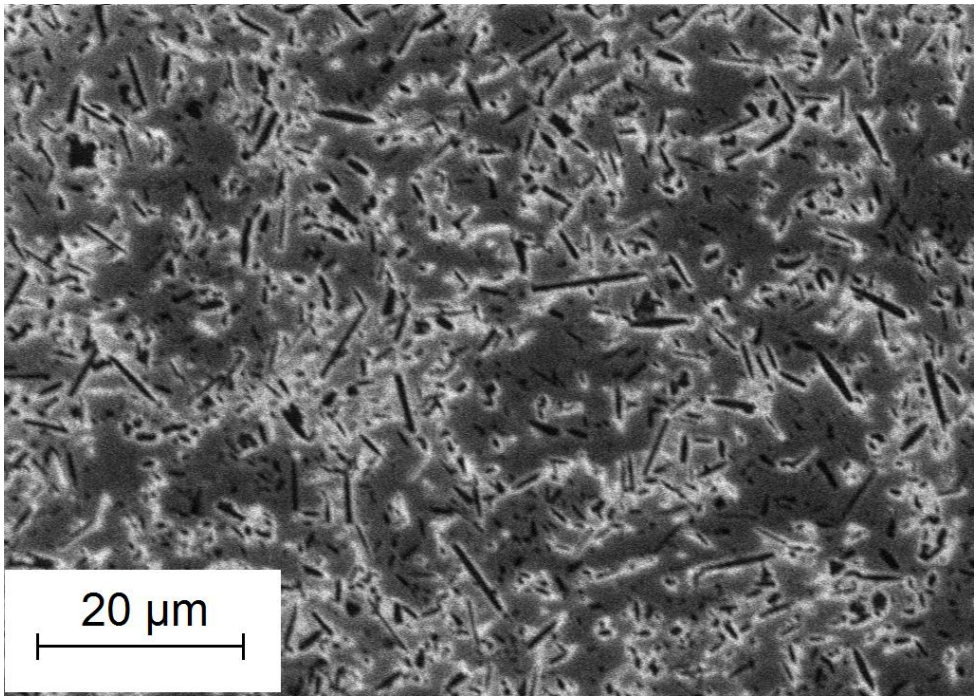

HP E

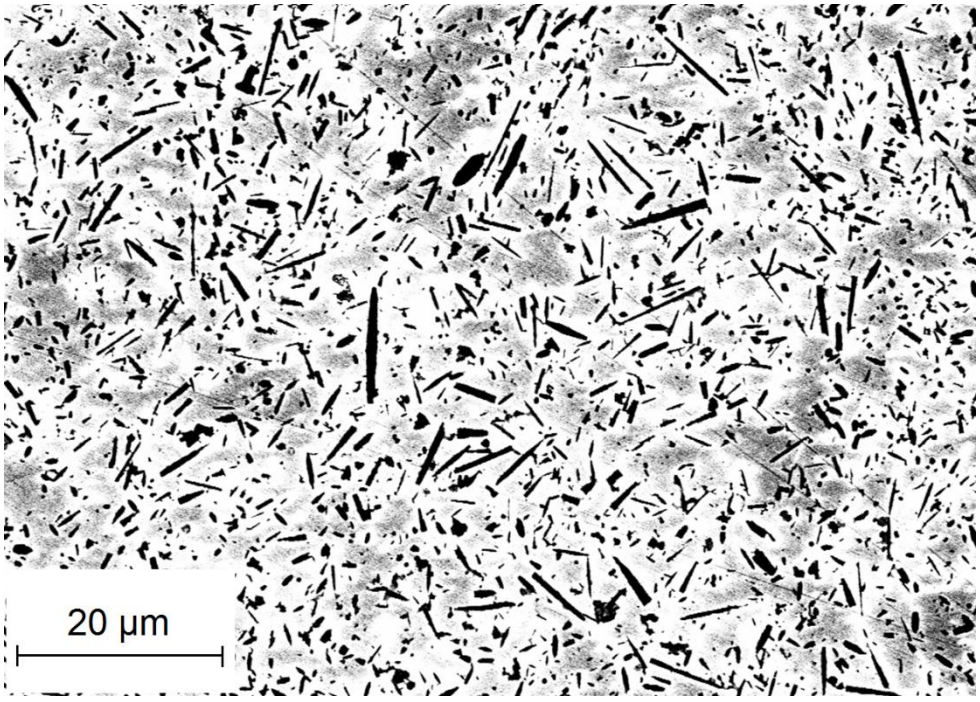

HP A

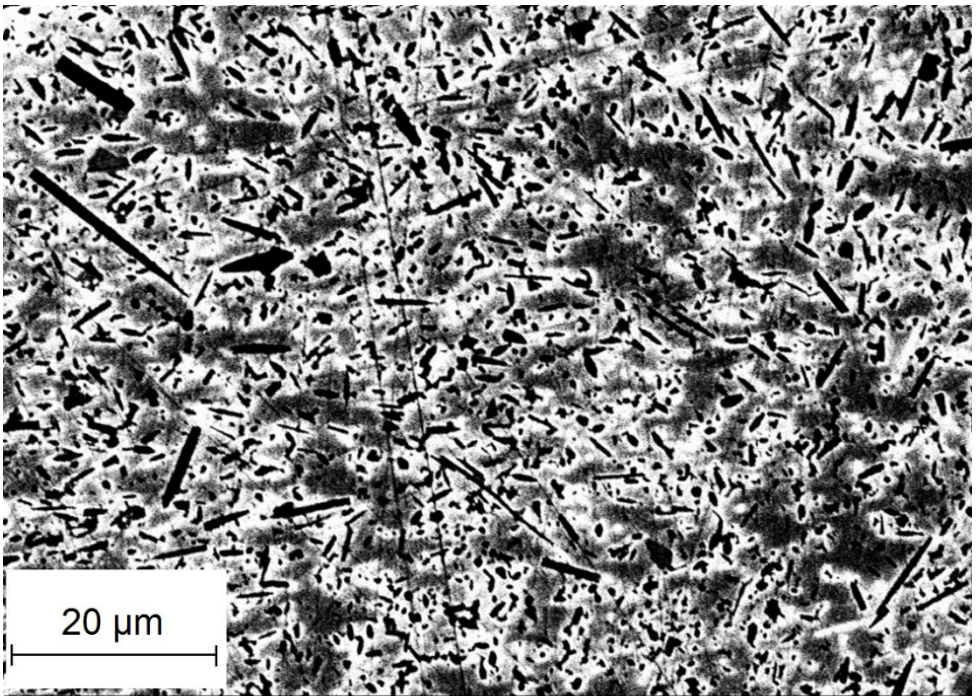

HP B

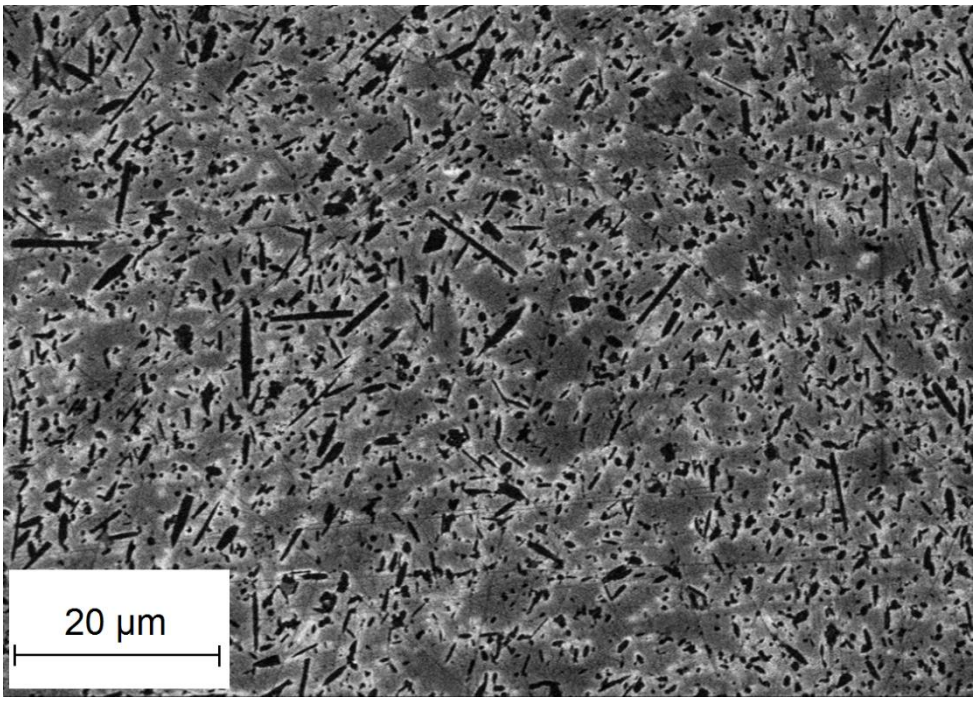

HP C

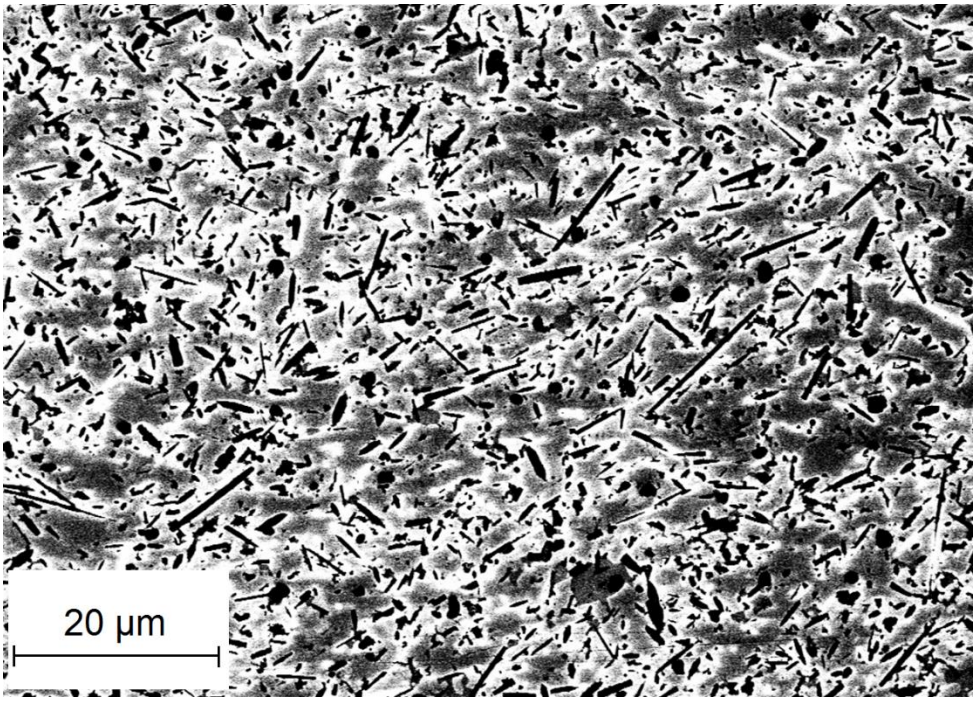

HP D

Figure 4.2: SEM images of all five additive compositions for the 15% SiC_w-Al_2O_3 hotpressed samples

4.1.2 Spark Plasma Sintered Specimens

Similarly to the hotpressed samples mentioned in Figure 4.1, the spark plasma sintered samples measured using Ag paint in Figure 4.3a display a strong effect brought about by the electrode effect. The low frequency semicircle is present for the silver paint electrodes while the sputtered electrodes (shown in Figure 4.3b) showcase the bulk behavior more easily. The magnitude difference between the bulk behavior and the electrode effect for the spark plasma sintered samples is larger than for the hotpressed counterparts. This is another effect of the electrode size effect previously mentioned in Chapter 3 Figure 3.16 [9]. The size of the electrode is a direct result of the size of dies used during the sintering process. The die for the hotpressed samples was roughly 2.92cm in diameter, while the diameter for the spark plasma sintered samples was roughly 2.00 cm as described in Chapter 2. The smaller electrode area of the spark

plasma sintered samples leads to a larger electrode response as has been documented in the literature [9].

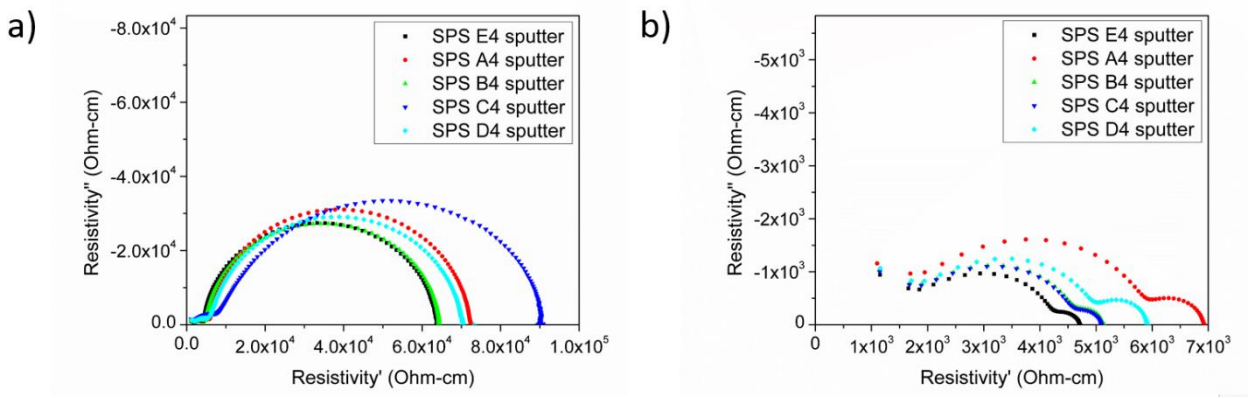

Figure 4.3: a) Comparison of the electrical properties of 15% SiC_w-Al_2O_3 composites for all SPS sintered five additive compositions using the silver paint electrode, b) Comparison across all five additive compositions using the silver sputter electrode for SPS samples

Table 4.2 lists the separated values between the bulk response and electrode response for the spark plasma sintered samples shown in Figure 4.3. The A composition seems to be an outlier to an otherwise slow but steady increase in the resistivity for the bulk behavior. The electrode behavior on the other hand is similar regardless of composition.

Table 4.2: Bulk and Ag Paint Electrode Response for Spark Plasma Sintered Samples

SPS	Bulk (Ohm*cm)	Electrode (Ohm*cm)	Additives
E	4,700	57,300	Pure
A	7,000	65,000	0% MgO, 1% Y_2O_3
B	5,200	56,800	0.25% MgO, 1% Y_2O_3
C	5,200	84,800	0.5% MgO, 1% Y_2O_3
D	5,900	64,100	1% MgO, 1% Y_2O_3

SEM images for the surface microstructure of the SPS samples are presented in Figure 4.4. Each image was taken at 10.0Kx magnification with an accelerating voltage of 15kV. The randomness of the whisker orientations and size distribution are similar to those shown in the SEM images for the HP samples. An interesting effect is observed in the SPS B composition here, where a very fine grain like structure appears within the matrix. It is unlikely that the effects observed are pores because the density of this sample is above 99% and its density is comparable to the other SPS samples.

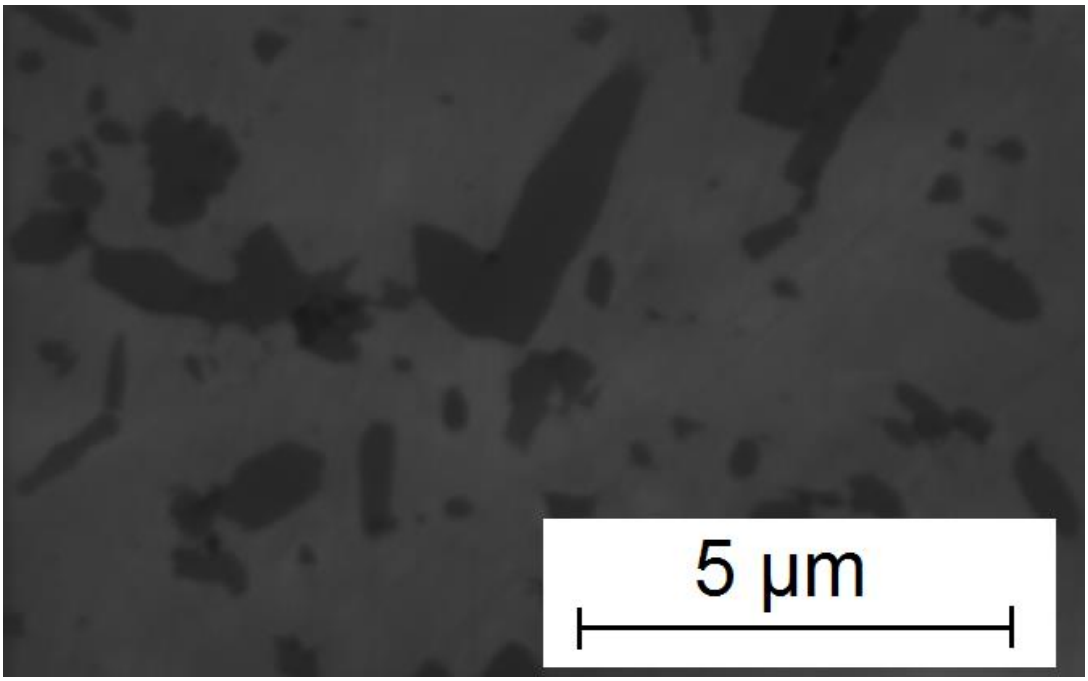

SPS E

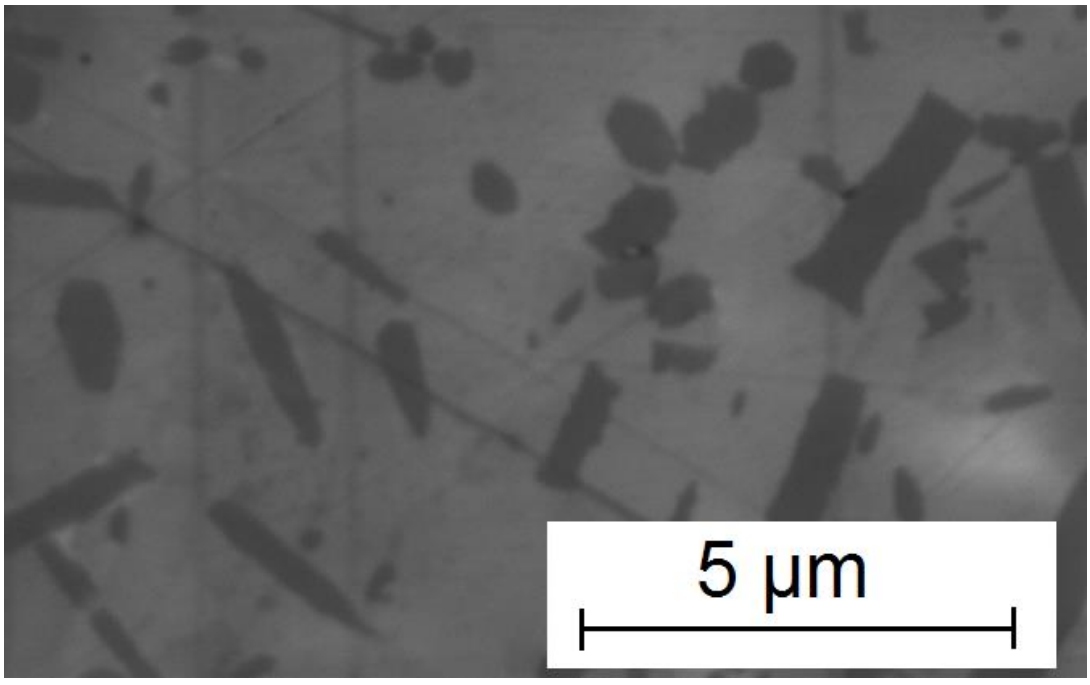

SPS A

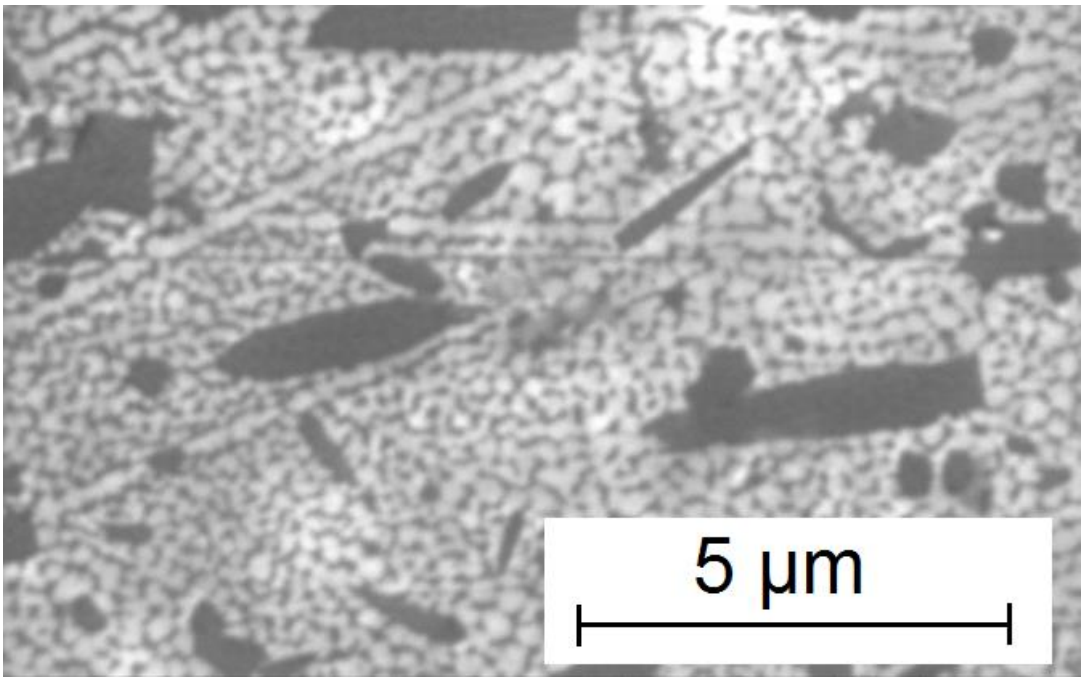

SPS B

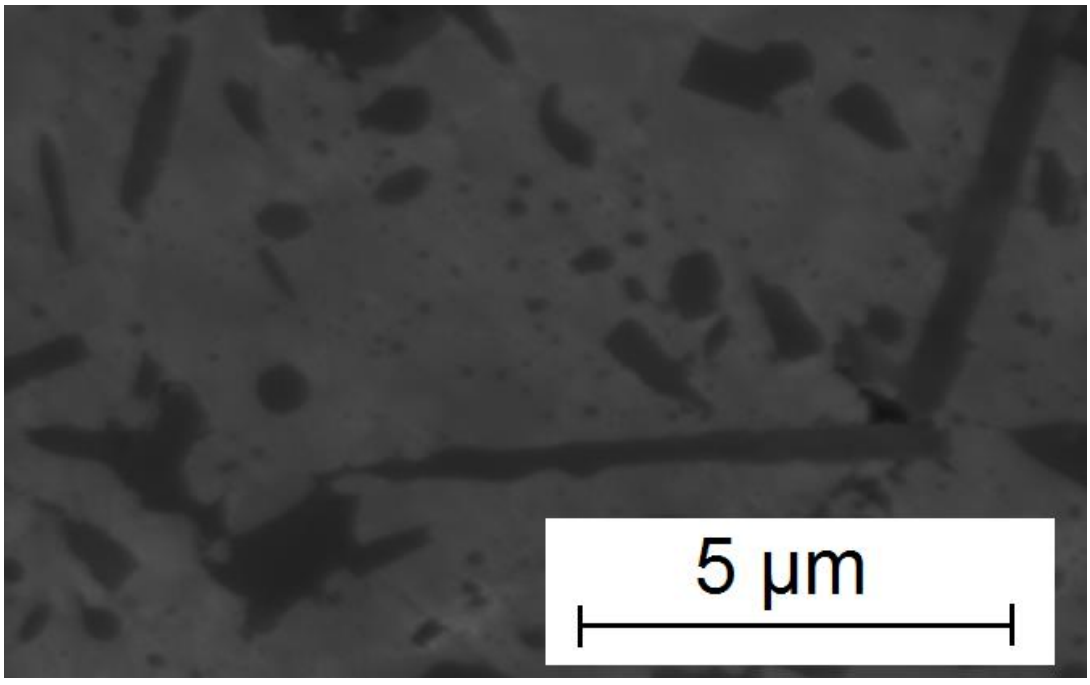

SPS C

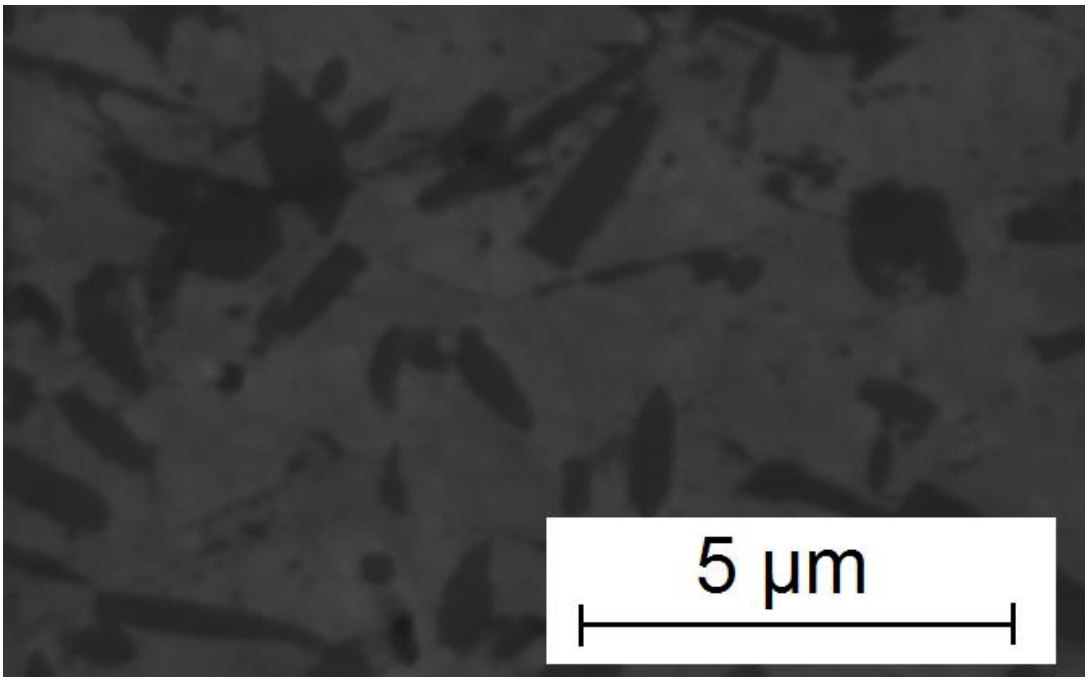

SPS D

Figure 4.4: SEM images of all five compositions for the spark plasma sintered samples

4.1.3 Comparison of Ag Paint and Sputtered Ag Electrodes

Figure 4.5 gives a clearer side by side view of the electrode effect for each sample one by one as they were all measured by using Ag paint, first removing it and then recoating with sputtered Ag. Although this figure does not bring anything new to the table, it adds clarity to the way the electrode effect can affect each sample. In each case, the huge electrode contact semicircle disappears when the same sample is measured using sputtered Ag. The trends brought about by the differing sintering additives are more easily viewed in Figure 4.1 and Figure 4.3. Nevertheless, all samples appear to show two main semicircles. This will be discussed in more detail later.

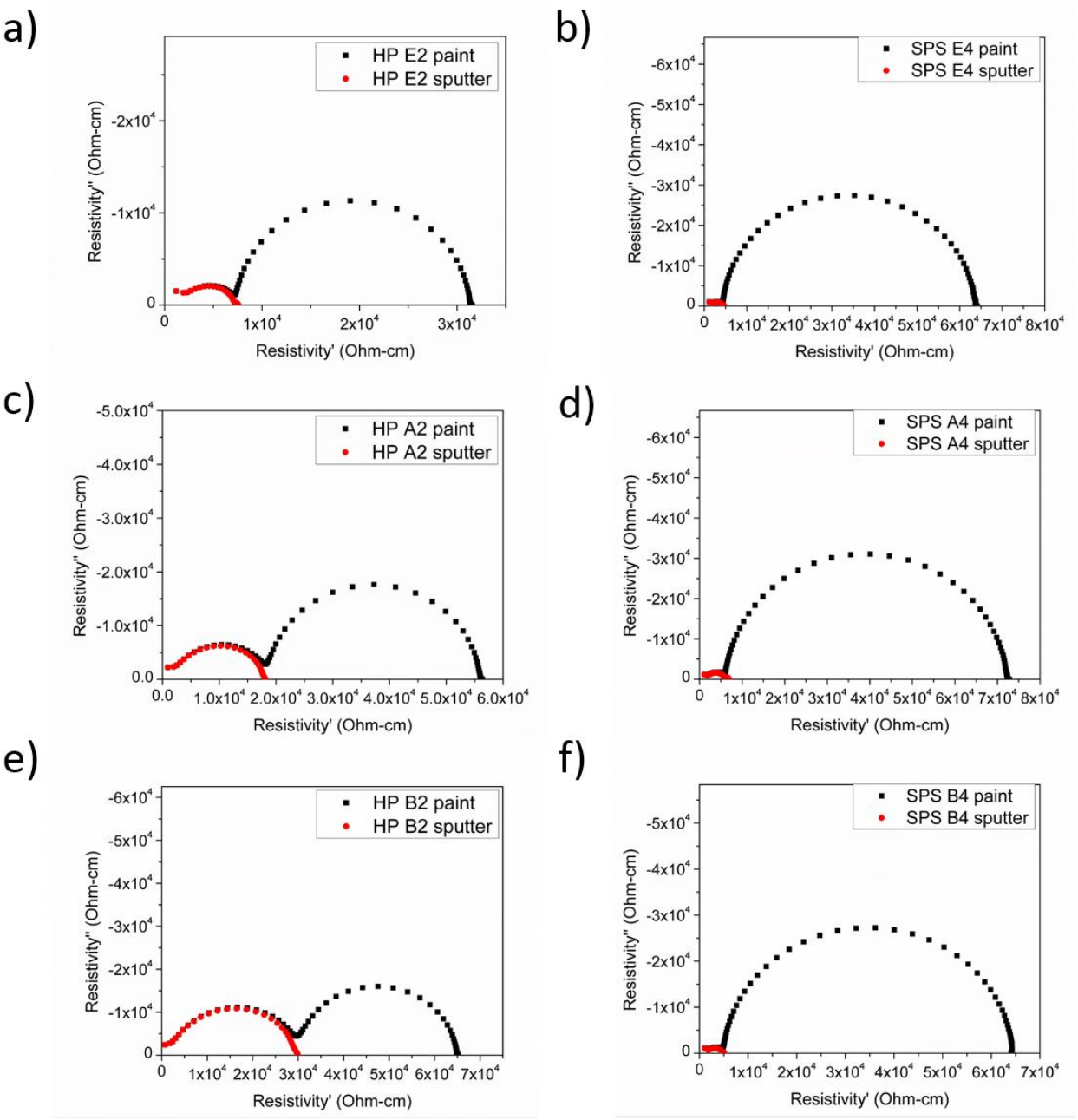
a)
HP E2 paint
HP E2 sputter
Resistivity'' (Ohm-cm)
Resistivity' (Ohm-cm)
b)
SPS E4 paint
SPS E4 sputter
Resistivity'' (Ohm-cm)
Resistivity' (Ohm-cm)
c)
HP A2 paint
HP A2 sputter
Resistivity'' (Ohm-cm)
Resistivity' (Ohm-cm)
d)
SPS A4 paint
SPS A4 sputter
Resistivity'' (Ohm-cm)
Resistivity' (Ohm-cm)
e)
HP B2 paint
HP B2 sputter
Resistivity'' (Ohm-cm)
Resistivity' (Ohm-cm)
f)
SPS B4 paint
SPS B4 sputter
Resistivity'' (Ohm-cm)
Resistivity' (Ohm-cm)

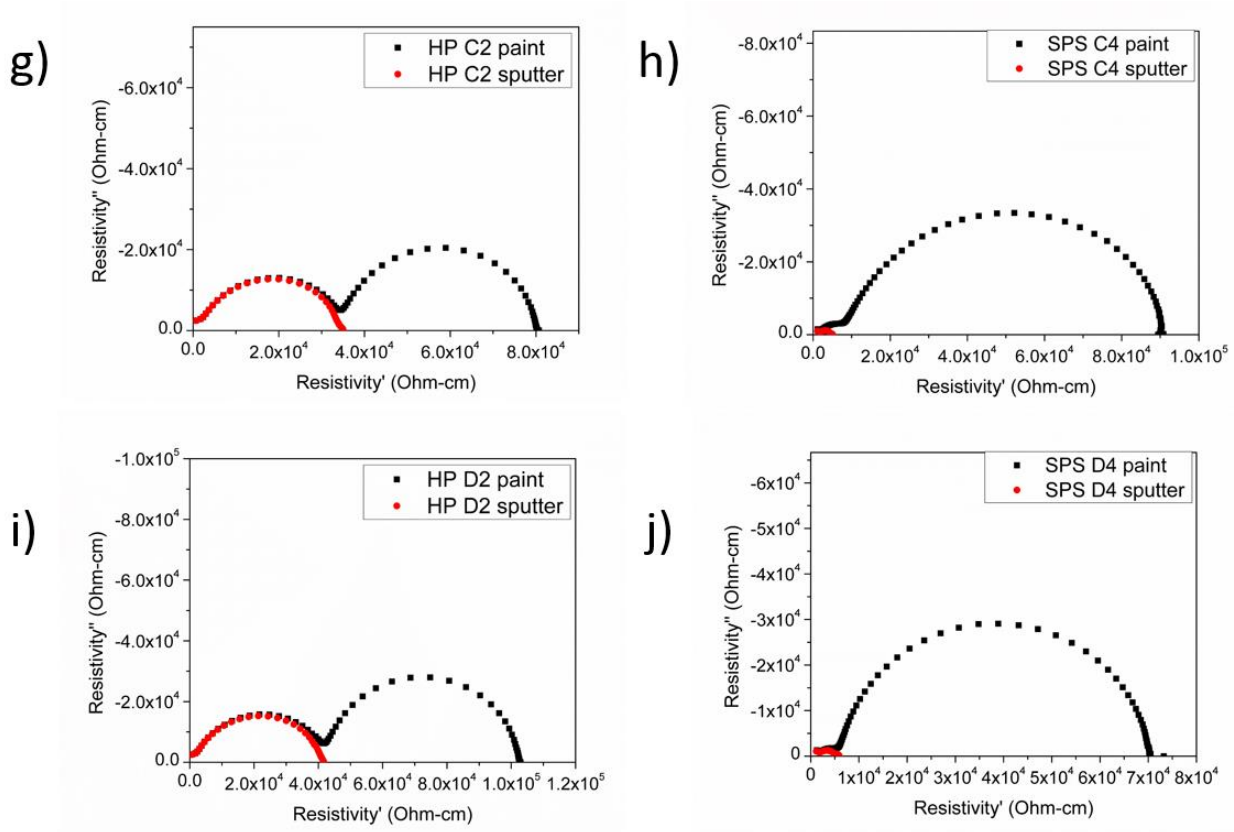

Figure 4.5: Side by side comparison of electrode effect for both HP and SPS samples across all powder compositions

The sintering additives used in the past correspond to the highest composition of this study, i.e. the D composition containing 1% Y_2O_3 and 1% MgO was compared with samples made in the past by Brian Bertram [1] with the same level of sintering additives as well as SiC_w composition in Figure 4.6. Brian's sample was measured again recently, but it is important to note that the shape of the sample was closer to a semicircle due to being cut previously instead of having a circular shape like the recently pressed hotpressed and spark plasma sintered samples. After normalization, it is observed that the newly fabricated samples are roughly twice as conducting compared to the older samples. Since compositional parameters are identical, the changes can be attributed to differences in processing parameters such as the maximum sintering temperature and pressure as well as the size and shape of the specimens.

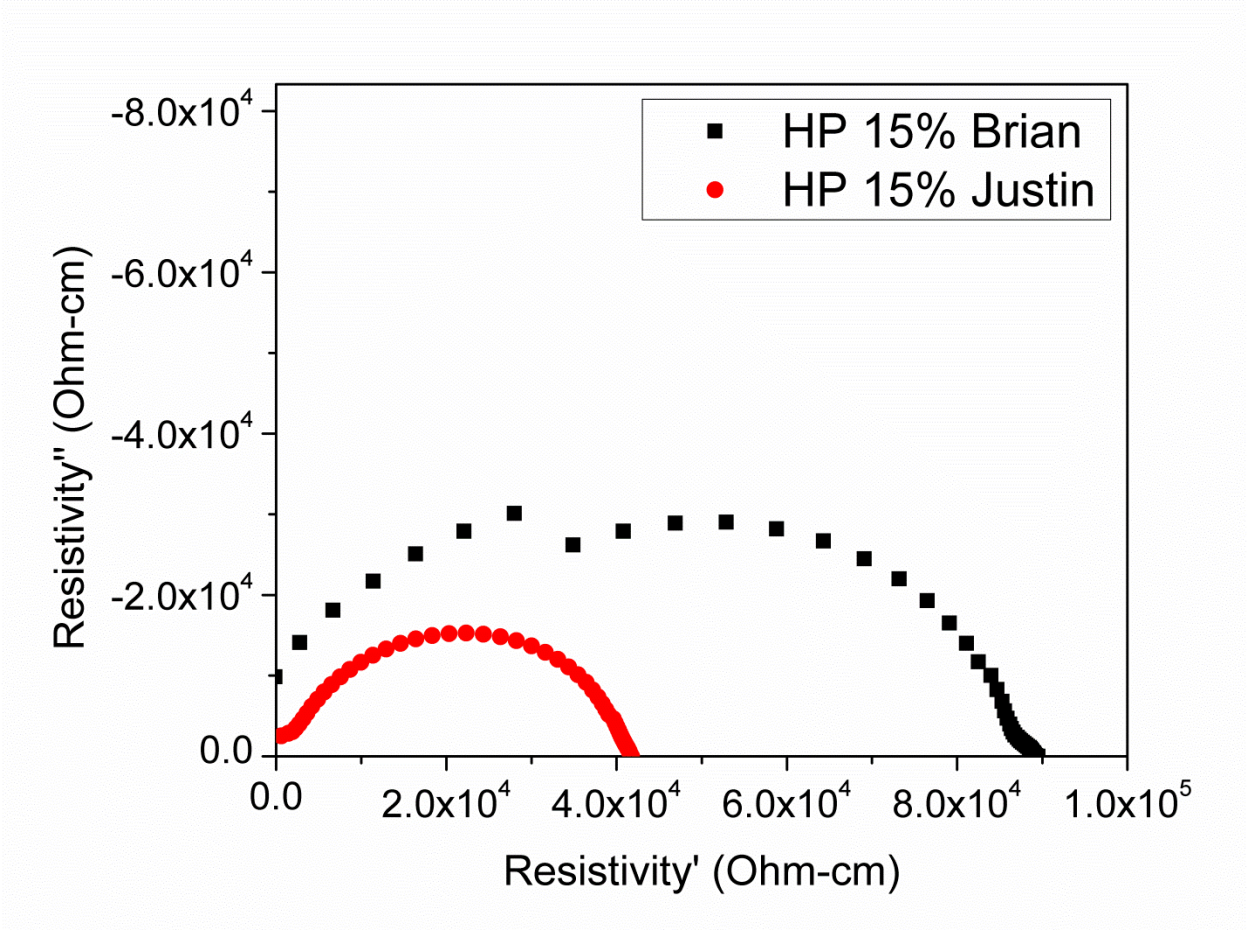

Figure 4.6: Comparison between 15% SiC_w composites made by Brian Bertram and Justin Brandt

4.1.4 Comparison of HP vs SPS with Sputtered Ag

The effects of sample processing brought about by the differences between hotpressing and spark plasma sintering are better shown in Figure 4.7. The data is presented in normalized impedance to account for the sample size difference between the hotpressed and spark plasma sintered samples. Most obviously, the common trend seen throughout these samples is the fact that the spark plasma sintered samples are consistently more conductive in nature (i.e. they show smaller impedance semicircles) compared to the hotpressed samples. The magnitude varies between 2x-10x depending on the composition. The resistivity for the pure samples are closer in

nature, the factor is only a difference of two. As the amount of sintering additives increases, the difference increases as well, ultimately expanding to a difference separated by a factor of ten.

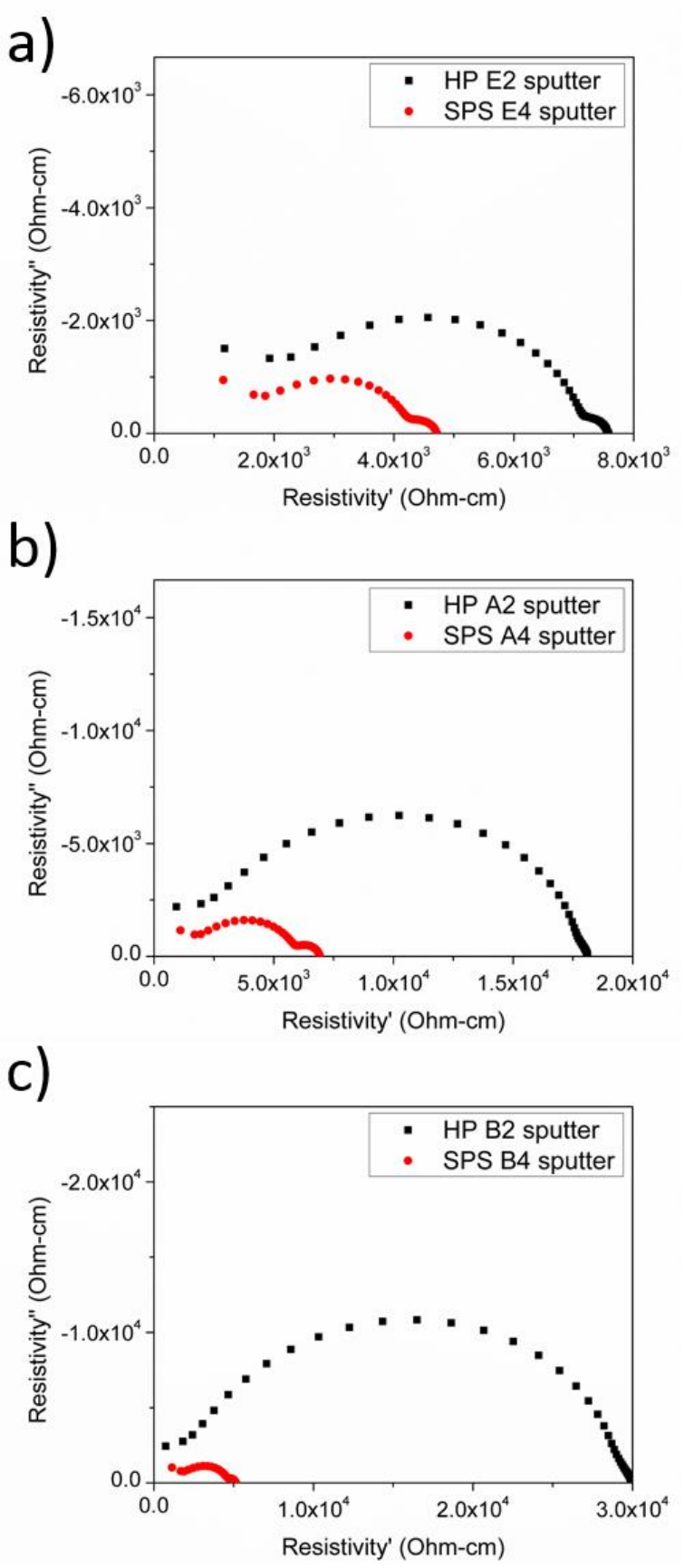
a)
HP E2 sputter
SPS E4 sputter
Resistivity'' (Ohm-cm)
-6.0x10^3
-4.0x10^3
-2.0x10^3
0.0
0.0
2.0x10^3
4.0x10^3
6.0x10^3
8.0x10^3
Resistivity' (Ohm-cm)
b)
HP A2 sputter
SPS A4 sputter
Resistivity'' (Ohm-cm)
-1.5x10^4
-1.0x10^4
-5.0x10^3
0.0
0.0
5.0x10^3
1.0x10^4
1.5x10^4
2.0x10^4
Resistivity' (Ohm-cm)
c)
HP B2 sputter
SPS B4 sputter
Resistivity'' (Ohm-cm)
-2.0x10^4
-1.0x10^4
0.0
0.0
1.0x10^4
2.0x10^4
3.0x10^4
Resistivity' (Ohm-cm)

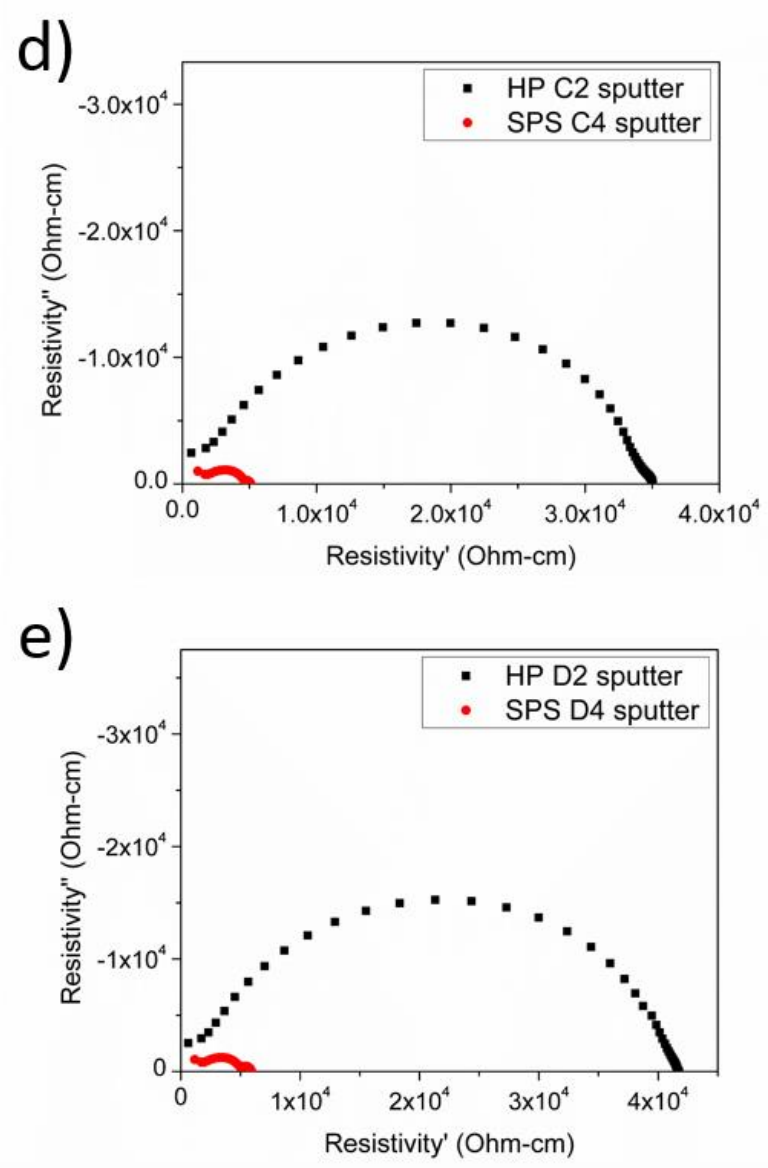

Figure 4.7: Direct comparison between hotpressing and spark plasma sintering for each 15% SiC_w-Al_2O_3 sample containing different amounts of additives

The impedance behavior shown in Figure 4.7 can be explained by the schematic shown in Figure 4.8 depicting possible whisker behavior. Junctions between whiskers may be in direct contact or be slightly separated as previously proposed [9]. The current can be expected to travel much more easily through junctions that interconnect directly, whereas slightly disjointed whiskers may need some help in order for signals to traverse them. Finally, in between

individual whiskers the signals travel most easily and the resistance values there should be the smallest.

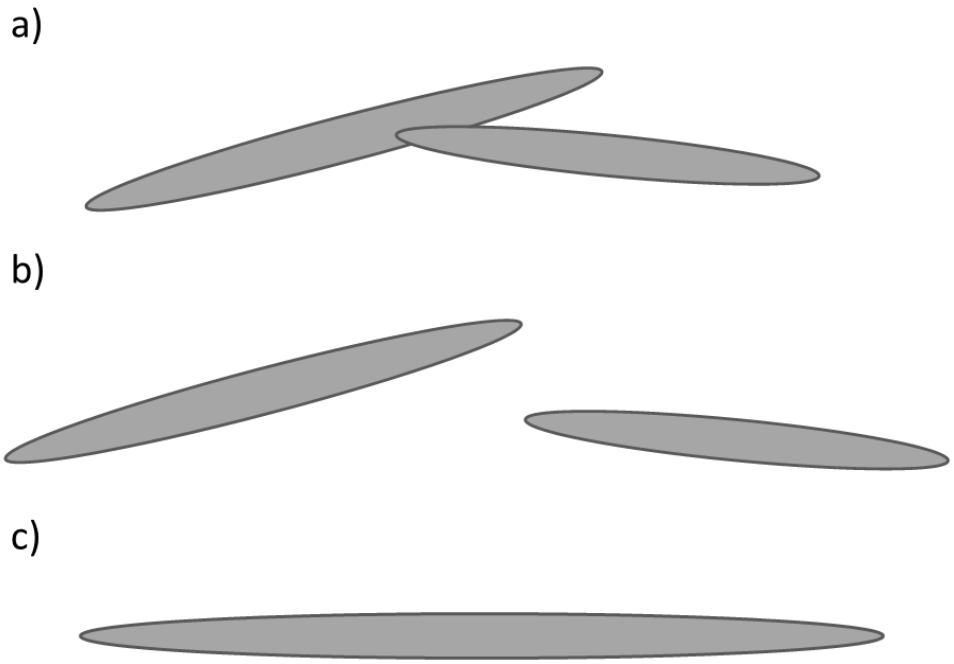

Figure 4.8: Whisker junction schematic for a) directly touching whiskers junctions, b) whisker junctions which are not directly in contact, and c) whiskers alone

4.2 SPS Parameters Effect

By comparing the four replicate sample sets for sample E (no additives) and D (containing 1% MgO and 1% Y_2O_3), the results of slightly differing processing conditions for the spark plasma sintered samples can be seen. The changes in parameters are as described previously in Chapter 2, Table 2.4. Since these samples are normalized by geometry, the additional powder used in the first set of samples which resulted in thicker samples does not have a strong influence on the pure SPS E4 sample relative to the others. However, for the SPS D4 sample with the most sintering additives, the resistivity is significantly higher. This may be the

result of a particularly insulating portion within the sample and not a direct result of the geometry alone. This data is shown in Figure 4.9a and Figure 4.9b.

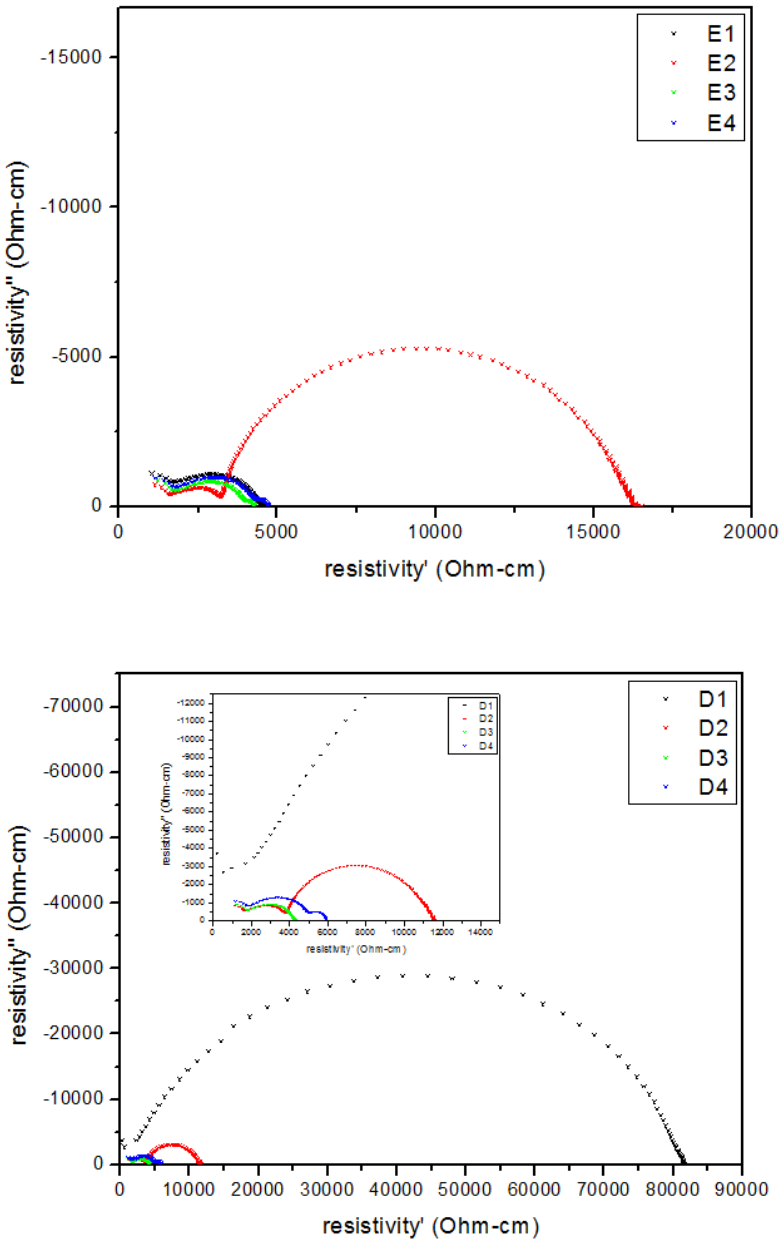

Figure 4.9: a) and b) All four sample sets for the SPS compared for the two extremes of the sintering additives E and D respectively

4.3 EDX Measurements

Energy-dispersive X-ray spectroscopy installed on the Zeiss Ultra60 FE-SEM was used to confirm the nature of the microstructure observed through both SEM and AFM. By using EDX, the chemical composition of individual sections of an SEM image can be studied. Figure 4.10 lists the base image the EDX analysis was conducted upon.

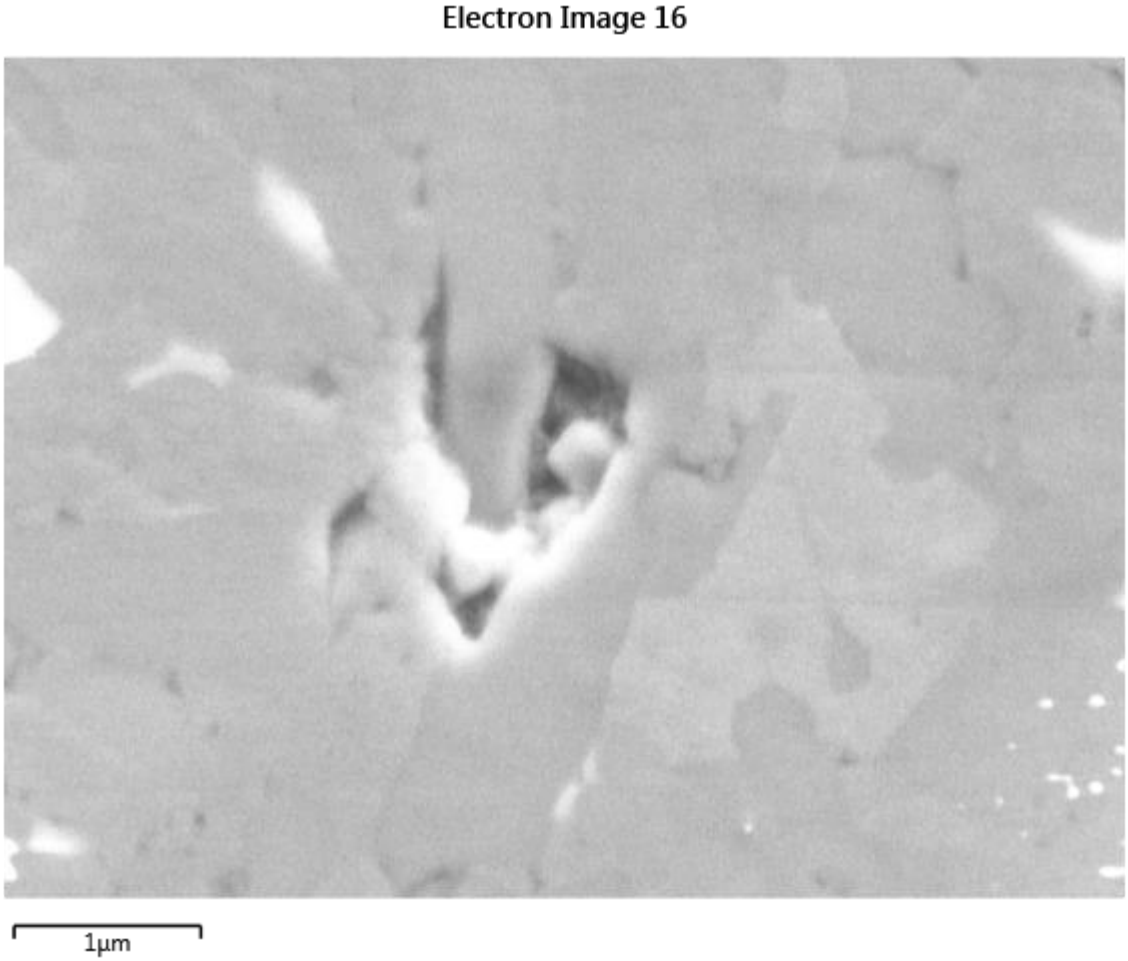

Figure 4.10: SEM base image used for EDX study

Figure 4.11 displays the individual element response for Al, O, Si, and C for the image shown in Figure 4.10. The clear segregation between the matrix elements within alumina and the filler elements within SiC are easily discernable. The whisker morphology is distinct and present

within the image as well. These EDX results show without a doubt what was assumed to be the case in all the previous microscopy data, the needle shaped whiskers embedded on the surface are comprised of SiC alone and the matrix surrounding it is the alumina.

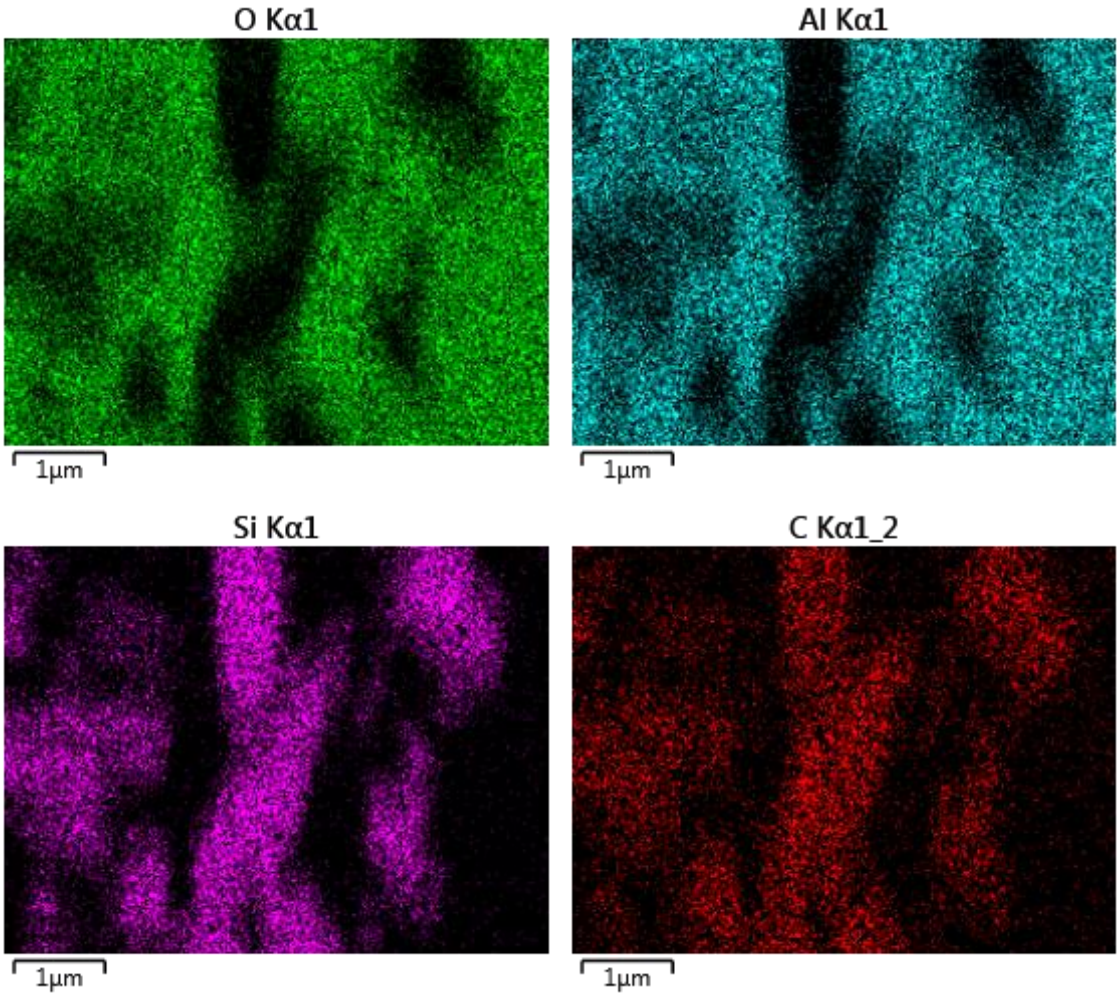

Figure 4.11: EDX highlighting individual element positions relative to SEM image from Figure 4.10

The map sum spectrum given from this one image does not match exactly the sample composition expected throughout the entire sample, but this is understandable due to the fact that the sample size of one image is nowhere near enough to accurately represent the sample as a whole. Nevertheless, this data shows the matrix elements having a dominating presence overall

within the sample and in addition to the strength of the peaks given by the number of the counts received by the detector the location of the peaks within the keV spectrum are given here as well. Oxygen by far has the strongest signal, followed by the Al signal. The filler material elements of Si and C have significantly weaker responses. The Kα for all four of these elements happens to be within the 0-2 keV range. This allows for a relatively low accelerating voltage to be used to gather data through EDX. This data can all be observed within Figure 4.12.

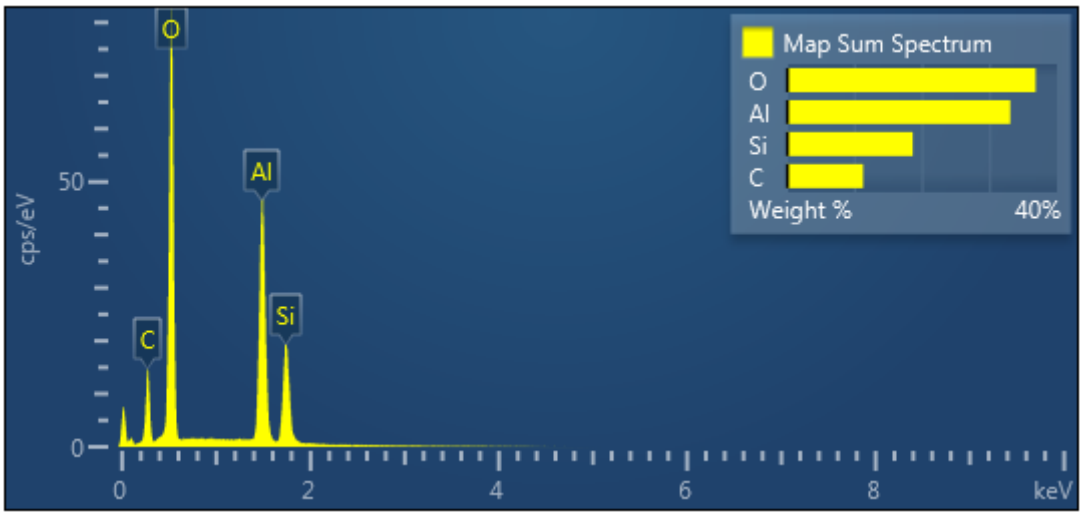

Figure 4.12: Map spectra for EDX showing both the counts relative to the electric field and the map sum spectrum of the elements

4.4 XRD Data

Figure 4.13 and Figure 4.14 are the data gathered from XRD tests on the spark plasma sintered samples. While Figure 4.13 shows all the peaks from roughly 20 degrees to 90 degrees, Figure 4.14 was added to better illustrate the effect of changing the sintering additives. The peak labeled right before the 30 degree marker is a clear indicator of a peak associated with the Y_2O_3 sintering aid. The reason this is associated with Y_2O_3 is clear if the five compositions are reexamined. Excluding the pure composition E, A through D all have 1% of Y_2O_3 incorporated into the blend. The pink data points of composition E is the only sample with no response at this

labeled peak. Next, a number of MgO associated peaks can be found in Figure 4.13 as well. The peak labeled on the figure is a prime example of this, but unlabeled peaks around 32 degrees and 37 degrees show a similar response. In these areas you can see a gradual increase in peak intensity as the sintering additive in this case MgO is increased. Peaks such as these are spread throughout the 20 to 90 degree range of these XRD scans.

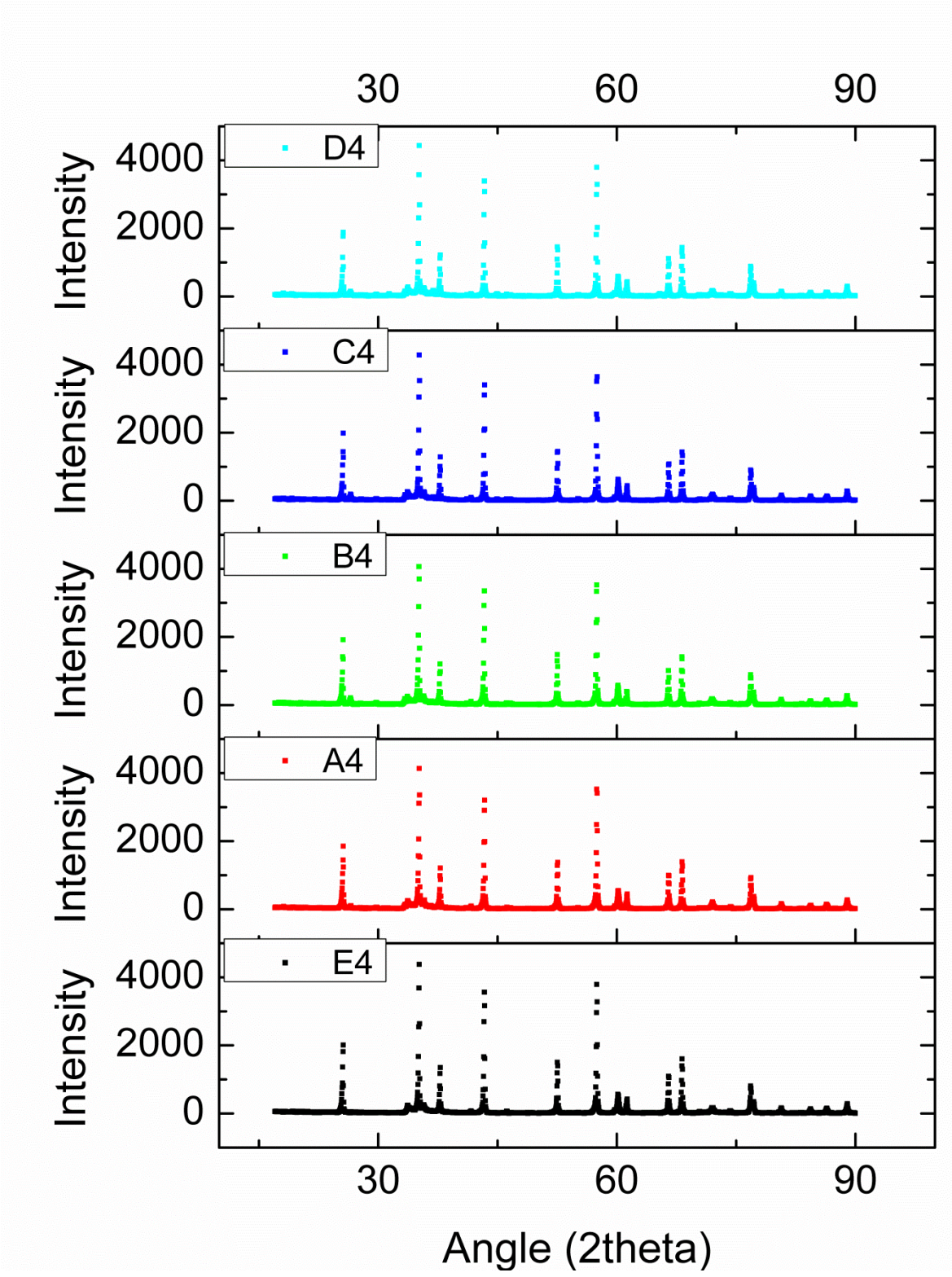

Figure 4.13: XRD data for SPS samples set 4 overlapped to outline differences in additive content

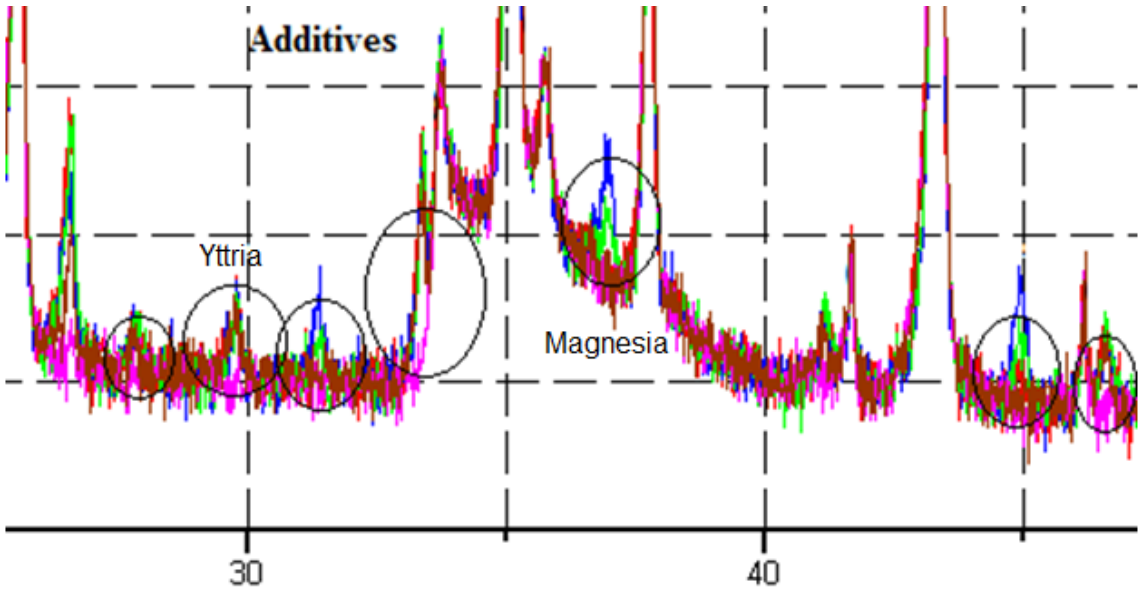

Figure 4.14: Zoomed in version of XRD data to specifically showcase some peaks attributed to Y_2O_3 and MgO

This chapter served to study specifically the differences between the hotpressed and spark plasma sintered samples containing different amounts of additives while keeping the SiC_w content fixed at 15%. In addition to the impedance responses and microstructure being compared via impedance spectroscopy and SEM imaging respectively, the samples were also compared across the five compositions made with differing amounts of sintering additives. The changes through the five compositions were best studied using EDX and XRD. Some tests conducted here served to reaffirm relatively obvious or simple observations such as the increasing level of peak responses for additives in the XRD data. While others served to discover results that may not be as intuitive such as the direct result of how sintering additives affect the impedance response. Ultimately, the resulted garnered should assist future studies which can take these results a step further.

Chapter 5

Conclusions and Future Work

5.1 Conclusions

This study accomplished the goal of bridging the gap in information between full length extruded rods and thin slices as well as looking into the effects of varying the amount of sintering additives while keeping the SiC_w filler constant. Many of the results present here were obtained using impedance spectroscopy. The reliability and consistency of these results barring any intentional changes in parameters has been proven time and time again. In both studies across different sample processing methods, the whisker concentration was kept constant because the percolation behavior has been studied extensively in previous studies [9-16].

Instead, by focusing on one composition past the percolation threshold, a systematic study on the nature of the extruded rods could be conducted which would reveal the properties of a single sample on a more micro scale. The extruded rods examined here were fabricated previously by Brian Bertram [1]. The 20% extruded rods were selected for the detailed study. The extruded rod study described in Chapter 3 includes a full length bar study across multiple 20% extruded rods, full rod sectioning studies, anisotropy studies, as well as thin slice measurements. The general observation was that there was variability present across different extruded samples despite the samples being fabricated in the same manner. This was true in both the full length rods as well as comparing different sections within the same rod in different sizes. The sizes included halves, fourths, and eighths. Due to the anisotropic nature of the samples brought about by the extrusion process, directional studies were also conducted upon the extruded rods. Results showed consistently the more conducting nature of the parallel orientation [15]. This can be attributed to the inter-whisker distances on average being much larger in the

perpendicular orientation. The importance of electrode size is then observed by conducting a DC bias measurement on both parallel and perpendicular directions.

Current AFM results showed conclusively how the current signals manifest in the shape of the whiskers. The topography image shown in conjunction with the I-AFM corroborates this. The results here are exactly as expected and despite predicting the outcome before the samples were even fabricated, it is important to show proof in a tangible manner.

Similarly to the single composition focused upon for the extruded rod samples, new samples fabricated for this study comprised a fixed amount of SiC_w only. This value was set to 15% and instead the sintering additives were adjusted. The electrode effect present when using Ag paint electrodes was quite significant, but could be removed by the use of sputtered Ag electrodes [9]. Once all samples were sputtered, the influence of the additives themselves could be compared. As the sintering additives increased, the conductivity of the samples gradually decreased. This was the case for both the hotpressed and spark plasma sintered samples. While the additives do aid during the sintering process of the sample production, allowing for lower maximum hold temperatures, once the sample is fully densified in terms of electrical conductivity their presence seems to impede the flow of current.

A direct comparison of the impedance data between hotpressed and spark plasma sintered samples was also conducted. Between all compositions, the spark plasma sintered samples were consistently more conductive compared to the hotpressed samples. The difference in conductivity ranged anywhere between 2x-10x depending on the composition. The current and voltage applied simultaneously in addition to the pressure and temperature in the case of spark plasma sintering caused inter-whisker connectivity to improve. With the addition of increasing voltage, previously undesired pathways can be unlocked so to speak. Finally, the combination of

EDX and XRD data were used to further confirm the nature of the microstructure formed. The whiskers showed strongly the elements of Si and C while the remaining matrix comprised of Al and O within the EDX data. The XRD data not only contained the Al_2O_3 and SiC peaks but showcased the presence of both sintering additives Y_2O_3 and MgO.

5.2 Future Work

Despite the progress made throughout these experiments, unexplored avenues still remain in the intellectual pursuit of these samples. The time available for the study of samples using the XRD and EDX were limited. A more detailed study looking at multiple samples especially at different compositions will be highly beneficial in being able to study how the sintering additives are mixed into the samples on a microstructural level.

Additionally, the sintering techniques especially for the spark plasma sintered samples leaves room for improvement. Even with the range of parameters varied through the four sets of spark plasma sintered samples, cracks emerged within the vast majority of these samples. In order to avoid this, further adjustments must be made. Regardless of these complications, the spark plasma sintering technology remains to be particularly promising for providing samples with improved properties.

Another direction this research can take is to conduct further impedance analysis studies incorporating DC bias. In this study, DC bias was used upon the extruded samples to the study its effects on the low frequency impedance response to eliminate the electrode effect. However, the effects of increasing DC bias on hotpressed and spark plasma sintered samples remain largely unstudied. The difference in densities and microstructure may lead to drastic effects upon these samples.

References:

[1] B. D. Bertram, “Effects of interfaces and preferred orientation on the electrical response of composites of alumina and silicon carbide whiskers,” PhD, Materials Science and Engineering, Georgia Institute of Technology, Atlanta, GA, 2011.

[2] P. F. Becher and G. C. Wei, "Toughening behavior in SiC-whisker-reinforced alumina," *Journal of the American Ceramics Society*, vol. 67 pp. 267-269, 1984.

[3] R. Gerhardt and R. Ruh, “Electrical Properties of SiC Reinforced Mullite Composites”; Paper 102-E-90 in Extended Abstracts, Electronics Division, 92nd Annual Meeting of the American Ceramic Society (Dallas, TX, April 22–26, 1990). Edited by K. M. Nair. American Ceramic Society, Westerville, OH, 1990.

[4] J. Zhang, H. Huang, L. Cao, F. Xia, and G. Li, “Semiconductive Property and Impedance Spectra of Alumina–Silicon Carbide Whisker Composite,” *J. Am. Ceram. Soc.*, vol. 75, pp. 2286–2288, 1992.

[5] R. A. Gerhardt and R. Ruh, “Volume Fraction and Whisker Orientation Dependence of the Electrical Properties of SiC-Whisker-Reinforced Mullite Composites,” *Journal of the American Ceramic Society*, vol. 84, pp. 2328–2334, 2001.

[6] J. Runyan, R. A. Gerhardt, and R. Ruh, “Electrical Properties of Boron Nitride Matrix Composites: I, Analysis of McLachlan Equation and Modeling of the Conductivity of Boron Nitride–Boron Carbide and Boron Nitride–Silicon Carbide Composites,” *Journal of the American Ceramic Society*, vol. 84, pp. 1490–1496, 2001.

[7] R. A. Gerhardt, J. Runyan, C. Sana, D. S. McLachlan, and R. Ruh, “Electrical Properties of Boron Nitride Matrix Composites: III, Observations near the Percolation Threshold in BN–B_4C Composites,” *Journal of the American Ceramic Society*, vol. 84, pp. 2335–2342, 2001.

[8] J. Runyan, R. A. Gerhardt, and R. Ruh, “Electrical Properties of Boron Nitride Matrix Composites: II, Dielectric Relaxations in Boron Nitride–Silicon Carbide Composites,” *Journal of the American Ceramic Society*, vol. 84, pp. 1497–1503, 2001.

[9] D. S. Mebane and R. A. Gerhardt, “Interpreting Impedance Response of Silicon Carbide Whisker/Alumina Composites Through Microstructural Simulation,” *Journal of the American Ceramic Society*, vol. 89, pp. 538–543, 2006.

[10] D. S. Mebane and R. A. Gerhardt, "Orientation dependence of resistivity in anisotropic ceramic composites," *Ceramic Transactions*, vol. 150, pp. 265-272, 2004.

[11] D. S. Mebane, A. M. Gokhale, and R. A. Gerhardt, “Trivariate, Stereological Length–Radius–Orientation Unfolding Derived and Applied to Alumina–Silicon Carbide Whisker Composites,” *Journal of the American Ceramic Society*, vol. 89, pp. 620–626, 2006.

[12] D. S. Mebane, S. I. Lieberman, A. M. Gokhale, R. A. Gerhardt, "Bivariate stereological unfolding procedure for randomly oriented chopped fibers or whiskers," *Acta Materialia*, vol. 53, pp. 4943-4953, 2005.

[13] B. D. Bertram and R. A. Gerhardt, "Room temperature properties of electrical contacts to alumina composites containing silicon carbide whiskers," *Journal of Applied Physics*, vol. 105, pp. 074902-074912, 2009.

[14] B. D. Bertram, R. A. Gerhardt, and J. W. Schultz, "Impedance response and modeling of composites containing aligned semiconductor whiskers: Effects of dc-bias partitioning and percolated-cluster length, topology, and filler interfaces," *Journal of Applied Physics*, vol. 111, pp. 124913-124927, 2012.

[15] B. D. Bertram and R. A. Gerhardt, "Effects of Frequency, Percolation, and Axisymmetric Microstructure on the Electrical Response of Hot-Pressed Alumina–Silicon Carbide Whisker Composites," *Journal of the American Ceramic Society*, vol. 94, pp. 1125–1132, 2011.

[16] B. D. Bertram, R. A. Gerhardt, and J. W. Schultz, "Extruded and Pressureless-Sintered Al_2O_3–SiC_w Composite Rods: Fabrication, Structure, Electrical Behavior, and Elastic Modulus." *Journal of the American Ceramic Society*, vol. 94, pp. 4391–4398, 2011.

[17] J. Runyan, R. A. Gerhardt, and R. Ruh, "Electrical properties of boron nitride matrix composites: I, analysis of McLachlan equation and modeling of the conductivity of boron nitride-boron carbide and boron nitride-silicon carbide composites," *Journal of the American Ceramics Society*, vol. 84, pp. 1490-1496, 2001.

[18] M. Taya, "Electronic Composites." Cambridge University Press: Cambridge, 2005.

[19] W. S. Johnson and M. J. Birt, "Comparison of some micromechanics models for discontinuously reinforced metal matrix composites," *Journal of Composites Technology Research*, vol. 13, pp. 161-167, 1991.

[20] P. F. Becher, C. H. Hsueh, P. Angelini, and T. N. Tiegs, "Theoretical and experimental analysis of the toughening behavior of whisker reinforcement in ceramic matrix composites," *Materials Science and Engineering A-Structural Materials Properties Microstructure and Processing*, vol. 107, pp. 257-259, 1989.

[21] R.A. Gerhardt, "Impedance Spectroscopy and Mobility Spectra," Chapter in Encyclopedia of Condensed Matter Physics, Elsevier Press, pp. 350-363, 2005

[22] W. Cao and R. Gerhardt, "Calculation of Various Relaxation Times and Conductivity for a Single Dielectric Relaxation Process," *Solid State Ionics*, vol. 42, pp. 213-221, 1990.

[23] R. Gerhardt and A.S. Nowick, "The Grain Boundary Conductivity Effect in Ceria Doped with Various Trivalent Cations. Part I: Electrical Behavior," *J. Amer. Ceram. Soc.* vol. 69, pp. 641-646, 1986.

[24] T. Pruyn, "Investigation of Percolation in Borosilicate Glass Matrix Composites Containing Conducting Segregated Networks," PhD, Materials Science and Engineering, Georgia Institute of Technology, Atlanta, GA, 2014.

[25] R. Muhlbauer, "Structure-Property-Processing Relationships in Paper and Carbon Nanotube Composite Materials," PhD, Materials Science and Engineering, Georgia Institute of Technology, Atlanta, GA, 2014.

[26] R. Gerhardt, "Impedance and Dielectric Spectroscopy Revisited: Distinguishing Localized Relaxation from Long-Range Conductivity," *J. Phys. Chem. Solids*, vol. 55, pp. 1491-1506, 1994.

[27] R. Ou, R. Samuels, and R. A. Gerhardt, "In-plane impedance spectroscopy of doped polyaniline films," *J. Plastic Film and Sheeting*, vol. 17, pp. 184-196, 2001.

[28] C. J. Capozzi, Z. Li, R. A. Gerhardt, and R. J. Samuels, "Impedance Spectroscopy And Optical Characterization Of Polymethylmethacrylate/Indium Tin Oxide Nanocomposites With Three-Dimensional Voronoi Microstructures," *J. Applied Physics*, vol. 104, pp. 114902-114912, 2008.

[29] M. P. Garrett, I. N. Ivanov, R. A. Gerhardt, A. A. Puretzky, and D. B. Geohegan, "Separation of Junction and Bundle Resistance in Single Wall Carbon Nanotube Percolation Networks by Impedance Spectroscopy," *Appl.Phys.Lett*. vol. 97, pp. 163105, 2010.

[30] Advanced Composite Materials LLC website, www.acm-usa.com.

[31] T. E. Quantrille, "Ceramic Composites for Microwave Grilling and Speed Cooking," in 42nd Annual Microwave Symposium. International Microwave Power Institute, New Orleans, LA, 2008.

[32] X. Li, "Ceramic Cutting Tools - An Introduction," *Key Engineering Materials*, vol. 96, pp. 1-18, 1994.

[33] P. Mehrotra, "Applications of ceramic cutting tools," *Key Engineering Materials*, vol. 138, pp. 1-24, 1998.

[34] C. Dogan and J. Hawk, "Influence of whisker toughening and microstructure on the wear behavior of Si_3N_4- and Al_2O_3-matrix composites reinforced with SiC," *Journal of Materials Science*, vol. 35, pp. 5793-5807, 2000.

[35] J. R. Brandt and R. A. Gerhardt "Assessment of Homogeneity of Extruded Alumina-SiC Composite Rods Used in Microwave Heating Applications by Impedance Spectroscopy," *Mater. Res. Soc. Symp. Proc.*, vol. 1538, 2013.

[36] R. Marder, C. Estournès, G. Chevallier, and R. Chaim, "Plasma in spark plasma sintering of ceramic particle compacts," *Scripta Materialia*, vol. 82, pp. 57-60, 2014.

[37] Z. H. Zhang, Z. F. Liu, J. F. Lu, X. B. Shen, F. C. Wang, Y. D. Wang, "The Sintering Mechanism In Spark Plasma Sintering – Proof Of The Occurrence Of Spark Discharge,"*Scripta Materialia,* vol. 81, pp. 56-59, 2014.

[38] C. B. Carter and M. G. Norton, "Ceramic Materials Science and Engineering." Springer: New York, 2007.

[39] R. W. Rice, "Ceramic Fabrication Technology." Marcel Dekker, Inc.: New York, 2003.

[40] http://cleanroom.ien.gatech.edu/equipment/149/zeiss-ultra60-fe-sem/ (Accessed June 27, 2014)

[41] http://research.fit.edu/nhc/documents/XE100UserManual.pdf (Accessed June 23, 2014)

[42] C. Q. Peng, Y. S. Thio, and R. A. Gerhardt, "Conductive paper fabricated by layer-by-layer assembly of polyelectrolytes and ITO nanoparticles," *Nanotechnology*, vol. 19, pp. 505603, 2008.

[43] J. Waddell, R. Ou, C. J. Capozzi, S. Gupta, C. A. Parker, R. A. Gerhardt, K. Seal, S. V. Kalinin and A. P. Baddorf. "Detection of percolating paths in polyhedral segregated network composites using electrostatic force microscopy and conductive atomic force microscopy," *Appl. Phys. Lett.* vol. 95, pp. 233122, 2009.

[44] http://www.azonano.com/equipment-details.aspx?EquipID=325 (Accessed June 27, 2014)

[45] W. Cao, R. Gerhardt, and J. Wachtman, "Preparation and sintering of colloidal silica-potassium silicate gels," *Journal Of The American Ceramic Society*, vol. 71, pp. 1108-1113, 1988.

[46] W. R. Dinkins, "Electrical Characterization of Insulating Materials Using Spectral and Spatial Measurements," MS, Materials Science and Engineering, Georgia Institute of Technology, Atlanta, GA, 1994.

[47] E. A. Holm and M. J. Cima, "Two-Dimensional Whisker Percolation in Ceramic Matrix–Ceramic Whisker Composites," *J. Am. Ceram. Soc.*, vol. 72, pp. 303–305, 1989.